

**Effect of Thermal Annealing of Atomic-Layer-Deposited
AlO_x/ Chemical Tunnel Oxide Stack Layer at the
PEDOT:PSS/n-type Si Interface to Improve its Junction
Quality**

(導電性高分子 PEDOT:PSS/n-type Si 接合特性改善のための
原子層成長 AlO_x/化学酸化層積層構造の熱処理効果に関する研究)



*A Dissertation Submitted to the Graduate School of Science and
Engineering of Saitama University in Candidacy for the Degree of Doctor
of Philosophy*

By

Md Enamul Karim

Recommended for Acceptance by the Department of Functional Material
Science

Supervisor: Hajime Shirai

Submission: September 2020

Dedicated to My Parents

Mr Shahid Ullah

&

Fatema Juhura

Abstract

High-efficiency c-Si solar cells are attracting interest in research, in which a metal oxide or organic polymer thin film having electron/hole transporting ability is bonded to crystalline Si (c-Si) as an anode and a cathode. In our previous study, a transparent and high hole-transporting conductive polymer poly(3,4-ethylenedioxy thiophene):poly(styrene sulfonate) (PEDOT:PSS) was used to plane n-type crystal Si (We have achieved an efficiency of 13.3% for pristine PEDOT:PSS device), and have achieved an efficiency of 15.5% by using an antireflection film together. Furthermore, we have prototyped 10 series modules for 2 cm² and 4-inch size elements and have demonstrated the potential as an independent power supply for surveillance cameras. However, in order to further improve the device performance, it is necessary to promote the passivation of the c-Si/PEDOT:PSS anode-cathode interface and further enhance the internal electric field at the anode-cathode interface. In this doctoral dissertation, aluminum oxide (AlO_x), which is expected to have high Si passivation ability and high fixed charge density, among high-k materials with high dielectric constant, and PEDOT:PSS/n-Si interface were selected. The effect of increasing the electric field strength at the interface was investigated by inserting the film into the PEDOT:PSS/n-Si interface. Firstly, by arranging the amorphous (a-) AlO_x films prepared by atomic layer deposition (ALD) in islands, the efficiency of hole collection at the anode, and the improvement of AlO_x to increase the electric field strength at the anode interface. Secondly, Si passivation by short-time heat treatment (RTA) at 425°C in a reduced pressure environment and an atmospheric pressure heat treatment (FGA) in an N₂/H₂ environment of a coated structure of a 1-2 nm thick AlO_x layer and a chemically oxidized SiO_x layer. And the effects on

PEDOT:PSS/n-Si interface local chemical bond state, electronic structure, and device performance were investigated. This doctoral dissertation consists of 6 chapters. The outline of each chapter is described below:

Chapter 1, "Introduction", describes the background of research and development of crystalline Si solar cells and the purpose of this paper.

In Chapter 2, the effect of a TiO_x layer as a hole blocking layer at the Si/Al interface on the back cathode of a c-Si solar cell is discussed from steady-state photocurrent and current transient response characteristics. Specifically, focusing on TiO_2 , which has a small work function, a titanium oxide (TiO_2) synthesized by hydrolysis of TiCl_4 was used to insert a TiO_x layer with a thickness of 1-2 nm at the n-Si/Al interface by spin coating. It has been demonstrated that the device structure is effective in improving the conversion efficiency and the efficiency of collecting photo-generated carriers in the 600-1200 nm region as compared with the device performance without insertion. Furthermore, in order to quantitatively evaluate the hole blocking ability, the hole current pushed back into the c-Si by the hole blocking layer by instantaneously applying the reverse bias from the steady current when the forward bias was applied in the dark. We established a Transient Reverse Recovery measurement to determine the recombination velocity S from the waveform. As a result of a comparative study of this technique with existing techniques for evaluating the recombination rate, such as the QSSPC and μ -PCD methods, it has been clarified that it can be sufficiently used as a technique for evaluating the performance of the hole blocking layer.

Chapter 3, "Experimental procedure", describes the fabrication method and the evaluation method of the ultra-thin aluminum oxide (AlO_x) film, which is expected as a high dielectric constant material (high-k), by the ALD method for the purpose of

enhancing the electric field strength at the PEDOT:PSS/n-Si anode interface. It also describes the photolithography process for forming a $15 \times 15 \mu\text{m}^2$ island array, chemical oxide layer formation, RTA, and FGA heat-treatment process. About the in-plane distribution of minority carrier lifetime (τ_{eff}) by μ -photoconductive decay method (μ -PCD method), X-ray photoelectron spectroscopy (XPS) method, and infrared absorption spectroscopy (FTIR) evaluation method for the above ultrathin films.

In Chapter 4, 4.1 describes the fundamental physical properties of amorphous (a-)AlO_x insulator thin films produced by an alternate supply of TMA[Al(CH₃)₃] and water by the ALD method. Film formation was performed by using TMA, water supply time, time sequence, substrate temperature as variables, the film thickness, surface morphology, and local chemical bonding state were evaluated. In addition, the physical properties of n-Si interface bonding were evaluated by short-time heat treatment (RTA) at 425°C for 15 minutes in a reduced pressure environment after film formation. As a result, it was clarified that the surface roughness and the Al(OH) bond remaining in the film were reduced most at the substrate temperature of 200°C, and a dense amorphous structure was formed.

In 4.2, in order to achieve both passivation of the c-Si surface and hole trapping ability, a $15 \times 15 \mu\text{m}^2$ size of 20 nm thick ALD a-AlO_x with different lattice spacing was formed on the c-Si surface by photolithography. We investigated the PEDOT:PSS/a-AlO_x/n-Si junction characteristics and device performance of spin-coated 80 nm thick PEDOT:PSS layer on the island array. The Si passivation ability was improved, and the diffusion potential was increased to 1.4V with the increase of the a-AlO_x/PEDOT:PSS area ratio, but the fill factor in the solar cell element was significantly decreased by the increase of the parallel resistance, which deteriorated the conversion efficiency.

Therefore, in Section 4.3, we investigated the effect of inserting a 2-3 nm thick AlO_x ultrathin layer formed by the ALD method as a tunnel layer and Si passivation. In the RTA of 20-nm-thick a- AlO_x , τ_{eff} was reduced from 150 μs to 15-30 μs . On the other hand, τ_{eff} can be improved to 600-700 μs by FGA treatment of a- $\text{AlO}_x/\text{ch-SiO}_x/\text{n-Si}$ coated structure with ch-SiO_x of 1-2 nm thickness inserted at the a- $\text{AlO}_x/\text{n-Si}$ interface. It is revealed that, from the evaluation of the sheet resistance, as a result of FGA processing of the coated structure, it decreases from PEDOT:PSS/c-Si junction $162\Omega/\square$ to PEDOT:PSS/a- $\text{AlO}_x/\text{ch-SiO}_x/\text{n-Si}$ coated structure $105\Omega/\square$. In addition that, from the evaluation of the capacitance-voltage (C-V) characteristics, the fixed charge density was changed from $3.2 \times 10^{12} \text{ cm}^{-2}$ to $5.7 \times 10^{12} \text{ cm}^{-2}$ by applying FGA processing from a- $\text{AlO}_x/\text{n-Si}$ to a- $\text{AlO}_x/\text{ch-SiO}_x/\text{n-Si}$ coated structure, and the interface state density decreased from $4.5 \times 10^{11} \text{ cm}^{-2}\text{eV}^{-1}$ to $2 \times 10^{11} \text{ cm}^{-2}\text{eV}^{-1}$. Moreover, the conversion efficiency of the device on the planarized n-Si with PEDOT:PSS/a- $\text{AlO}_x/\text{ch-SiO}_x/\text{n-Si}$ coated structure as anode is 13.08% without insertion and 14.91% (open voltage: 0.645V, Fill factor: 0.77, short-circuit current density increased to 30 mA/cm^2).

In Chapter 5, the electronic structure of the interface in the a- $\text{AlO}_x/\text{ch-SiO}_x/\text{n-Si}$ layered structure by ch-SiO_x insertion and RTA and FGA treatment was evaluated by XPS, UV spectroscopy, and Kelvin probe method. FGA treatment revealed that ch-SiO_x contained a large proportion of Si^* complexes near 103 eV, which did not belong to Si^+ , Si^{2+} , Si^{3+} , and Si^{4+} , compared to RTA. In RTA, the oxidation of the a- AlO_x layer on the surface became dominant, whereas in FGA, the oxidation of the ch-SiO_x layer was promoted as the reduction of the AlO_x layer progresses, and as a result, the passivation ability of the c-Si surface was improved. Besides, the band level diagram of the PEDOT:PSS/a- $\text{AlO}_x/\text{ch-SiO}_x/\text{n-Si}$ interface was determined, and the a- $\text{AlO}_x/\text{ch-SiO}_x/\text{n-Si}$

coated structure was inserted, and the subsequent FGA treatment was performed to form the anode interface. It was clarified for the first time that the electric field strength was enhanced.

In Chapter 6, we summarized the doctoral dissertation, gave conclusions, and mentioned future prospects.

Acknowledgments

First of all, I would like to thank my supervisor, Professor Hajime Shirai, for his scholastic guidance advice and countless support. I am especially thankful for his encouraging words and patience. Without his support, I could not have overcome the numerous paper revision, months of fruitless results, and moments of confusion. I also acknowledge his help to sort out my problems in personal matters. Besides of my supervisor, I am very much thankful to Professor Masamichi Sakai, Professor Kenji Kamishima, and Professor Keiji Ueno for their valuable comments and guidance in this journey.

Special thanks to all former and present members of Shirai group. First, I must thank senior members, Dr. Jaker Hossain, Dr. A.T.M. Saiful Islam, Daisuke Harada, Koji Kasahara, and Takanori Kuroki for their fruitful suggestions and support in my beginning days in Japan. I also very much thankful to Arifuzzaman Rajib, Abdul Kuddus, Yuki Nasuno, Moriya Yuma, Kawamura Koki, Imai Koki, Miyamoto Ryuta, Matsuzaki Ryuji, Funajima Yusuke, Takahashi Rayato for their support and excellent research environment.

I must acknowledge the generosity of all funding agencies. This work was partially supported by a Japan Science and Technology Agency (JST) grant, a Grant-in-Aid for Scientific Research from the Ministry of Education, Culture, Sports, Science, and Technology (MEXT) of Japan. And, my great thanks to MEXT for the scholarship support for my Ph.D. program at Saitama University.

My gratitude also goes to Assistant Professor, Dr. Ryo Ishikawa, for his fruitful comments and excellent advice during my research work. I am also thankful to all the staff of the Department of Functional Materials Science, Saitama University. Especially, to Mr. Yoshiaki Saito and Nobuhiko Gokan for their technical and maintenance support.

Also, I would like to thanks Professor Tatsuro Hanajiri, Associate Professor Tomofumi Ukai, Associate Professor Shunji Kurosu, Technical manager Masahide Tokuda, and Yasuhiko Fujii, Toyo University, Kawagoe campus, for their kind helping and fruitful discussion in UV photolithography facility, SEM and EDS characterization, and analysis. I also highly appreciate Mr. Yoshiharu Iwai of Riken Keiki Co. Ltd, Japan, for Kelvin Probe measurement.

In the end, I would like to acknowledge my family members from the bottom of my heart. First, to my parents, they had always been beside me by their kind support and excellent care, they had never shied away from sacrificing their happiness even for fulfilling my small wishes and for my tiny achievements. After that, I would like to thank my beloved wife for her endless support at every moment of my life.

Finally, I would like to thank all my teachers, friends, well-wisher for their endless support during my journey.

List of Publications and Presentations

Journal Papers

1. **M. E. Karim**, Y. Nasuno, A. Kuddus, T. Ukai, S. Kurosu, M. Tokuda, Y. Fujii, Y. Nakajima, T. Hanajiri, R. Ishikawa, K. Ueno, H. Shirai, “Effect of thermal annealing of ALD-AlO_x/chemical tunnel oxide stack layer on the junction properties at the organic/n-type silicon interface”, J. Appl. Phys. **128**, 045305 (2020).
2. **M. E. Karim**, A.T.M. S. Islam, Y. Nasuno, A. Kuddus, R. Ishikawa, H. Shirai , “Solution-Processed TiO₂ as a hole blocking layer in PEDOT:PSS./n-Si Heterojunction Solar Cells”, EPJ-Photovoltaics, **11**, 7 (2020).
3. A. Rajib, **M. E. Karim**, T. Ukai, S. Kurosu, M. Tokuda, Y. Fujii, Y. Nakajima, T. Hanajiri, R. Ishikawa, K. Ueno, and H. Shirai, “Synthesis of AlO_x thin films by atmospheric-pressure mist chemical vapor deposition for effects on junction properties at the AlO_x/Si interface” J. Vac. Sci. Technol. A **38**, 033413 (2020).
4. A.T.M. S. Islam, **M. E. Karim**, A. Rajib, Y. Nasuno, T. Ukai, S. Kurosu, M. Tokuda, Y. Fujii, Y. Nakajima, T. Hanajiri, H. Shirai, “Chemical mist deposition of organic for efficient front- and back- PEDOT:PSS/crystalline Si heterojunction solar cells”, Appl. Phys. Lett. **114**, 193901 (2019).

Conference Presentations

1. **M. E. Karim**, Arifuzzaman Rajib, Yuki Nasuno, Tomofumi Ukai, Shunji Kurosu, Masahide Tokuda, Yasuhiko Fujii, Tatsuro Hanajiri, R. Ishikawa, Keiji Ueno, H. Shirai, “Effect of the tunnel oxide/ AlO_x stacked hole-selective contacts on the junction properties at PEDOT:PSS/n-type Si interface”, The 67th JSAP Spring Meeting, 2020, Tokyo, Japan.
2. **M. E. Karim**, Tomofumi Ukai, A.T.M. S. Islam, Shunji Kurosu, Yasuhiko Fujii, Masahide Tokuda,, Tatsuro Hanajiri, R. Ishikawa, Keiji Ueno, H. Shirai, “PEDOT:PSS/n-Si heterojunction solar cells with ALD- Al_2O_3 /n-Si field effect inversion layer”, The 80th JSAP Autumn Meeting, 2019, Hokkaido, Japan.
3. **M. E. Karim**, Tomofumi Ukai, Daisuke Harada, A.T.M. S. Islam, Shunji Kurosu, Yoshikata Nakajima Yasuhiko Fujii, Masahide Tokuda, Tatsuro Hanajiri, R. Ishikawa, Keiji Ueno, H. Shirai, “PEDOT:PSS/n-Si heterojunction solar cells with ALD- Al_2O_3 /n-Si field effect inversion layer”, The 66th JSAP Spring Meeting, 2019, Tokyo, Japan.
4. **M. E. Karim**, Tomofumi Ukai, Daisuke Harada, A.T.M. S. Islam, Shunji Kurosu, Yoshikata Nakajima Yasuhiko Fujii, Masahide Tokuda, Tatsuro Hanajiri, R. Ishikawa, Keiji Ueno, H. Shirai, “PEDOT:PSS/n-Si heterojunction solar cells with ALD- Al_2O_3 /n-Si field effect inversion layer” 6th Korea-Japan Joint Symposium on Advanced Solar Cells, 2019, Nikko, Japan
5. **M. E. Karim**, S. Kurosu, Y. Nakajima, Y. Fujii, M. Tokuda, T. Hanajiri, R. Ishikawa, Keiji Ueno, H. Shirai “Passivation of nanopillar Si surface by ALD- AlO_x and its effect on PV performance of PEDOT:PSS/n-Si solar cells” The 79th JSAP Autumn Meeting, 2018, Nagoya, Japan.

List of Tables

- 2.1** Summary of PV performance for the PEDOT:PSS/n-Si solar cells with various thicknesses of TiO₂ HBL.
- 3.1** Area ratio of AlO_x island with a PEDOT:PSS overlayer
- 4.1** Local vibration modes of AlO_x related FTIR peaks
- 4.2** Photovoltaic parameters of the pristine PEDOT:PSS/n-Si device with a different area ratio of AlO_x island & PEDOT:PSS
- 4.3** Chemical shifts of SiO_x suboxide components, Si²⁺, Si³⁺, Si^{*}, and Si⁴⁺, from the Si(2p_{3/2}) core energy level used as a reference value for ALD-AlO_x (six cycles) with and without tunnel oxide *ch*-SiO_x (1-3) layers before and after FGA and RTA.
- 4.4** Solar cell parameters for the pristine PEDOT:PSS/n-Si device and the devices with solely ALD-AlO_x and the AlO_x/*ch*-SiO_x (1~3nm) stack ultrathin layers.
- 5.1** Determination of valance band offset for ALD-AlO_x/n-Si interface with and without tunnel oxide *ch*-SiO_x layers.
- 5.2** Sheet resistance for PEDOT:PSS/n-Si devices with and w/o AlO_x and AlO_x/*ch*-SiO_x(1~3nm) interlayers

List of Figures

- 1.1** Solar cell efficiency charts produced by NREL
- 1.2** Molecular structure of PEDOT and PSS
- 1.3** Efficiency progress of PEDOT:PSS/n-Si solar cells with time
- 1.4** Property of several high-k materials with their band offset. [G.D. Wilk et al., J. Appl. Phys.10, 15 (2001)]
- 1.5** (a) Schematic band diagram of AlO_x /n-Si interface and (b) proposed device diagram of PEDOT:PSS/ AlO_x island/ n-Si HT solar cells
- 1.6** Proposed device diagram and its corresponding band diagram of PEDOT:PSS/n-Si junction with and without stack layer of ALD- AlO_x /*ch*- SiO_x
- 2.1** (a) PEDOT:PSS chemical structure, (b) Schematic structure of the PEDOT:PSS/n-Si/ TiO_2 double heterojunction solar cells with single- and double- TiO_2 layers as a HBL
- 2.2** XPS profile of the Ti(2p) core levels of, (a) TiO_2 /n-Si, and (b) Al/ TiO_2 /n-Si, samples.
- 2.3** 2D mapping of minority career lifetime for the TiO_2 coated n-Si substrate
- 2.4** Schematics of (a) the circuit diagram and (b) T_{rr} current for the devices with and without HBLs
- 2.5** (a) J-V curve of PEDOT:PSS/n-Si solar cells with different layer thicknesses of TiO_2 as HBL. (b) the EQE for the devices with and without a 2-nm-thick TiO_2 HBLs. The inset shows the $\text{EQE}_{\text{TiO}_2}/\text{EQE}_{\text{pristine}}$ ratio. (c) The 2D map of the EQE

- at 1050 nm for pristine device with and without a 2-nm-thick TiO_2 HBL
- 2.6** (a) Normalized EQE, $\text{EQE}_{\text{TiO}_2}/\text{EQE}_{\text{pristine}}$ and (b) I_{rr} current profiles of the PEDOT:PSS/n-Si heterojunction solar cells with single- and double-layer of 2-nm-thick TiO_2 as HBL including the recovery time for each devices
- 3.1** Fabrication process of PEDOT:PSS/n-Si heterojunction solar cell
- 3.2** Basic principle of Al_2O_3 deposition by Atomic Layer Deposition (ALD)
- 3.3** Schematic diagram of the ALD system
- 3.4** Gas supply of ALD system
- 3.5** Pattern mask for 15 μm squatted AlO_x islands with a different interval from 15-150 μm distance
- 3.6** Fabrication process of AlO_x island on c-Si substrate using UV photolithography process
- 3.7** (a) Microscopic image of AlO_x island on n-Si substrate and (b) thickness profile of AlO_x island
- 3.8** a) Device fabrication of PEDOT:PSS/n-Si solar cell with AlO_x island, (b) Cross-sectional image of AlO_x island/PEDOT:PSS on n-Si substrate
- 3.9** Figure-3.9: Fabrication process of ch-SiO_x at the $\text{AlO}_x/\text{n-Si}$ interface
- 3.10** Schematic device diagram of PEDOT:PSS/n-Si heterojunction with ultrathin $\text{AlO}_x/\text{ch-SiO}_x$ stack layer
- 3.11** Principle of micro-photoconductive decay ($\mu\text{-PCD}$) method
- 3.12** Schematic diagram of Forming gas annealing (FGA) and Rapid thermal annealing (RTA)
- 3.13** Schematic diagram of an AFM system
- 3.14** (a) Schematic diagram of an FTIR set up, (b) Simple interferometer with a beam-

- splitter and compensator plate
- 3.15** FTIR spectroscopy (Shimadzu, ITTracer-100 system)
 - 3.16** (a) Schematic of an MIS structure used in C-V measurement, (b) Modelled ideal C-V curve (no interface state, $V_{fb}=0V$) of a silicon MIS capacitor at low and high frequencies. The voltage ranges corresponding to accumulation, depletion, weak inversion, and strong inversion are indicated
 - 3.17** (a) principle of XPS with scan spectra for the ultrathin thick SiO_2 on Si substrate, (b) deconvolution of Si 2P core level for $\sim 5\text{\AA}$ thick SiO_2 on Si substrate and the possible Si suboxide peaks
 - 3.18** Schematic diagram of a PYSA system configuration with PC screen of a measurement sample of AC-2 by PYSA system
 - 3.19** Energy band diagram for metals, semiconductors or organic materials measured by PYSA system configuration
 - 3.20** (a) Schematic diagram of PEDOT:PSS/ AlO_x /ch- SiO_x /n-Si device measuring sheet resistance by a four-probe circuit, and (b) its equivalent circuit diagram.
 - 4.1** AlO_x thickness plotted as a function of ALD number of cycles
 - 4.2** The growth rate of AlO_x film vs. substrate temperature
 - 4.3** AFM images of ALD- AlO_x films at a different substrate temperature
 - 4.4** FTIR spectra of ALD- AlO_x films at a different substrate temperature
 - 4.5** Effective minority carrier lifetime of ALD- AlO_x on the n-Si substrate at different values of layer thickness
 - 4.6** $1/C^2$ vs. voltage (b) summarized built-in field of PEDOT:PSS/n-Si solar cell with AlO_x island at different area ration of AlO_x island & PEDOT:PSS
 - 4.7** Photocurrent-Voltage (J-V) curve for the PEDOT:PSS/n-Si solar cell with AlO_x

- island under (a) dark condition, (b) illumination at different area ration of AlO_x island & PEDOT:PSS
- 4.8** (a) External quantum efficiency (EQE) (b) Reflectance of PEDOT:PSS/n-Si solar cell with AlO_x island at different area ration of AlO_x island & PEDOT:PSS
- 4.9** Photocurrent-Voltage (J-V) curve for the PEDOT:PSS/n-Si solar cell with AlO_x island under (a) dark condition, (b) illumination (c) EQE at different donor density substrate
- 4.10** (a) Current density and open-circuit voltage curve, (b) fill-factor and power conversion efficiency for different donor density substrate compared with pristine PEDOT:PSS device
- 4.11** Carrier concentration and built-in potential as a function of different donor density substrate
- 4.12** (a) Correlation between τ_{eff} and ALD number of cycles for ALD- AlO_x on n-Si before and after RTA for 5-15 cycles. (b) τ_{eff} of ALD- AlO_x (six cycles) and ALD $\text{AlO}_x/\text{ch-SiO}_x$ stack layers on n-Si ($1\sim5\ \Omega\cdot\text{cm}$) substrate before and after FGA at $560\ ^\circ\text{C}$ for 30 min.
- 4.13** A typical C-V curve for the MIS device
- 4.14** (a) negative fixed charge density (Q_f) as a function with $\text{AlO}_x/\text{n-Si}$ with and without ch-SiO_x ($1\sim3\text{nm}$) for as-deposited, FGA and RTA condition, (b) Q_f and D_{it} as a function with different annealing condition
- 4.15** XPS Si(2p) core energy region spectra of ALD- AlO_x (six cycles) with and without tunnel oxide ch-SiO_x ($1\sim3\text{nm}$) layers (a) as-deposited, (b) after FGA at $560\ ^\circ\text{C}$ for 30 min, and (c) RTA at $425\ ^\circ\text{C}$ for 15 min. The subfigures on the left show the spectra between $100\sim105\ \text{eV}$. The subfigures on the right show the enlarged view

- of the same energy region
- 4.16** Aluminum octahedra (Al-O₆) and aluminum tetrahedra (Al-O₄) complex
 - 4.17** FTIR spectra for the AlO_x/ch-SiO_x for as-deposited, FGA and RTA from (a) 500-400 and (b) 500-1200 cm⁻¹ wavenumber
 - 4.18** (a) Dark and (b) photocurrent density-voltage curves of pristine PEDOT:PSS/n-Si heterojunction solar cell and PEDOT:PSS/n-Si devices together with six cycles ALD-AlO_x solely and ALD-AlO_x/ch-SiO_x (1~3nm) stack interlayers. (c) V_{oc} and V_{bi} for the corresponding PEDOT:PSS/n-Si devices
 - 4.19** (a) EQE, (b) EQE_{AlO_x(AlO_x/ch-SiO_x)/EQE_{pristine}, and (c) 2D mapping of EQE at 400- and 1000-nm wavelengths for pristine PEDOT:PSS/n-Si heterojunction solar cells together with six-cycles ALD-AlO_x solely and ALD-AlO_x/ch-SiO_x (1~3nm) stack interlayers}
 - 5.1** Schematic band diagram of an MS junction
 - 5.2** XPS spectra of Al(2p) and Si(2p) core energy level regions of (a) ALD-AlO_x/n-Si, (b) AlO_x/ch-SiO_x (~1.5nm)/n-Si, and (c) AlO_x/ch-SiO_x (~3nm)/n-Si samples, respectively. The inset shows the compositional ratio for corresponding samples
 - 5.3** Derived band alignment and band offset of the ALD-AlO_x/n-Si interface with and without tunnel oxide ch-SiO_x (1~3nm) layers
 - 5.4** Figure-5.4: (top) Schematic energy band diagram of PEDOT:PSS/n-Si junction, including definitions of the energy differences. (bottom) Derived energy band diagrams of (a) PEDOT:PSS/n-Si, (b) PEDOT:PSS/AlO_x/n-Si, and (c) PEDOT:PSS/AlO_x/ch-SiO_x (1~3nm)/n-Si

List of Abbreviations

Al ₂ O ₃	Aluminum oxide
ALD	Atomic Layer Deposition
AR	Antireflection layer
a-Si	Amorphous-Si
c-Si	Crystalline Silicon
C-V	Capacitance-Voltage
CZ	Czochralski
DI	Deionized
E _g	Energy Gap
EQE	External Quantum Efficiency
FF	Fill Factor
HBL	Hole Blocking Layer
J _{sc}	Short-Circuit Current Density
J-V	Current Density-Voltage
n-Si	n-type Silicon
PCE	Power Conversion Efficiency
PEDOT	Poly (3,4-Ethylenedioxy-Thiophene)
PSS	Poly (Styrenesulfonate)
PV	Photovoltaic
S	Surface Recombination Velocity
SE	Spectroscopic Ellipsometry

SiO_x	Silicon Sub-Oxide
TiO_2	Titanium Dioxide
T_{rr}	Transient Reverse Recovery
V	Voltage
V_{bi}	Built-In Potential
V_{oc}	Open-Circuit Voltage
J_0	Dark Saturation Current Density
τ_{eff}	Effective Minority Carrier Lifetime
$\mu\text{-PCD}$	Microwave Photoconductance Decay

Table of Contents

Abstract.....	III
Acknowledgments	VIII
List of Publications and Presentations.....	X
List of Tables	XII
List of Figures.....	XIII
List of Abbreviations	XVIII
Table of Contents.....	XX
Chapter 1	1
Introduction	1
1.1 Research background	1
1.2 Crystalline-Si/Organic Heterojunction Solar Cells	3
1.3 Background of the Solution-Processed Hybrid PVs	3
1.4 Motivation of this study.....	5
1.5 Outline of This Dissertation.....	10
Bibliography	13
Chapter 2	23
Effect of TiO ₂ as a Hole Blocking Layer in the PEDOT:PSS/n-Si Heterojunction Solar Cells.....	23
2.1. Introduction	23

2.2	Experimental Details	24
2.2.1	Solution-processed TiO ₂ and the device fabrication.....	24
2.3	Characterizations.....	26
2.3.1	XPS study	27
2.3.2	Minority Carrier Lifetime	28
2.3.3	Transient reverse recovery (T _{rr}) measurement.....	28
2.4	Results and discussion	30
2.4.1	Photovoltaic performance of solar cells	30
2.4.2	Junction property at the Si/TiO ₂ cathode interface monitored by the T _{rr} characterization.....	33
2.5	Summary and conclusions.....	34
	Bibliography	35
	Chapter 3	39
	Experimental Procedure and Characterization Method.....	39
3.1	Experimental Procedure.....	39
3.1.1	Fabrication process of PEDOT:PSS/n-Si heterojunction solar cell.....	39
3.1.2	Deposition of AlO _x on c-Si by Atomic Layer Deposition (ALD)	40
3.1.2.1	Principle of AlO _x deposition by ALD	40
3.1.2.2	Sample preparation.....	41
3.1.2.3	AlO _x film deposition by ALD	42
3.1.3	Preparation of AlO _x island by UV photolithography process.....	43

3.1.3.1	Sample preparation.....	43
3.1.3.2	Preparation of AlO _x island by UV photolithography process..	44
3.1.3.3	Device fabrication PEDOT:PSS/n-Si heterojunction solar cells with AlO _x island	47
3.1.4	Fabrication process PEDOT:PSS/n-Si heterojunction solar cell with ultrathin AlO _x / <i>ch</i> -SiO _x (1~3 nm)	48
3.1.4.1	Fabrication process of <i>ch</i> -SiO _x at the AlO _x /n-Si interface	48
3.1.4.2	Fabrication process PEDOT:PSS/n-Si heterojunction solar cells with AlO _x / <i>ch</i> -SiO _x stack layer.....	48
3.2	Characterization method	50
3.2.1	Micro-photoconductive decay (μ-PCD)	50
3.2.2	Forming gas annealing (FGA) and Rapid thermal annealing (RTA) method	51
3.2.3	Atomic Force Microscopy (AFM).....	51
3.2.4	Fourier-transform infrared spectroscopy (FTIR).....	52
3.2.5	Capacitance-Voltage (C-V) Profiling	54
3.2.6	X-ray electron spectroscopy (XPS) method	55
3.2.7	Photoemission Yield Spectroscopy in Air (PYSA)	56
3.2.8	Four-probe method for sheet resistance measurement	58
	Bibliography	60
	Chapter 4	62

ALD- AlO_x related result and discussion	62
4.1 Fundamental properties of AlO_x film deposited by ALD.....	62
4.1.1 ALD- AlO_x film characterization.....	62
4.1.1.1 ALD- AlO_x film thickness	62
4.1.1.2 AFM study.....	65
4.2 Effect of ALD- AlO_x island at the PEDOT:PSS/n-Si interface property by the UV photolithography process	69
4.2.1 Effect of AlO_x island at the PEDOT:PSS/n-Si interface for different area ratio of AlO_x and PEDOT:PSS	69
4.2.2 Effect of AlO_x island at the PEDOT:PSS/n-Si interface for different donor density substrate	73
4.3 Effect of thermally annealed atomic-layer-deposited AlO_x /chemical tunnel oxide stack layer at the PEDOT:PSS/n-type Si interface to improve its junction quality	77
4.3.1 Effect of FGA and RTA at the stack layer of ALD- AlO_x / <i>ch</i> - SiO_x /c-Si	77
4.3.1.1 Effective lifetime of ALD- AlO_x / <i>ch</i> - SiO_x stack layer on c-Si....	77
4.3.1.3 Study of XPS for the ALD- AlO_x / SiO_x stack layer on c-Si with and without FGA.	81
4.3.1.3 Effect of RTA and FGA on the ALD- AlO_x with and without <i>ch</i> - SiO_x (1~3nm) by FTIR spectra	85
4.3.1 PV performance of FGA treated ALD- AlO_x / <i>ch</i> - SiO_x stack layer with the PEDOT:PSS/n-Si heterojunction solar cell	86

Bibliography	91
Chapter 5	93
Band alignment at the PEDOT:PSS/a-AlO _x / <i>ch</i> -SiO _x /c-Si interface	93
5.1 Determination of band offset and band alignment of ALD- AlO _x /SiO _x stack layer on n-Si substrate	93
5.3.4 Effect of FGA treated ALD-AlO _x / <i>ch</i> -SiO _x stack layer at the PEDOT:PSS/n-Si interface	98
Bibliography	102
Chapter 6	104
Summary and future work	104
5.1 Summary and conclusion	104
5.2 Future Work	106

Chapter 1

Introduction

1.1 Research background

There are several types of renewable energy sources that have already been established from the last decades, including wind energy, hydropower, solar energy, geothermal energy, bioenergy. Among them, solar photovoltaic (PV) devices become a very prominent way to directly convert solar energy into electricity, most commonly known as a solar cell. Early silicon solar photovoltaic cells did not have good efficiency. However, the efficiency increased day by day, while, the cost decreased. The first Si p-n junction solar cell was developed by Daryl Chapin et al. in 1954 [1], having power conversion efficiency (PCE) of 6%. In 1955, Hoffman Electronics-Semiconductor Division introduced a new photovoltaic product having only a 2% efficiency, which energy cost was \$1,785/Watt (USD). Within a few years, Hoffman Electronics was able to increase cell efficiency by up to 10%. The efficiency increased rapidly to 14% in 1960. In 1985, researchers at the University of New South Wales, Australia, were able to construct a solar cell that has over 20% efficiency. A 20% efficiency solar cell was patented in 1992. In the 21st century, efficiency continues to rise, and the future forecast shows that efficiency would be increasing more. Figure-1.1 shows the different types of solar cell efficiency charts produced by National Renewable Energy Laboratory (NREL) [2].

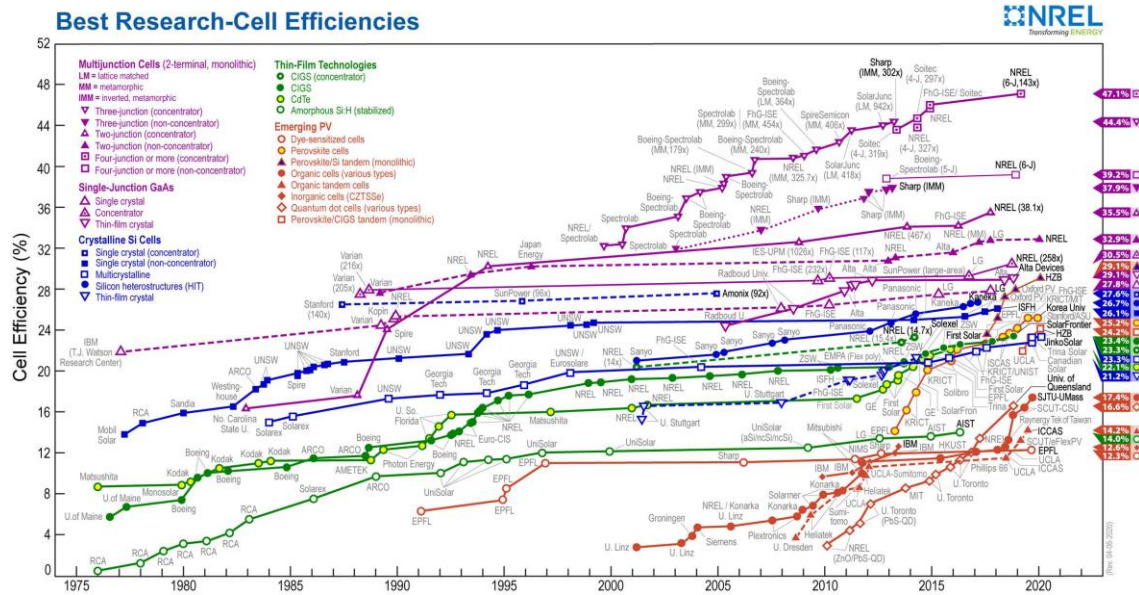


Figure-1.1: solar cell efficiency charts produced by NREL

However, the production cost of the higher solar photovoltaic cell is increasing day by day with the increasing cell efficiency. That's why it is a critical issue to reduce the production cost by compromising with efficiency and using cheaper materials: electrically inferior thin-film semiconductors instead of comparatively more expensive c-Si. To achieve a substantial reduction in cost, low materials cost, low temperature, low vacuum processing, easy and cheap equipment installation, and higher throughput makes “thin-film” technologies are needed. The composite semiconductors, like Copper Indium Gallium Selenide (CIGS), Cadmium Telluride (CdTe), and amorphous-Si (a-Si) technologies are prominent examples of this approach.

Another approach is to prepare thin-film solar cell devices from organic semiconducting polymers. In place of typical conduction and valance band, which are observed in inorganic materials, they have inter-molecular filled, and empty energy states referred to as the highest-occupied-molecular-orbital (HOMO) and the lowest-unoccupied-molecular-orbital (LUMO) respectively. The typical energy gap (E_g) of

organic materials $\sim 2\text{-}3$ eV, which is much higher than the c-Si (1.1 eV). This type of PV cell has several advantages, including low production cost, high throughput, flexible thin-film, and can be prepared by roll-to-roll processes, such as lamination, spray-coating, or transfer printing [3]. Due to the low cost, several types of organic-based solar cells have been proposed [4]. However, since semiconducting polymers absorb only in a small spectral range of the solar spectrum [5-6], the PCE of these types of solar cells is too low, and their reliability is still poor [7-10].

1.2 Crystalline-Si/Organic Heterojunction Solar Cells

In recent years, the combination of organic and inorganic materials has an attractive significant research interest in c-Si hybrid solar cells due to their obvious advantages of a low-temperature process, remarkably low fabrication cost, and potential high efficiency [11-14]. Hybrid photovoltaic (PV) cells are low temperature processable ($<140^{\circ}\text{C}$) like most-organic solar cells and have simple fabrication such as spin coating (SC) or mist coating of organic polymer on c-Si, followed by screen printing or evaporated electrodes with high processing speed. Like traditional Si-based solar cells, light absorption and separation of photogenerated carriers happen predominantly in silicon; as a result, the recombination losses are low, and the light absorption is high in these hybrid solar cells compared to the organic PVs.

1.3. Background of the Solution-Processed Hybrid PVs

Recently c-Si/Organic hybrid solar cells with a conductive polymer, such as poly(3-hexylthiophene) (P3HT)/Si, Spiro-OMeTAD/Si and poly(3,4-ethylenedioxythiophene):poly(styrenesulfonate) (PEDOT:PSS)/Si, have been lead to the emerging research field of the hybrid optoelectronic device [15-17]. In this type of hybrid solar cells,

the PEDOT:PSS layer acts as a hole-transporting path [18] when forming a heterojunction with the n-type Silicon (n-Si) substrate. Si has a strong absorption capability in a very wide spectral range and excellent carrier transportability. PEDOT:PSS is a water-soluble polymer that has high conductivity, a transmission window in the visible spectral range, and excellent chemical and thermal stability. This type of n-Si/PEDOT:PSS heterojunction hybrid solar cell combines the excellent absorption property of Si in a wide spectrum range and the benefit of aqueous solution-based processes of PEDOT:PSS. This type of heterojunction can be formed by solution-based fabrication techniques such as Spin-coating (SC), chemical mist deposition (CMD), electrospray deposition, and inkjet of polymer on c-Si [19-24].

The molecular structure of the PEDOT:PSS is shown in figure 1.2. The polythiophene based conjugated polymer PEDOT carries a positive charge and shows hydrophobic behavior. On the other hand, sulfonated polystyrene PSS shows negative charge behavior because of having a deprotonated sulfonate group and has hydrophilic characteristics.

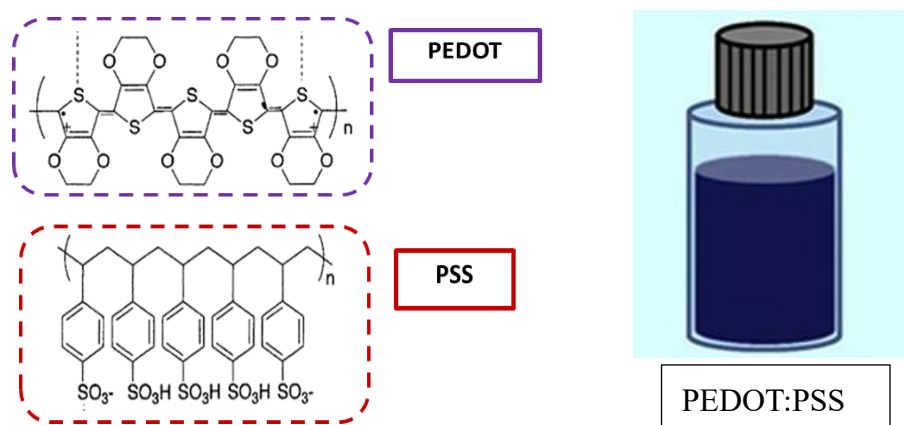


Figure-1.2: Molecular structure of PEDOT and PSS

Figure-1.3 shows the PV progress of PEDOT:PSS/n-Si solar cells with time. The PCE of 10.8% ~ 13.3% has been explored in plain Si substrate by adjusting the type of solvents (e.g., methanol (MeOH), ethylene glycol (EG), mixed of MeOH/EG, dimethyl sulfoxide (DMSO)), solution concentration, the thickness of the PEDOT:PSS, and resistivity of the substrate [25-28]. The efficiency was farther improved to 15.4% by introducing the antireflection (AR) overcoating without additional light management (texturing, pillar) system [29]. Most recently, the PCE of PEDOT:PSS/c-Si solar cells increased to over 20% with a back-PEDOT structure in textured Si substrate, but it required conventional high-temperature processing steps [32].

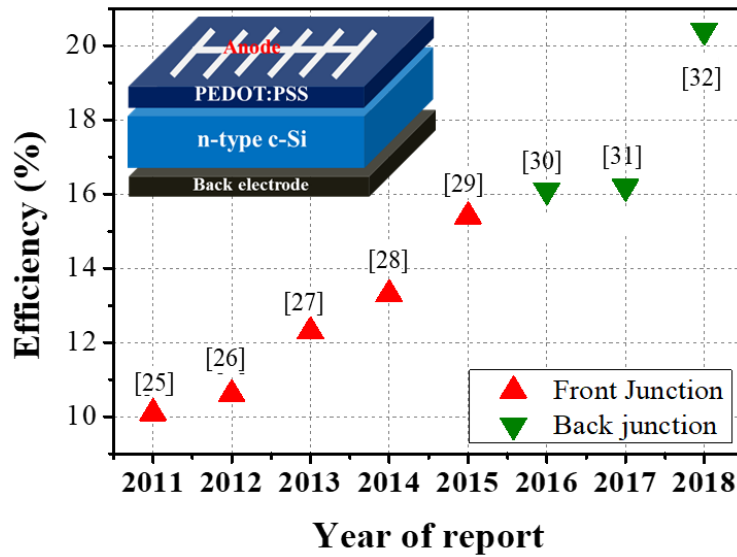


Figure-1.3: Efficiency progress of PEDOT:PSS/n-Si solar cells with time

1.4 Motivation of this study

In recent times, highly efficient organic-inorganic hybrid solar cells utilizing organic (PEDOT:PSS) combined with n-Si have attracted much attention for their reasonable cell conversion efficiency and cost-effective fabrication [33–39]. The PEDOT:PSS layer acts as a hole transporting path when forming a heterojunction with n-

type Si. Over the past few years, considerable progress towards high-efficiency n-Si/PEDOT:PSS hybrid solar cells has been achieved by adjusting significant factors such as electrical conductivity, chemical affinity, interfacial layers, and the thickness of the materials [40-49]. Despite the tremendous efforts to improve solar cell performance, the highest power conversion efficiency reported to date is low when compared to the value (33%) theoretically estimated by Shockley–Queisser for a single-junction device [50]. To further increase the PCEs in heterojunction hybrid solar cells, the interfacial engineering between the n-Si and PEDOT:PSS is of significant importance. This is because photogenerated charge carriers must effectively pass through the heterojunction interface. Therefore, it is crucial to form a high-quality oxide interlayer at that interface. With the objective of this, an additional passivation layer may be applied to improve the understanding of the passivation and junction properties at anode or cathode interface. In the case of the cathode interface, many researchers, including our research group, have used several carrier selective contacts like SiO_x , SiN_x , or TiO_x to improve the junction quality. In our study, we also used the TiO_x as a hole blocking layer at the cathode interface to improve the passivation quality as well as the junction quality.

However, the passivation ability of PEDOT:PSS on the n-Si substrate still remains insufficient compared with those of the SiO_2 , SiN_x , or TiO_x dielectrics.[51-53] Although high PCE over 20.6 % has been established for PEDOT:PSS/n-Si (native oxide) heterojunction solar cells by Zielke et al. succeeded in increasing the PCE of PEDOT:PSS/n-Si(native oxide) heterojunction solar cells to over 20.6% without the use of an additional tunnel oxide layer [54], but the role of native oxide is still not clear. Additionally, the PCE of a device on thermally grown SiO_2 /n-Si rather than the native oxide was reportedly 10–13% lower.[51,52] Thus, the interface chemistry of SiO_x local chemical bond configurations at the PEDOT:PSS/n-Si junction remains controversial in

terms of improving the passivation ability and enhancing the field– inversion. Various studies have extensively employed ultrathin metal oxide layers as carrier selective contact layer. These layers were obtained using various fabrication methods, such as thermal evaporation [55-57], plasma-enhanced chemical vapor deposition [58-64], atomic layer deposition (ALD) [65-67], and sputtering [68-71]. Among the metal oxides, ALD- AlO_x is well-known as a good material for the passivation layer at the anode contact for c-Si. Figure-1.4 shows the property of several high- k materials with their corresponding band offset corresponds to the c-Si from which we choose AlO_x due to high dielectric constant.

Material	Dielectric constant (κ)	Band gap E_G (eV)	ΔE_C (eV) to Si	Crystal structure(s)
SiO_2	3.9	8.9	3.5	Amorphous
Si_3N_4	7	5.1	2.4	Amorphous
Al_2O_3	9	8.7	2.8 ⁿ	Amorphous
Y_2O_3	15	5.6	2.3 ⁿ	Cubic
La_2O_3	30	4.2	2.3 ⁿ	Hexagonal, cubic
Ta_2O_3	26	4.5	1-1.5	Orthorhombic
TiO_2	80	3.5	1.2	Tetrag. ^c (rutile, anatase)
HfO_2	25	5.7	1.5 ⁿ	Mono. ^b , Tetrag. ^c , cubic
ZrO_2	25	7.8	1.4 ⁿ	Mono. ^b , Tetrag. ^c , cubic

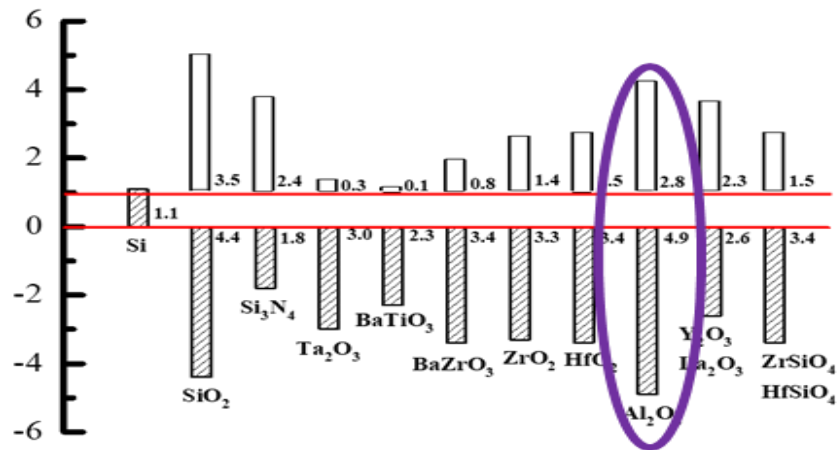


Figure-1.4: Property of several high- k materials with their band offset. [G.D. Wilk et al., J. Appl. Phys.10, 15 (2001)]

To achieve this aim, we have investigated the PEDOT:PSS/n-Si junction by inserting a higher passivation layer of AlO_x to improve its junction quality by suppressing the fermi level pinning as well as the reducing of the sheet resistance produced at PEDOT:PSS/n-Si junction. Although a higher passivation layer can be achieved due to the higher thickness of AlO_x , at the same time, due to the thicker AlO_x , the photogenerated carriers have difficulty to be tunneled through the thick inversion layer. Several attempts using an ALD- AlO_x /PEDOT:PSS combined stack hole-selective layer have been made to increase the passivation ability as well as the built-in-field V_{bi} at the PEDOT:PSS/n-Si anode interface. These attempts include photolithography-processed ALD- AlO_x islands with different gap distances on highly resistive c-Si and an ultrathin ALD- AlO_x /chemical tunnel oxide ($ch\text{-SiO}_x$) stack layer at the PEDOT:PSS/n-Si interface. In case of a higher thickness of ALD- AlO_x film, a UV photolithography process has been introduced to apply an AlO_x island to make a tunnel layer through a thick AlO_x layer where the photogenerated carriers easily pass through the tunneling. Figure-1.5(a) shows a proposed band diagram of AlO_x /n-Si interface, where the negative fixed charge density is stored underneath the inversion layer of AlO_x . Figure-1.5(b) shows the proposed device structure where the photogenerated holes are transported through the AlO_x island layer to the passivated PEDOT:PSS contact, while the electron reaches the back contact via the Si substrate. In this study, the different area ratio of ALD- AlO_x island has been introduced with the overlayer of PEDOT:PSS to improve the junction quality.

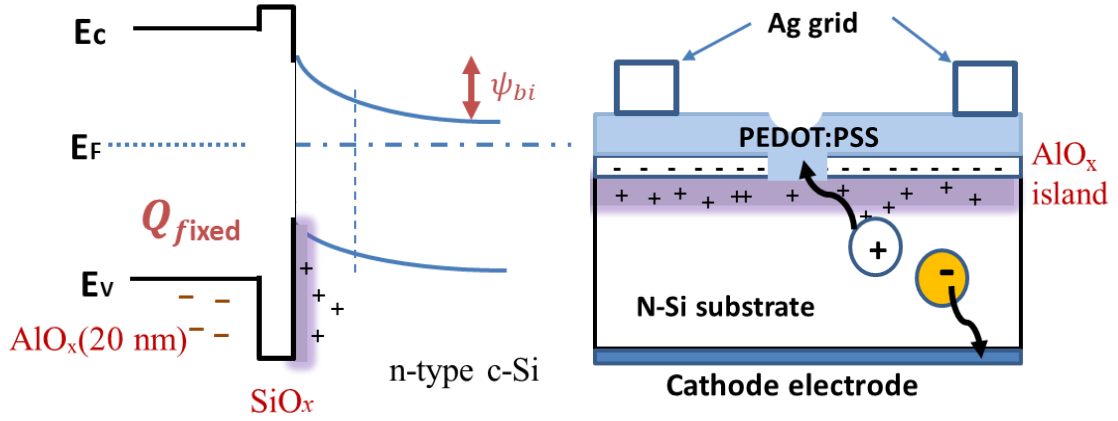


Figure-1.5: (a) Schematic band diagram of $\text{AlO}_x/\text{n-Si}$ interface and (b) proposed device diagram of PEDOT:PSS/ AlO_x island/ n-Si HT solar cells.

However, another researcher has investigated that the photovoltaic performance is sensitive to the ratio of the area of PEDOT:PSS to that of ALD- AlO_x , and the layer thicknesses, and the obtained PCE remains low at 4–5 %.[57] When the former approach is used, the photovoltaic performance is sensitive to the ratio of the area of PEDOT:PSS to that of ALD- AlO_x , and the layer thicknesses, and the obtained PCE remains low at 4–5 % [57]. Therefore, another approach is the use of ALD- $\text{AlO}_x/\text{ch-SiO}_x$ stack layer at the PEDOT:PSS/ n-Si interface to improve its junction quality. For furthermore improvement of the performance, an additional annealing effect has been introduced at the junction to improve its passivation quality using the forming gas annealing (FGA) in N_2/H_2 gas mixture. [57] Figure-1.6 shows the proposed schematic device and band diagram of the PEDOT:PSS/ n-Si device with and without FGA treated ALD- $\text{AlO}_x/\text{ch-SiO}_x$ stack layer.

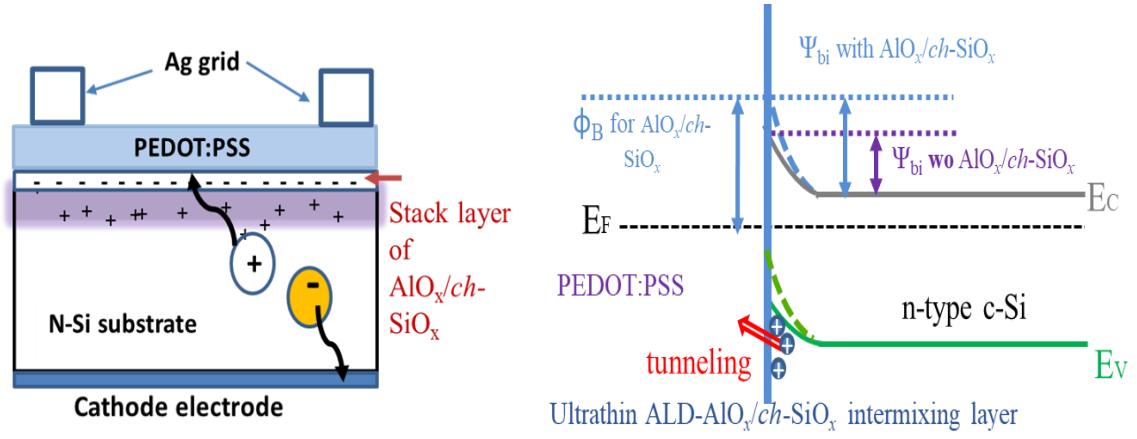


Figure-1.6: Proposed device diagram and its corresponding band diagram of PEDOT:PSS/n-Si junction with and without stack layer of ALD-AlO_x/ch-SiO_x.

However, the impact of FGA on the local Si-O_x chemical bonding configurations and the junction properties at the ALD-AlO_x/n-Si interface has not yet been systematically evaluated. To this aim, we investigated the effects of rapid thermal annealing (RTA) and FGA of ALD-AlO_x on n-Si with and without tunnel oxide *ch*-SiO_x layers on the local SiO_x bonding configurations as well as the junction properties at a PEDOT:PSS/n-Si interface.

1.5 Outline of This Dissertation

In this work, the junction property of the organic/c-Si heterojunction solar cell has been investigated with the selective carrier contacts like TiO_x and AlO_x. The main contribution in this work is the improvement of passivation ability at the PEDOT:PSS/n-Si junction by the insertion of FGA treated ultrathin stacked ALD-AlO_x/SiO_x layer.

In chapter 2, the junction property at the n-type cathode interface has been investigated using a hole blocking layer (HBL) instead of direct metal contact to reduce the recombination at the cathode interface. In this study, the solution-processed TiO_x has been used as a hole blocking layer at the cathode interface, which increased the PCE of the PEDOT:PSS/n-Si solar cell from 11.2 to 13.1% with the increased J_{sc} and V_{oc} . Also, a transient reverse recovery study revealed that the surface recombination velocity could be determined for the PEDOT:PSS/n-Si/ TiO_x double heterojunction solar cell with no use of both side TiO_x coated c-Si samples.

In chapter 3, the detailed experimental procedure characterization method has been explained for the PEDOT:PSS/n-Si heterojunction solar cell with and without ALD- AlO_x layer. In the experimental procedure, firstly, we have explained the detailed fabrication process of PEDOT:PSS/n-Si heterojunction solar cell. After then, the details deposition process of AlO_x by the atomic layer deposition has been discussed. After that, the details fabrication process of AlO_x island at the PEDOT:PSS/n-Si interface has been explained using the UV photolithography process. Following that, the stack layer of ALD- AlO_x /ch-SiO_x related device fabrication process has been discussed in detail. In the next part, the characterization methods have been discussed, including the μ -PCD, Annealing process, AFM, FTIR, C-V profiling, XPS, PYSA, four-probe method, etc.

In chapter-4, first, the fundamental property of ALD- AlO_x on the n-Si substrate are characterized. Also, we have investigated the minority carrier lifetime of ALD- AlO_x /n-Si interface, which depicted the better passivation quality of the c-Si surface. It has been achieved using a higher thickness of ALD- AlO_x layer after rapid thermal annealing (RTA). Thus, we classified two different thickness regimes of ALD- AlO_x . In the case of $\sim 20\text{nm}$ thickness regimes, the AlO_x island has been introduced at

PEDOT:PSS/n-Si heterojunction using the UV photolithography process to pass the photogenerated carriers through the AlO_x island layer. The photocurrent-voltage curve revealed that the current density had been increased for the AlO_x island inserted PEDOT:PSS/n-Si device due to the photocurrent enhancement and suppression of reflectance within the visible spectrum region. On the other hand, using the ultrathin $\text{AlO}_x/\text{SiO}_x$ stack layer on the n-Si substrate, the built-in potential and the open-circuit voltage in the PEDOT:PSS/n-Si heterojunction solar cell has been improved, which is confirmed from the external quantum efficiency, XPS and FTIR study.

In chapter 5, the ultrathin $\text{AlO}_x/\text{SiO}_x$ stack layer on the n-Si substrate has been investigated on the local chemical bonding configuration and the junction properties at the PEDOT:PSS/n-Si interface. Forming gas annealing (FGA) promotes the reduction of AlO_x layer as well as the formation of SiO_x layer, which improves the passivation ability at the PEDOT:PSS/n-Si interface. These results suggest that the negative charge stored in the ALD- AlO_x layer increased because of the removal of oxygen after FGA by reduction. This indicates that both the increased passivation ability and increased negative charge storage in the ALD- AlO_x layer contribute to the increase in V_{bi} at the PEDOT:PSS/n-Si anode interface and increase in V_{oc} in PEDOT:PSS/n-Si heterojunction solar cells.

Bibliography

- [1] Best Research-Cell Efficiency Chart by NREL [online]
“https://www.nrel.gov/pv/cell_efficiency.html.”
- [2] D. M. Chapin, C. S. Fuller, and G. L. Pearson, "A New Silicon p-n Junction Photocell for Converting Solar Radiation into Electrical Power", *Journal of Applied Physics* **25**, 676–677 (1954).
- [3] J. R. Sheats, "Manufacturing and commercialization issues in organic electronics", *Journal of Materials Research* **19**, 1974–1989 (2004).
- [4] J. Y. Kim, K. Lee, N. E. Coates, D. Moses, T.-Q. Nguyen, M. Dante, and A. J. Heeger, "Efficient Tandem Polymer Solar Cells Fabricated by All-Solution Processing," *Science* **317**, 222–225 (2007).
- [5] W. Brütting, ed., *Physics of Organic Semiconductors*. Edited By. (WILEY-VCH Verlag GmbH & Co. KGaA, 2005), Vol. 7.
- [6] A. Moliton and R. C. Hiorns, "Review of electronic and optical properties of semiconducting π -conjugated polymers: applications in optoelectronics", *Polymer International* **53**, 1397–1412 (2004).
- [7] V. Shrotriya, G. Li, Y. Yao, T. Moriarty, K. Emery, and Y. Yang, "Accurate Measurement and Characterization of Organic Solar Cells", *Advanced Functional Materials* **16**, 2016–2023 (2006).
- [8] M. Reyes-Reyes, K. Kim, and D. L. Carroll, "High-efficiency photovoltaic devices based on annealed poly(3-hexylthiophene) and 1-(3-methoxycarbonyl)-propyl-1-phenyl-(6,6)C61 blends", *Applied Physics Letters* **87**, 083506 (2005).
- [9] F. C. Krebs and K. Norrman, "Analysis of the failure mechanism for a stable organic photovoltaic during 10000 h of testing", *Progress in Photovoltaics*

- Research and Applications **15**, 697–712 (2007).
- [10] M. Jørgensen, K. Norrman, and F. C. Krebs, "Stability/degradation of the polymer solar cells," *Solar Energy Materials, and Solar Cells* **92**, 686–714 (2008).
 - [11] S. Avasthi, Y. Qi, G. K. Vertelov, J. Schwartz, A. Kahn, and J. C. Sturm, "Silicon surface passivation by an organic overlayer of 9,10-phenanthrenequinone", *Applied Physics Letters* **96**, 222109 (2010).
 - [12] L. M. Ono, Z. Tang, R. Ishikawa, K. Ueno, and H. Shirai, "Highly efficient crystalline silicon/Zonyl fluorosurfactant-treated organic heterojunction solar cells", *Applied Physics Letters* **100**, 183901 (2012)
 - [13] Q. Liu, F. Wanatabe, A. Hoshino, R. Ishikawa, T. Gotou, K. Ueno, and H. Shirai, "Crystalline Silicon/Graphene Oxide Hybrid Junction Solar Cells," *Japanese Journal of Applied Physics* **51**, 10NE22 (2012)
 - [14] A. T. M. S. Islam, M. E. Karim, A. Rajib, Y. Nasuno, T. Ukai, S. Kurosu, M. Tokuda, Y. Fujii, Y. Nakajima, T. Hanajiri, and H. Shirai, "Chemical mist deposition of organic for efficient front- and back-PEDOT:PSS/crystalline Si heterojunction solar cells," *Applied Physics Letters* **114**, 193901 (2019).
 - [15] J. C. Nolasco, R. Cabré, J. Ferré-Borrull, L. F. Marsal, M. Estrada, and J. Pallarès, "Extraction of poly (3-hexylthiophene) (P3HT) properties from dark current-voltage characteristics in a P3HT/n-crystalline-silicon solar cell", *Journal of Applied Physics* **107**, 044505 (2010).
 - [16] X. Shen, B. Sun, D. Liu, and S.-T. Lee, "Hybrid Heterojunction Solar Cell-Based on Organic-Inorganic Silicon Nanowire Array Architecture", *Journal of the American Chemical Society* **133**, 19408–19415 (2011).
 - [17] S. Avasthi, S. Lee, Y.-L. Loo, and J. C. Sturm, "Role of Majority and Minority Carrier Barriers Silicon/Organic Hybrid Heterojunction Solar Cells", *Advanced*

Materials **23**, 5762–5766 (2011).

- [18] S. Jäckle, M. Mattiza, M. Liebhaber, G. Brönstrup, M. Rommel, K. Lips, S. Christiansen, Junction formation and current transport mechanisms in hybrid n-Si/PEDOT:PSS solar cells. *Sci. Rep.* **5**, 13008 (2015).
- [19] F. C. Krebs, "Fabrication and processing of polymer solar cells: A review of printing and coating techniques," *Solar Energy Materials and Solar Cells* **93**, 394–412 (2009).
- [20] H. Nishinaka, T. Kawaharamura, and S. Fujita, "Low-Temperature Growth of ZnO Thin Films by Linear Source Ultrasonic Spray Chemical Vapor Deposition", *Japanese Journal of Applied Physics* **46**, 6811–6813 (2007).
- [21] D. Khim, H. Han, K.J. Baeg, J. Kim, S.W. Kwak, D.Y. Kim, and Y.Y. Noh, "Simple Bar-Coating Process for Large-Area, High-Performance Organic Field-Effect Transistors, and Ambipolar Complementary Integrated Circuits," *Advanced Materials* **25**, 4302–4308 (2013).
- [22] J. Hossain, T. Ohki, K. Ichikawa, K. Fujiyama, K. Ueno, Y. Fujii, T. Hanajiri, and H. Shirai, "Investigating the chemical mist deposition technique for poly(3,4-ethylene dioxythiophene): poly(styrene sulfonate) on textured crystalline-silicon for organic/crystalline-silicon heterojunction solar cells", *Japanese Journal of Applied Physics* **55**, 031601 (2016).
- [23] T. Ohki, K. Ichikawa, J. Hossain, Y. Fujii, T. Hanajiri, R. Ishikawa, K. Ueno, and H. Shirai, "Effect of substrate bias on mist deposition of conjugated polymer on textured crystalline-Si for efficient c-Si/organic heterojunction solar cells," *Physica status solidi (a)* **213**, 1922–1925 (2016).
- [24] C. K. Chan, L. J. Richter, B. Dinardo, C. Jaye, B. R. Conrad, H. W. Ro, D. S. Germack, D. A. Fischer, D. M. DeLongchamp, and D. J. Gundlach, "High

- performance airbrushed organic thin-film transistors," *Applied Physics Letters* **96**, 133304 (2010).
- [25] S. Avasthi, S. Lee, Y. Loo, J. C. Sturm, "Role of Majority and Minority Carrier Barriers Silicon/Organic Hybrid Heterojunction Solar Cells," *Adv. Mater.* **23**, 5762-5766 (2011)
- [26] L. He, C. Jiang, H. Wang, D. Lai, Rusli, "High-efficiency planar Si/organic heterojunction hybrid solar cells," *Appl. Phys. Lett.* **100**, 073503 1-3 (2012).
- [27] J. Schmidt, V. Titova, and D. Zielke, "Organic-silicon heterojunction solar cells: Open-circuit voltage potential and stability," *Appl. Phys. Lett.* **103**, 183901 (2013).
- [28] J. P. Thomas and K. T. Leung, "Defect - Minimized PEDOT:PSS/Planar - Si Solar Cell with Very High Efficiency," *Adv. Funct. Mater.* **24**, 4978 (2014).
- [29] Q. Liu, R. Ishikawa, S. Funada, T. Ohki, K. Ueno, and H. Shirai, "Highly Efficient Solution - Processed Poly(3,4 ethylenedioxythiophene):Poly (styrenesulfonate)/Crystalline-Silicon Heterojunction Solar Cells with Improved Light - Induced Stability", *Adv. En. Mat.* **5**, 1500744 (2015).
- [30] X. Zhang, D. Yang, Z. Yang, X. Guo, B. Liu, X. Ren, and S. Liu, "Improved PEDOT:PSS/c-Si hybrid solar cell using the inverted structure and effective passivation," *Scientific Reports* **6**, 35091 (2016).
- [31] R. Gogolin, D. Zielke, A. Descoeudres, M. Despeisse, C. Ballif, J. Schmidt, "Demonstrating the high V_{oc} potential of PEDOT:PSS/c-Si heterojunctions on solar cells", *Energy Procedia* **124**, 593–597 (2017).
- [32] D. Zielke, R. Gogolin, M. U. Halbich, C. Marquardt, W. Lövenich, R. Sauer, J. Schmidt, "Large - Area PEDOT:PSS/c-Si Heterojunction Solar Cells With Screen - Printed Metal Contacts", *Solar RRL* **2**, 1700191 (2018).
- [33] Y. .H Kim, C. Sachse, M. L. Machala, C. May, L. Müller-Meskamp and K. Leo

- “Highly conductive PEDOT:PSS electrode with optimized solvent and thermal post-treatment for ITO-free organic solar cells”, *Adv. Funct.Mater.* **21**, 1076–81 (2011).
- [34] L. He, D. Lai, H. Wang, C. Jiang, and Rusli “High-efficiency Si/polymer hybrid solar cells based on synergistic surface texturing of Si nanowires on pyramids Small”, **8**, 1664–8 (2012).
- [35] S. A. Moiz, A. M. Nahhas, H. D. Um, S. W. Jee, H. K. Cho, S. W. Kim, and J. H. Lee, “A stamped PEDOT:PSS silicon nanowire hybrid solar cell Nanotechnology”, **23**, 145401–7 (2012).
- [36] P. R. Pudasaini, F. Ruiz-Zepeda, M. Sharma, D. Elam, A. Ponce, and A. A. Ayon, “high-efficiency hybrid silicon nanopillar-polymer solar cells” *A.C.S. Appl. Mater. Interfaces* **5**, 9620–7 (2013).
- [37] R. Liu, S. T. Lee, and B. Sun “13.8% efficiency hybrid Si/organic heterojunction solar cells with MoO₃ film as antireflection and inversion induced layer” *Adv. Mater.* **26**, 6007–12 (2014).
- [38] K. A. Nagamatsu, S. Avasthi, J. Jhaveri, and J. C. Sturm “A 12% efficient silicon/PEDOT:PSS heterojunction solar cell fabricated at <100 °C” *IEEE J. Photovolt.* **4**, 260–4 (2014).
- [39] S. Wu, W. Cui, N. Aghdassi, T. Song, S. Duhm, S. T. Lee, and B. “Sun Nanostructured Si/organic heterojunction solar cells with high open-circuit voltage via improving junction quality”, *Adv. Funct. Mater.* **26**, 5035–41 (2016).
- [40] A. Elschner, S. Kirchmeyer, W. Lovenich, U. Merker, and K. Reuter “PEDOT: Principles and Applications of an Intrinsically Conductive Polymer”, (Boca Raton, FL: C.R.C. Press), 2011.
- [41] J. P. Thomas and K. T. Leung “Defect-minimized PEDOT:PSS/planar-Si solar cell

- with very high-efficiency”, *Adv. Funct. Mater.* **24**, 4978–85 (2014).
- [42] Y. Zhang, F. Zu, S. T. Lee, L. Liao, N. Zhao, and B. Sun “Heterojunction with thin organic layers on silicon for record efficiency hybrid solar cells” *Adv. Energy Mater.* **4**, 1300923–9 (2014).
- [43] K. T. Park, H. J. Kim, M. J. Park, J. H. Jeong, J. H. Lee, D. G. Choi, J. H. Lee and J. H. Choi “13.2% efficiency Si nanowire/PEDOT:PSS hybrid solar cell using a transfer-imprinted Au mesh electrode”, *Sci. Rep.* **5**, 12093–101 (2015).
- [44] X. Mu, X. Yu, D. Xu, X. Shen, Z. Xia, H. He, H. Zhu, J. Xie, B. Sun and D. Yang “High-efficiency organic/silicon hybrid solar cells with doping-free selective emitter structure induced by a WO₃ thin interlayer”, *Nano Energy* **16**, 54–61 (2015).
- [45] Y. Zhang, W. Cui, Y. Zhu, F. Zu, L. Liao, S. T. Lee and B. Sun “High-efficiency hybrid PEDOT:PSS/nanostructured silicon Schottky junction solar cells by doping-free rear contact”, *Energy Environ. Sci.* **8**, 297–302 (2015).
- [46] S. I. Na, G. Wang, S. S. Kim, T. W. Kim, S. H. Oh, B. K. Yu, T. Lee, and D. Y. Kim “Evolution of nanomorphology and anisotropic conductivity in solvent-modified PEDOT:PSS films for polymeric anodes of polymer solar cells”, *J. Mater. Chem.* **19**, 9045–53 (2009).
- [47] X. Shen, Y. Zhu, T. Song, S. T. Lee, and B. Sun “Hole electrical transporting properties in organic-Si Schottky solar cell”, *Appl. Phys. Lett.* **103**, 013504 (2013).
- [48] S. Jäckle, M. Liebhaber, J. Niederhausen, M. Büchele, R. Félix, R. G. Wilks, M. Bär, K. Lips and S. Christiansen “Unveiling the hybrid n-Si/PEDOT:PSS interface”, *A.C.S. Appl. Mater. Interfaces* **8**, 8841–8 (2016).
- [49] P. Yu “13% efficiency hybrid organic/silicon nanowire heterojunction solar cell via interface engineering”, *A.C.S. Nano* **7**, 10780–7 (2013)

- [50] S. Zhang, Y. Yao, D. Hu, W. Lian, H. Qian, J. Jie, Q. Wei, Z. Ni, X. Zhang, and L. Xie “Application of silicon oxide on high efficiency monocrystalline silicon PERC solar cells”, *Energies*, **12**, 1168. (2019).
- [51] J. Sheng, K. Fan, D. Wang, C. Han, J. Fang, P. Gao, and J. Ye, “Improvement of the SiO_x Passivation Layer for High-Efficiency Si/PEDOT:PSS Heterojunction Solar Cells“, *ACS Appl. Mater. Interfaces*, **6**, 16027-16034 (2014).
- [52] C. Zhang, Y. Zhang, H. Guo, Q. Jiang, P. Dong, and C. Zhang, “Efficient Planar Hybrid n-Si/PEDOT:PSS Solar Cells with Power Conversion Efficiency up to 13.31% Achieved by Controlling the SiO_x Interlayer”, *Energies*, **11**, 1397 (2018).
- [53] J. He, P. Gao, Z. Ling, L. Ding, Z. Yang, J. Ye, and Y. Cui, “High-Efficiency Silicon/Organic Heterojunction Solar Cells with Improved Junction Quality and Interface Passivation”, *ACS Nano*, **10**, 12, 11525-11531 (2016).
- [54] D. Zielke, C. Neihaves, W. Lovenich, A. Elschner, M. Horteis, and J. Schmidt, 5th International Conference on Silicon Photovoltaics, SiliconPV 2015, “ Organic-silicon solar cells are exceeding 20% efficiency”, *Energy Procedia* **77**, 331– 339 (2015).
- [55] Y. Zhang, R. Liu, S.-T. Lee, and B. Sun, “The role of a LiF layer on the performance of poly(3,4-ethylenedioxythiophene):poly(styrenesulfonate)/Si organic-inorganic hybrid solar cells”, *Appl. Phys. Lett.* **104**, 83514, (2014).
- [56] J. Bullock, M. Hettick, J. Geissbühler, A.J. Ong, T. Allen, C.M. Sutter-Fella, T. Chen, H. Ota, E.W. Schaler, S. De Wolf, C. Ballif, A. Cuevas, and A. Javey, “Efficient silicon solar cells with dopant-free asymmetric heterocontacts,” *Nat. Energy* **1**, 15031 (2016).
- [57] J. Bullock, P. Zheng, Q. Jeangros, M. Tosun, M. Hettick, C.M. Sutter-Fella, Y. Wan, T. Allen, D. Yan, D. Macdonald, S. De Wolf, A. Hessler-Wyser, A. Cuevas,

- and A. Javey, “Lithium Fluoride Based Electron Contacts for High-Efficiency n-type Crystalline Silicon Solar Cells”, *Adv. Energy Mater.* **6**, 1600241, (2016).
- [58] Y. Wan, C. Samundsett, J. Bullock, T. Allen, M. Hettick, D. Yan, P. Zheng, X. Zhang, J. Cui, J. McKeon, A. Javey, and A. Cuevas, “Magnesium Fluoride Electron-Selective Contacts for Crystalline Silicon Solar Cells”, *ACS Appl. Mater. Interfaces* **8**, 14671 (2016).
- [59] H.J. Frenck, W. Kulisch, M. Kuhr, and R. Kassing, “Deposition of TiO₂ thin films by plasma-enhanced decomposition of tetraisopropyltitanate”, *Thin Solid Films* **201**, 327 (1991).
- [60] W.G. Lee, S.I. Woo, J.C. Kim, S.H. Choi, and K.H. Oh, “Preparation and properties of amorphous TiO₂ thin films by plasma-enhanced chemical vapor deposition”, *Thin Solid Films* **237**, 105 (1994).
- [61] W. Yang and C.A. Wolden, “Plasma-enhanced chemical vapor deposition of TiO₂ thin films for dielectric applications”, *Thin Solid Films* **515**, 1708 (2006).
- [62] D. Li, M. Carette, A. Granier, J.P. Landesman, and A. Goullet, “Spectroscopic ellipsometry analysis of TiO₂ films deposited by plasma-enhanced chemical vapor deposition in oxygen/titanium tetraisopropoxide plasma”, *Thin Solid Films* **522**, 366 (2012).
- [63] D. Li, M. Carette, A. Granier, J.P. Landesman, and A. Goullet, “In situ spectroscopic ellipsometry study of TiO₂ films deposited by plasma-enhanced chemical vapor deposition”, *Appl. Surf. Sci.* **283**, 234 (2013).
- [64] K. L. Ou, D. Tadytin, K. Xerxes Steirer, D. Placencia, M. Nguyen, P. Lee, and N.R. Armstrong, “Titanium dioxide electron-selective interlayers created by chemical vapor deposition for inverted configuration organic solar cells”, *J. Mater. Chem. A* **1**, 6794 (2013).

- [65] S. McDonnell, R.C. Longo, O. Seitz, J.B. Ballard, G. Mordi, D. Dick, J.H.G. Owen, J.N. Randall, J. Kim, Y.J. Chabal, K. Cho, and R.M. Wallace, “Controlling the Atomic Layer Deposition of Titanium Dioxide on Silicon: Dependence on Surface Termination”, *J. Phys. Chem. C* **117**, 20250-20259 (2013).
- [66] B. Liao, B. Hoex, A.G. Aberle, D. Chi, and C.S. Bhatia, “Excellent c-Si surface passivation by low-temperature atomic layer deposited titanium oxide”, *Appl. Phys. Lett.* **104**, 253903, (2014).
- [67] L. Tian, A. Soum-Glaude, F. Volpi, L. Salvo, G. Berthomé, S. Coindeau, A. Mantoux, R. Boichot, S. Lay, V. Brizé, E. Blanquet, G. Giusti, and D. Bellet, “Undoped TiO₂ and nitrogen-doped TiO₂ thin films deposited by atomic layer deposition on planar and architected surfaces for photovoltaic applications”, *J. Vac. Sci. Technol. A* **33**, 01A141 (2015).
- [68] R. Dannenberg and P. Greene, “Reactive sputter deposition of titanium dioxide”, *Thin Solid Films* **360**, 122 (2000).
- [69] A.A. Akl, H. Kamal, and K. Abdel-Hady, “Fabrication and characterization of sputtered titanium dioxide films”, *Appl. Surf. Sci.* **252**, 8651 (2006).
- [70] J. Kischkat, S. Peters, B. Gruska, M. Semtsiv, M. Chashnikova, M. Klinkmüller, O. Fedosenko, S. Machulik, A. Aleksandrova, G. Monastyrskyi, Y. Flores, and W.T. Masselink, “Mid-infrared optical properties of thin films of aluminum oxide, titanium dioxide, silicon dioxide, aluminum nitride, and silicon nitride”, *Appl. Opt.* **51**, 6789 (2012).
- [71] M. Sakamoto, E. Kusano, and H. Matsuda, “Structure modification of titanium oxide thin films by rf-plasma assistance in Ti–O₂ reactive dc and pulsed dc sputtering”, *Thin Solid Films* **531**, 49-55 (2013).
- [72] A. S. Erickson, N.K. Kedem, A.E. Haj-Yahia, and D. Cahen, “Aluminum oxide–

n-Si field-effect inversion layer solar cells with organic top contact”, Appl. Phys. Lett., **101**, 233901, (2012).

Chapter 2

Effect of TiO₂ as a Hole Blocking Layer in the PEDOT:PSS/n-Si Heterojunction Solar Cells

2.1. Introduction

The selective carrier layer using metal oxide and organic for crystalline (c-) Si photovoltaics have extensively studied to replace the traditional high-temperature p-n junction and low-pressure processing. They include aluminum oxide (Al₂O₃), NiO, graphene oxide, and transparent conductive polymer poly(3,4-ethylenedioxythiophene):poly(styrene sulfonate) (PEDOT:PSS) as an electron blocking layer (EBL). Among them, solution-processed PEDOT:PSS acts as good passivation of c-Si and as a transparent hole transporting layer, which induces a strong inversion at the PEDOT:PSS/n-Si interface without any additional impurity doping. Thus, the junction property at the PEDOT:PSS/n-Si interface is explained in terms of p⁺-n junction model [1-3]. On the other hand, the band bending at the rear cathode interface is still less than the anode interface despite the use of low work function metal [4-6]. To this aim, several interfacial materials which act as a carrier selective layer (ESL) also have been extensively studied using transition metal oxide and fluorinated alkali metal such as magnesium oxide (MgO) [7], titanium oxide (TiO₂) [8-13], barium hydroxide (Ba(OH)₂) [14,15], cesium carbonate (Cs₂CO₃) [16,17], lithium fluoride (LiF) [18,19], magnesium fluoride (MgF₂) [20] and so on. Among them, TiO₂ on Si (100) has been shown to blocks holes ($\Delta E_V \geq 2.3$ eV) while being transparent to electrons ($\Delta E_C < 0.3$ eV), which acts as a hole blocking layer (HBLs). Several deposition methods have been applied for the fabrication of TiO₂ thin films such as PE-CVD [21-24], metal-organic chemical vapor deposition (MO-CVD) [21], pulsed laser

deposition (PLD) [22], atomic layer deposition (ALD) [23-25], sputtering [26], and sol-gel [27], etc. Among them, ALD of TiO_2 has been extensively studied, and effective minority carrier recombination velocities below 10 cm/s have been achieved [23-25]. However, the potential of solution-processed TiO_2 as an HBL for the n-Si heterojunction solar cells is still not clear.

In the chapter, the potential of solution-processed TiO_2 as an HBL on the photovoltaic performance of PEDOT:PSS/n-Si/ TiO_2 double heterojunction solar cells has been revealed. In this work, two investigations have been studied. One is the understanding of the junction property of the n-Si/ TiO_2 cathode interface, and another is the transient reverse recovery T_{rr} measurement to determine the effective surface recombination velocity S at the n-Si/ TiO_2 interface.

2.2 Experimental Details

2.2.1 Solution-processed TiO_2 and the device fabrication

Figure 1 shows the chemical structure of PEDOT:PSS and device structure of PEDOT:PSS/n-Si/ TiO_2 double heterojunction solar cells with TiO_2 as a hole blocking layer. As a base substrate, a both-side-polished $2 \times 2 \text{ cm}^2$ size n-type (100) CZ c-Si wafers ($1\text{--}5 \text{ } \Omega \cdot \text{cm}$) with a thickness of 250 μm was used. Prior to the film deposition, the n-Si substrates were ultrasonically cleaned with acetone, isopropanol, and DI-water for 10 min each, followed by 5 wt.% HF_{aq} treatment for 3 min to remove the native oxide. At first step, a solution of PEDOT:PSS (prepared from Clevios^R PH1000 by adding ethylene-glycol and capstone fluorosurfactant in the ratio of 93:7:0.16 wt.% respectively) was spin-coated (SC) on top of the cleaned n-Si substrate. After then, the solution coated sample is followed by thermal annealing at 140 °C for 30 min to remove the residual solvent. Then Ag grid electrodes were screen printed at the top of PEDOT:PSS and on the rear side of

the n-Si. In the next step, the precursor solution of titanium tetraisopropoxide [Ti(OCH(CH₃)₂)₄: TiP] diluted in isopropyl alcohol at three different concentrations of 0.5, 1, and 2 mg/ml was spin-coated at 3000 rpm for 40 sec on the rear side of n-Si. After then, the samples are followed by thermal annealing at 140°C for 10 min to remove the residual solvent. A hydrolysis reaction described below was applied to synthesize titanium dioxide on n-Si substrate as a HBL [28]



The two types of device structures were fabricated as shown in Fig 1(b). One is the single layer of PEDOT:PSS/n-Si/TiO₂ double heterojunction solar cells with a 2-nm-thickness by adjusting the solution concentration on the top of Ag grid electrode. The other is the alternate coating of 1-nm-thick TiO₂ layer to suppress the junction area at the Ag/n-Si contact. Thus, a 1-nm-thick TiO₂ was formed first on the n-Si substrate, followed by the screen print of Ag grid electrode. After that, another 1-nm-thick TiO₂ was spin-coated on the top of Ag grid/TiO₂/n-Si structure. The total thickness of TiO₂ was set to be ~2 nm. Finally, the Al was evaporated in the entire area of the rear side as the cathode electrode.

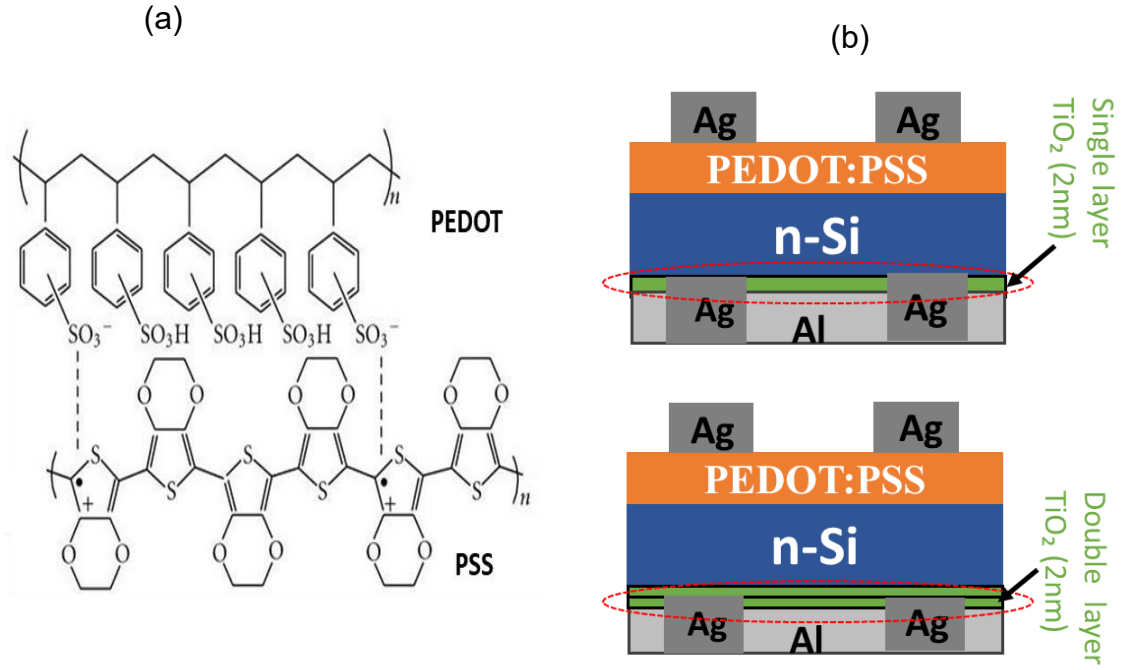


Figure 2.1: (a) PEDOT:PSS chemical structure, (b) Schematic structure of the PEDOT:PSS/n-Si/TiO₂ double heterojunction solar cells with single- and double-TiO₂ layers as a HBL.

The photovoltaic performance was characterized in the dark and under light exposure with simulated solar light of AM1.5G, 100 mW/cm² [Bunkoukeiki (CEP-25BX)]. The two-dimensional (2D) map of EQE at 1000 nm was also characterized for devices with a 2×2 cm² area using a Lasertec: MP Series.

2.3 Characterizations

The junction property at the TiO₂/n-Si cathode interface was characterized using atomic force microscopy (AFM), X-ray photoemission spectroscopy (XPS), and effective minority carrier lifetime τ_{eff} . Also, electroluminescence characterization was used to

determine the transverse recovery time using the solar cell structure under the dark current injection at the forward bias condition.

2.3.1 XPS study

For the XPS measurement, a monochromatized Al K_{α} radiation of $h\nu = 1486.6$ eV [AXIS-Nova (Kratos Analytical)] was used for analyzing the Ti(2p) and Si(2p) related components like Ti^{4+} . In figure-2.2(a), the XPS Ti(2p) scan spectra for TiO_2/n -Si interface provides the Ti^{4+} having a binding energy of 458.6 eV for $2p_{3/2}$ and 464.7 eV for $2p_{1/2}$. These results confirm the formation of the TiO_2 layer at the top of the n-Si substrate. Figure-2.2(b) shows the XPS Ti(2p) scan spectra for the Al/ TiO_2 /n-Si interface, where some additional Ti^{3+} peaks appeared together with Ti^{4+} peak. This analysis provides evidence that the stoichiometric TiO_2 film changes chemically into a complex oxide, which may lead to decorate the hole-blocking effect of the TiO_2 layer and may reduce the passivation quality.

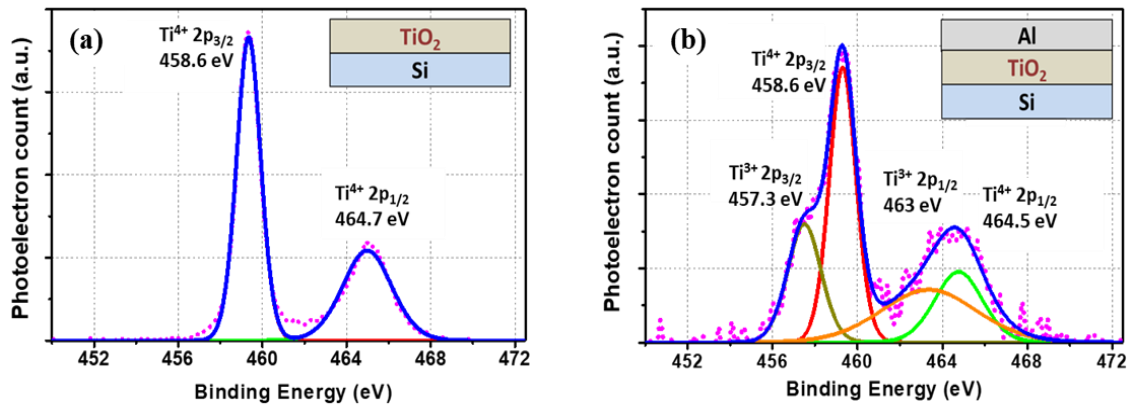


Figure 2.2: XPS profile of the Ti(2p) core levels of, (a) TiO_2/n -Si, and (b) Al/ TiO_2 /n-Si, samples.

2.3.2 Minority Carrier Lifetime

The effective minority career lifetime was determined for the n-Si/TiO₂ junction using a micro-photoconductive decay (μ -PCD) method (SLT-1410A, KOBELCO). Here 10 nm thick TiO₂ layer is symmetrically spin-coated on both sided plane n-Si (1-5 $\Omega \cdot \text{cm}$) substrates, followed by thermally annealed at 140 °C for 10 min. Figure- 2.3 shows the minority career lifetime mapping of n-Si substrate with and without uniformly spin-coated TiO₂.

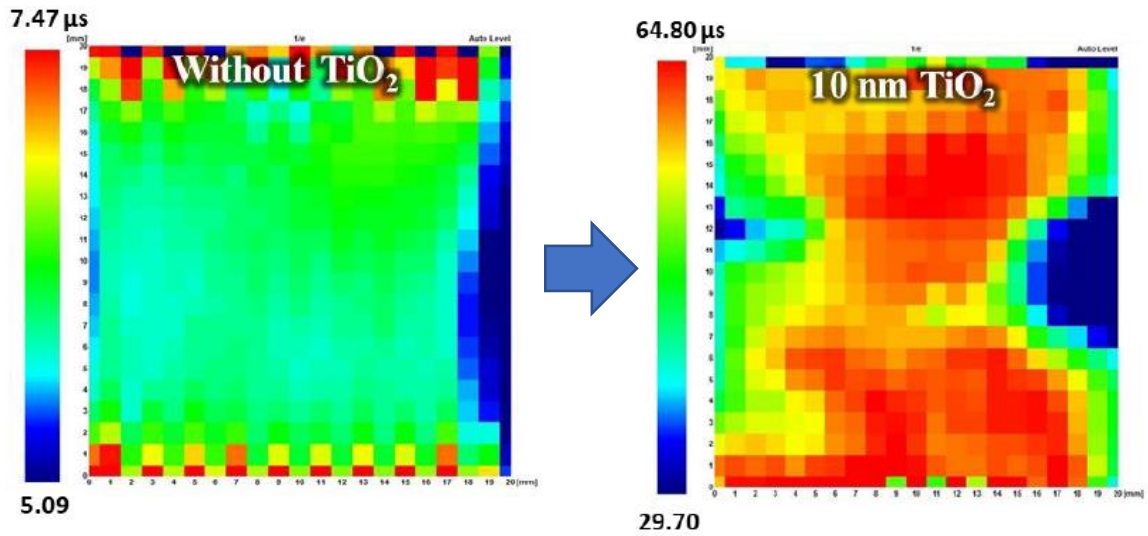


Figure-2.3: 2D mapping of minority career lifetime for the TiO₂ coated n-Si substrate

2.3.3 Transient reverse recovery (T_{rr}) measurement

For determining the surface recombination velocity (S), μ -PCD method is used on both sides symmetrically TiO₂ coated samples. But for the completed solar device, S can be determined by T_{rr} measurement. Figure-2.4 shows the (a) circuit diagram used for the T_{rr} study, and (b) expected output current. Here, V_{ts} is the transient bias source, R_L (100 Ω) is the external load resistance, the blue dash line area represents the simple equivalent circuit of the solar cell device, R_s and R_{sh} are equivalent series and shunt

resistance respectively. The detail of the T_{rr} measurement is described in refs. 29 and 30.

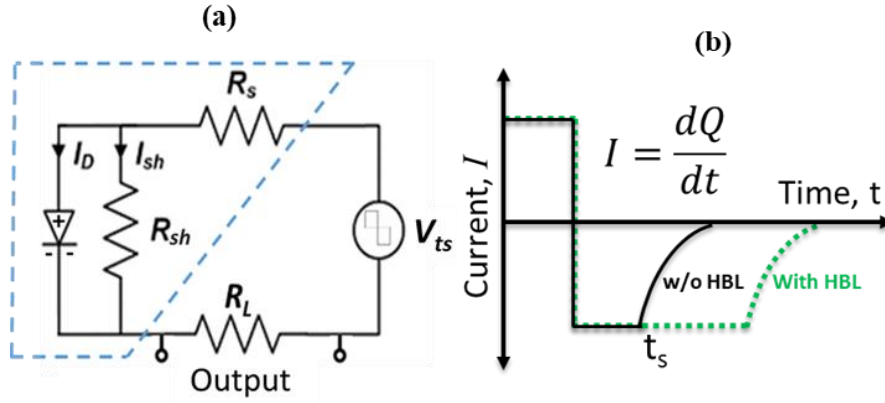


Figure 2.4: Schematics of (a) the circuit diagram and (b) T_{rr} current for the devices with and without HBLs.

First, a positive V_{ts} higher than the built-in potential is applied to the circuit to achieve a steady forward current level I_D and I_{sh} . After that, the reverse bias is applied to a device under test, and the time of recovery to the steady-state was monitored by combining the programmable rectangle wave (WW2074 model of Tabor Electronics) of 1 KHz and the digital storage oscilloscope (DSO7054A model of Agilent Technologies). The amount of stored charge inside the bulk can be calculated by:

$$Q = It_s \quad (2.2)$$

where I is the maximum current and t_s is the storage time. Here, $I_{si/HBL}$ ($t_{si/HBL}$) and I_{si} (t_{si}) are the transient currents (storage times) for the devices with and without HBLs. The storage charge ratio can be determined by:

$$Q_{ratio} = \frac{Q_{Si/HBL}}{Q_{Si}} = \frac{I_{Si/HBL} t_{Si/HBL}}{I_{Si} t_{Si}} \quad (2.3)$$

$$\text{If, } I_{Si/HBL} \approx I_{Si}, \quad Q_{ratio} = \frac{t_{Si/HBL}}{t_{Si}} \quad (2.4)$$

The Q_{ratio} can be obtained through the diffusion coefficient D_p and recombination

velocity S as follows:

$$Q_{ratio} = 2 \frac{D_p}{WS} + 1 \quad (2.5)$$

$$S = \frac{2D_p}{W(Q_{ratio} - 1)} \quad (2.6)$$

Thus, the S value can be calculated by determining the Q_{ratio} without calculating the exact amount of excess hole density of each, although the effect of the bulk recombination is neglected. The τ_{eff} value was also calculated by the μ -PCD using the following well-known equation to confirm the reliability of S value [31]:

$$S = \frac{WD\pi^2}{2(D\pi^2\tau_s - W^2)}, \quad (2.7)$$

Where W is the thickness of the Si substrate, D is the minority carrier diffusion constant of n-Si.

2.4 Results and discussion

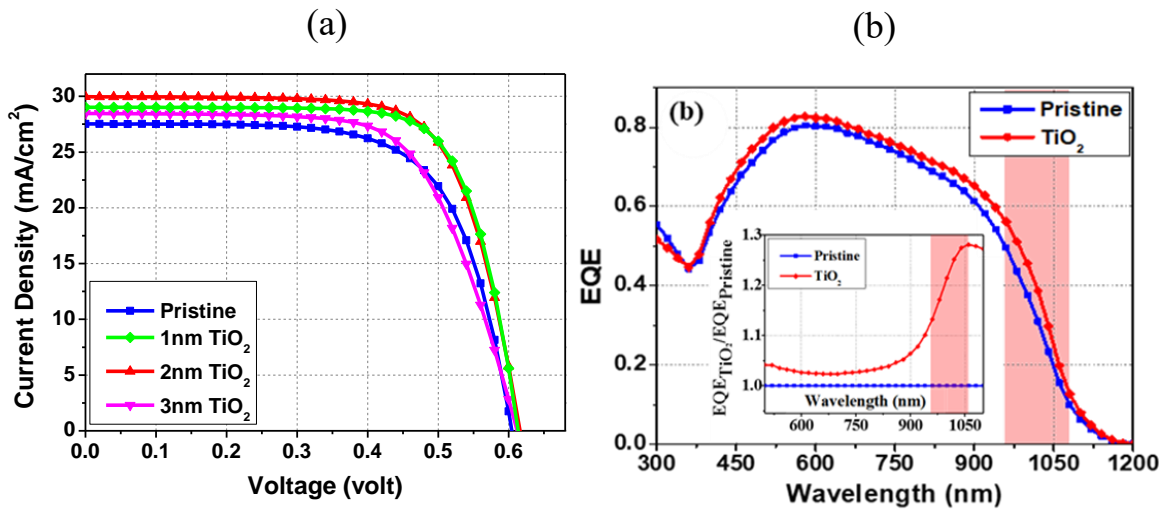
2.4.1 Photovoltaic performance of solar cells

Figures-2.5(a) shows the photocurrent-voltage (J-V) characteristics of the pristine PEDOT:PSS/n-Si heterojunction solar cells without and with different thicknesses of 1-, 2-, and 3-nm TiO_2 under AM1.5G simulated solar light exposure. The photovoltaic parameters for the corresponding devices are summarized in Table 2.1. For 1-2 nm thick TiO_2 layer inserted devices, the current density (J_{sc}) increased from 27.53 to 30 mA/cm^2 with increasing FF and V_{oc} . These findings originate from the enhancement of hole blocking capability at the cathode interface by inserting a TiO_2 layer. As a result, the PCE increased from 11.23 for the pristine to 13.08% for TiO_2 HBL inserted device by

adjusting a ~ 2 nm thick TiO_2 layer.

Figure 2.5(b) presents the EQE for the PEDOT:PSS/n-Si devices with and without a 2-nm-thick TiO_2 HBL layer. The inset figure shows the normalized EQE of the corresponding device. The EQE at the n-Si/cathode interface region corresponding to the wavelength ~ 1000 nm increased for the TiO_2 layer inserted device compared to the pristine device. These findings originate from the reduction of the carrier recombination at the Si/cathode interface.

In addition, the electroluminescence image at the far-infrared region due to the dark current injection from the cathode interface for the corresponding device is compared shown in figure-2.5(c). The emission image is intense for the device with a TiO_2 HBL rather than that without inserting HBLs. These findings suggest that the band bending



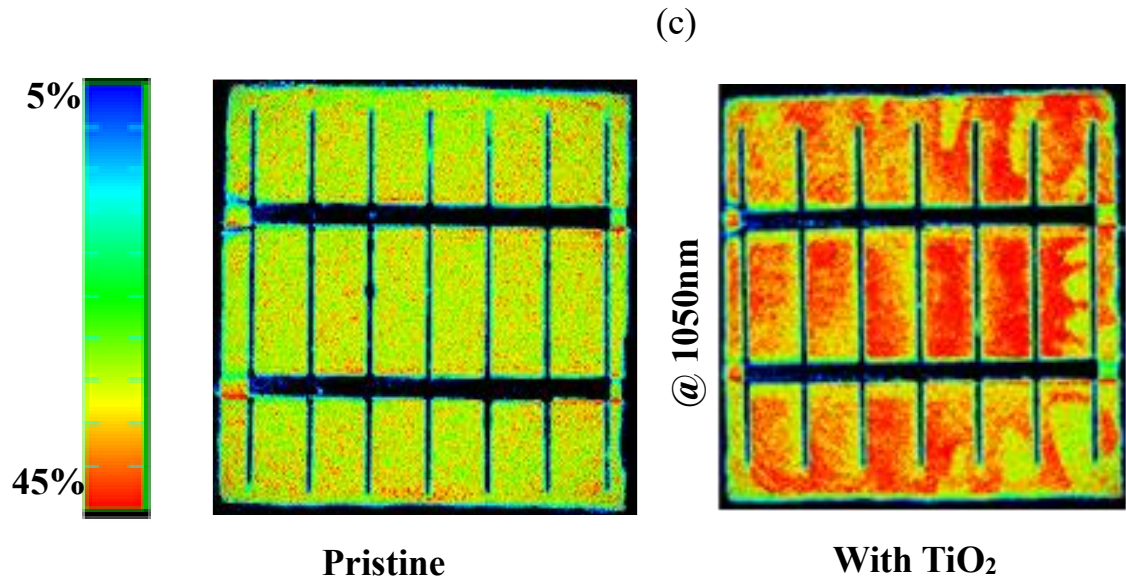


Figure-2.5: (a) J-V curve of PEDOT:PSS/n-Si solar cells with different layer thicknesses of TiO₂ as HBL. (b) the EQE for the devices with and without a 2-nm-thick TiO₂ HBLs. The inset shows the $\text{EQE}_{\text{TiO}_2}/\text{EQE}_{\text{pristine}}$ ratio. (c) The 2D map of the EQE at 1050 nm for pristine device with and without a 2-nm-thick TiO₂ HBL.

Table 2.1: Summary of PV performance for the PEDOT:PSS/n-Si solar cells with various thicknesses of TiO₂ HBL.

Device type		J_{sc} (mA/cm ²)	V_{oc} (mV)	FF (%)	PCE (%)
Pristine		27.5	605	68.0	11.23
TiO ₂	1 nm	29.0	613	73.1	13.01
	2 nm	30.0	616	70.9	13.08
	3 nm	28.5	612	65.8	11.46

2.4.2 Junction property at the Si/TiO₂ cathode interface monitored by the T_{rr} characterization

Figure- 2.6(a) shows the normalized EQE for both single and double layers of TiO₂ layer inserted device compared with the pristine device. Here, layer thickness for both layers is ~2nm. Corresponding device structures are inserted inside the figure. From the figure, it is shown that in case of a double-layer implanted device, photocurrent is more enhanced compared with a single-layer coated device. This improvement originates from the improved surface passivation provided by complete separation of the metal from Si surface. Additionally, more high carrier collection efficiency at the Si/cathode interface is also confirmed from this figure.

Figure 2.6 (b) shows the T_{rr} study of PEDOT:PSS/n-Si heterojunction solar cells with the 2-nm-thick single- and double-layer TiO₂. The hole storage time is ~2 and 2.8 times longer for single- and double-layer devices, respectively, compared to the pristine device without a TiO₂ layer. The amount of stored charge calculated by multiplying the corresponding recovery time (t_s) with maximum transient reverse current. Using equation 2.5, the surface recombination velocity (S) of ~750 cm/s is determined for the single-layer TiO₂ inserted device, in which 15.5% back area of the Si surface has direct contact with metal (Ag). This value has a good agreement with the S value measured by conventional μ -PCD. On the other hand, S value of ~375 cm/s was obtained for the device with alternate coating of TiO₂ layer. To understand the reliability of this value obtained by the T_{rr}, the μ -PCD measurement was performed using PEDOT:PSS or TiO₂ coated n-Si samples at both front and rear sides of c-Si substrate. The S of ~700 cm/s and ~60 cm/s are obtained for both sides of TiO₂ (2 nm) and PEDOT:PSS (80 nm) coated n-Si (1~5 Ω -cm) substrate respectively, which suggest that the cathode interface almost determines the photovoltaic performance.

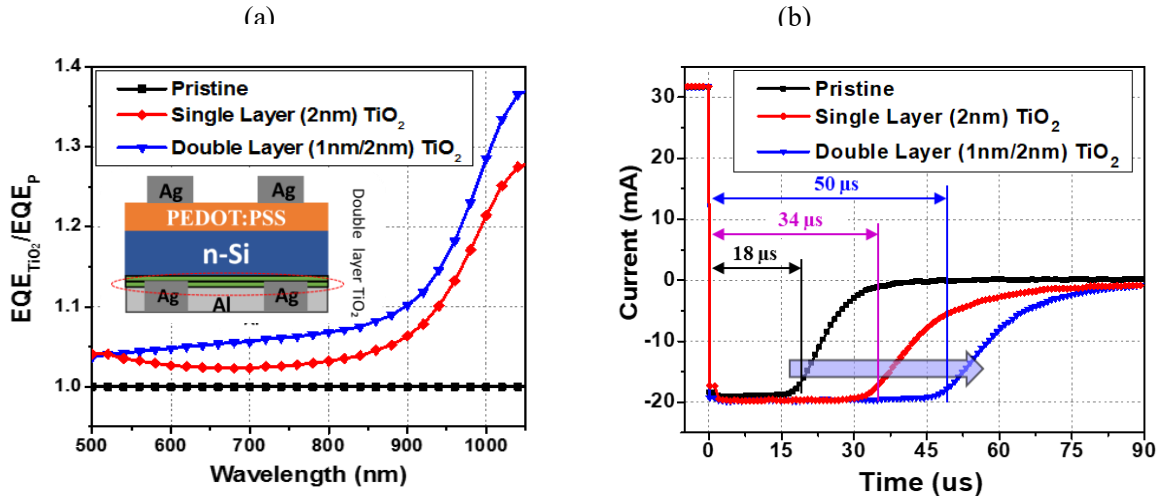


Figure 2.6: (a) Normalized EQE, $EQE_{TiO_2}/EQE_{pristine}$ and (b) Trr current profiles of the PEDOT:PSS/n-Si heterojunction solar cells with single- and double-layer of 2-nm-thick TiO_2 as HBL including the recovery time for each devices.

2.3 Summary and conclusions

The junction property at the solution-processed TiO_2 /n-Si interface was studied using the PEDOT:PSS/n-Si heterojunction solar cells. A PCE of 13.08% was obtained for the PEDOT:PSS/n-Si/ TiO_2 double heterojunction solar cells by adjusting the TiO_2 layer thickness at the n-Si/Ag interface with increased J_{sc} and V_{oc} . These findings originate from the efficient carrier collection at the n-Si/cathode interface, although the surface recombination at the cathode interface dominate the photovoltaic performance. The Trr provides the S value using the solar cell device structures with no needs of both sides TiO_2 coated c-Si.

Bibliography

1. J. Zhao, "Recent advances of high-efficiency single crystalline silicon solar cells in processing technologies and substrate materials", *Sol. Energy Mater. Sol. Cells* **82**, 53 (2004).
2. E.C. Douglas and R. V. D'Aiello, "A study of the factors which control the efficiency of ion-implanted silicon solar cells *IEEE Trans. Electron Devices* **27**, 792 (1980).
3. K. Masuko, M. Shigematsu, T. Hashiguchi, D. Fujishima, M. Kai, N. Yoshimura, T. Yamaguchi, Y. Ichihashi, T. Mishima, N. Matsubara, T. Yamanishi, T. Takahama, M. Taguchi, E. Maruyama, and S. Okamoto, " Achievement of More Than 25% Conversion Efficiency With Crystalline Silicon Heterojunction Solar Cell", *IEEE J. Photovoltaics* **4**, 1433 (2014).
4. J. Schmidt and K. Bothe, " Structure and transformation of the metastable boron- and oxygen-related defect center in crystalline silicon", *Phys. Rev. B* **69**, 024107 (2004).
5. T. Sameshima, K. Kogure, and M. Hasumi, " Crystalline Silicon Solar Cells with Two Different Metals", *Jpn. J. Appl. Phys.* **49**, (2010).
6. T.G. Allen, J. Bullock, Q. Jeangros, C. Samundsett, Y. Wan, J. Cui, A. Hessler-Wyser, S. De Wolf, A. Javey, and A. Cuevas, "A Low Resistance Calcium/Reduced Titania Passivated Contact for High Efficiency Crystalline Silicon Solar Cells" *Adv. Energy Mater.* **7**, 1602606 (2017).
7. Y. Wan, C. Samundsett, D. Yan, T. Allen, J. Peng, J. Cui, X. Zhang, J. Bullock, and A. Cuevas, " A magnesium/amorphous silicon passivating contact for n-type crystalline silicon solar cells", *Appl. Phys. Lett.* **109**, 113901 (2016).

8. M. Akiya and H. Nakamura, " Low ohmic contact to silicon with a magnesium/aluminum layered metallization", J. Appl. Phys. **59**, 1596 (1986).
9. P.L. Janega, J. McCaffrey, D. Landheer, M. Buchanan, M. Denhoff, and D. Mitchel, "Contact resistivity of some magnesium/silicon and magnesium silicide/silicon structures", Appl. Phys. Lett. **53**, 2056 (1988).
10. J. Kanicki, "Contact resistance to undoped and phosphorus-doped hydrogenated amorphous silicon films", Appl. Phys. Lett. **53**, 1943 (1988).
11. T.G. Allen, J. Bullock, P. Zheng, B. Vaughan, M. Barr, Y. Wan, C. Samundsett, D. Walter, A. Javey, and A. Cuevas, " Calcium contacts to n-type crystalline silicon solar cells", Prog. Photovoltaics Res. Appl. **25**, 636 (2017).
12. A.Y.C. Yu and C.A. Mead, " Characteristics of aluminum-silicon schottky barrier diode" Solid. State. Electron. **13**, 97 (1970).
13. H.C. Card, "Aluminum-Silicon Schottky barriers and ohmic contacts in integrated circuits", IEEE Trans. Electron Devices **23**, 538 (1976).
14. A.M. Cowley and S.M. Sze, "Surface States and Barrier Height of Metal-Semiconductor Systems", J. Appl. Phys. **36**, 3212 (1965).
15. J. Tersoff, "Schottky Barrier Heights and the Continuum of Gap States" Phys. Rev. Lett. **52**, 465 (1984).
16. S.M. Sze and K.K. Ng, *Physics of Semiconductor Devices*, 3rd ed. (John Wiley & Sons, Inc., Hoboken, 2006).
17. Y. Wan, C. Samundsett, J. Bullock, M. Hettick, T. Allen, D. Yan, J. Peng, Y. Wu, J. Cui, A. Javey, and A. Cuevas, "Conductive and Stable Magnesium Oxide Electron - Selective Contacts for Efficient Silicon Solar Cells", Adv. Energy Mater. **7**, 1601863 (2017).
18. X. Yang, P. Zheng, Q. Bi, and K. Weber, "Silicon heterojunction solar cells with

- electron selective TiO_x contact", *Sol. Energy Mater. Sol. Cells* **150**, 32 (2016).
19. K.A. Nagamatsu, S. Avasthi, G. Sahasrabudhe, G. Man, J. Jhaveri, A.H. Berg, J. Schwartz, A. Kahn, S. Wagner, and J.C. Sturm, "Titanium dioxide/silicon hole-blocking selective contact to enable double heterojunction crystalline silicon-based solar cell", *Appl. Phys. Lett.* **106**, 123906 (2015).
 20. S. Avasthi, W.E. McClain, G. Man, A. Kahn, J. Schwartz, and J.C. Sturm, "Hole-blocking titanium-oxide/silicon heterojunction and its application to photovoltaics", *Appl. Phys. Lett.* **102**, 203901 (2013).
 21. J. He, Z. Ling, P. Gao, and J. Ye, " TiO_2 Films from the Low-Temperature Oxidation of Ti as Passivating-Contact Layers for Si Heterojunction Solar Cells", *Sol. RRL* **1**, 1700154 (2017).
 22. J. Jhaveri, K.A. Nagamatsu, A.H. Berg, G. Man, G. Sahasrabudhe, S. Wagner, J. Schwartz, A. Kahn, and J.C. Sturm, "Double-Heterojunction Crystalline Silicon Solar Cell with Electron Selective TiO_2 Cathode Contact Fabricated at 100°C with Open-Circuit Voltage of 640 mV 2015", *IEEE 42nd Photovoltaic. Spec. Conf. PVSC* **2**, 1 (2015).
 23. P.J. Cameron and L.M. Peter, "Characterization of Titanium Dioxide Blocking Layers in Dye-Sensitized Nanocrystalline Solar Cells", *J. Phys. Chem. B* **107**, 14394 (2003).
 24. A. Manor, E.A. Katz, T. Tromholt, and F.C. Krebs, "Enhancing functionality of ZnO hole blocking layer in organic photovoltaics", *Sol. Energy Mater. Sol. Cells* **98**, 491 (2012).
 25. J. Hossain, K. Kasahara, D. Harada, A.T.M. Saiful Islam, R. Ishikawa, K. Ueno, T. Hanajiri, Y. Nakajima, Y. Fujii, M. Tokuda, and H. Shirai, " Barium hydroxide hole blocking layer for front-and back-organic/crystalline Si heterojunction solar

- cells", *J. Appl. Phys.* **122**, 55101 (2017).
26. A.T.M.S. Islam, M.E. Karim, A. Rajib, Y. Nasuno, T. Ukai, S. Kurosu, M. Tokuda, Y. Fujii, Y. Nakajima, T. Hanajiri, and H. Shirai, "Chemical mist deposition of organic for efficient front-and back-PEDOT: PSS/crystalline Si heterojunction solar cells", *Appl. Phys. Lett.* **114**, 193901 (2019).
 27. Y. Zhang, W. Cui, Y. Zhu, F. Zu, L. Liao, S.T. Lee, and B. Sun, "High efficiency hybrid PEDOT: PSS/nanostructured silicon Schottky junction solar cells by doping-free rear contact", *Energy Environ. Sci.* **8**, 297 (2015).
 28. W. Wu, J. Bao, X. Jia, D. Liu, L. Cai, B. Liu, J. Song, and H. Shen, "Pseudocapacitive Na-ion storage boosts high rate and areal capacity of self-branched 2D layered metal chalcogenide nanoarrays", *Phys. Status Solidi-Rapid Res. Lett.* **10**, 662 (2016).
 29. S. Kim, J. Lee, V.A. Dao, S. Lee, N. Balaji, S. Ahn, S.Q. Hussain, S. Han, J. Jung, J. Jang, Y. Lee, and J. Yi, "Effects of LiF/Al back electrode on the amorphous/crystalline silicon heterojunction solar cells", *Mater. Sci. Eng. B* **178**, 660 (2013).
 30. Y. Zhang, R. Liu, S.-T. Lee, and B. Sun, "The role of a LiF layer on the performance of poly(3,4-ethylenedioxythiophene):poly(styrenesulfonate)/Si organic-inorganic hybrid solar cells", *Appl. Phys. Lett.* **104**, 83514 (2014).
 31. J. Bullock, M. Hettick, J. Geissbühler, A.J. Ong, T. Allen, C.M. Sutter-Fella, T. Chen, H. Ota, E.W. Schaler, S. De Wolf, C. Ballif, A. Cuevas, and A. Javey, "Efficient silicon solar cells with dopant-free asymmetric heterocontacts", *Nat. Energy* **1**, 15031 (2016).

Chapter 3

Experimental Procedure and Characterization Method

3.1 Experimental Procedure

3.1.1 Fabrication process of PEDOT:PSS/n-Si heterojunction solar cell

As a base substrate, a both-side-polished $2 \times 2 \text{ cm}^2$ size n-type (100) CZ c-Si wafers ($1\text{--}5 \text{ }\Omega \cdot \text{cm}$) with a thickness of $250 \text{ }\mu\text{m}$ was used. Before the film deposition, the n-Si substrates were ultrasonically cleaned with acetone, isopropanol, and DI-water for 10 min each, followed by 5 wt% HF_{aq} treatment for 3 min to remove the native oxide. At first step, a solution of PEDOT:PSS (prepared from Clevios^R PH1000 by adding ethylene-glycol and capstone fluorosurfactant in the ratio of 93:7:0.16 wt.% respectively) was spin-coated (SC) on top of the cleaned n-Si substrate. After then, the solution coated sample is followed by thermal annealing at $140 \text{ }^\circ\text{C}$ for 30 min to remove the residual solvent. Ag grid electrodes were formed on the front and rear sides using a screen printer (Newlong Seimitsu Co., Ltd. DP-320) followed by thermal annealing at $170 \text{ }^\circ\text{C}$ for 30 min. Finally, the Al was evaporated in the entire area of the rear side as the cathode electrode. Figure-3.1 shows the details device fabrication process of PEDOT:PSS/n-Si heterojunction solar cell.

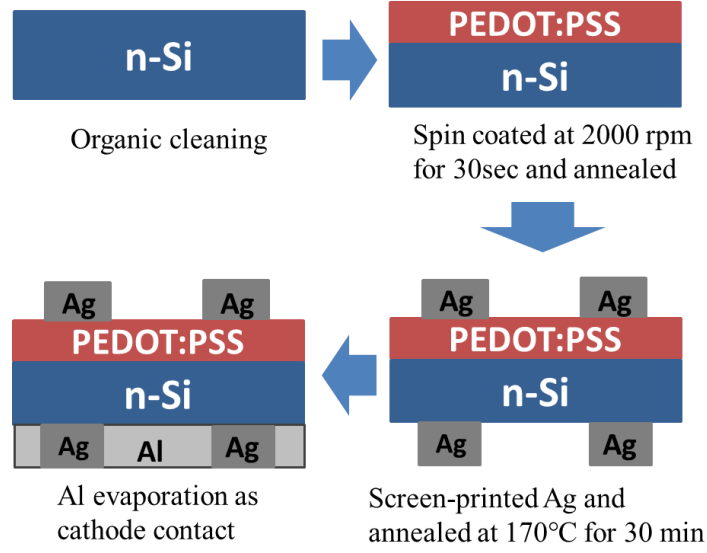
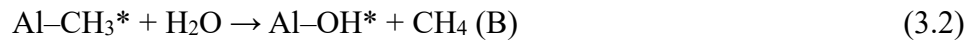


Figure-3.1: Fabrication process of PEDOT:PSS/n-Si heterojunction solar cell

3.1.2 Deposition of AlO_x on c-Si by Atomic Layer Deposition (ALD)

3.1.2.1 Principle of AlO_x deposition by ALD

Many promising applications result from combining the advantages of the ALD growth process with the excellent material properties of Al_2O_3 . Consequently, ALD- Al_2O_3 growth has been studied extensively over the past few years. Al_2O_3 growth by ALD has been based on the CVD reaction: $2\text{Al}(\text{CH}_3)_3 + 3\text{H}_2\text{O} \rightarrow \text{Al}_2\text{O}_3 + 6\text{CH}_4$. To implement ALD- Al_2O_3 , this CVD reaction is split into two half-reactions [1,2-5]:



Where the asterisks denote the surface species, alternate precursors such as $\text{Al}(\text{CH}_3)_2\text{Cl}$, AlCl_3 , and H_2O_2 have also been employed for ALD- Al_2O_3 [6-9].

During ALD- Al_2O_3 growth, trimethylaluminum (TMA) is introduced and

allowed to react with hydroxyl groups on the surface. This reaction proceeds until the surface reaction reaches completion [3]. Subsequently, TMA is carried or pumped away. The same process is then performed with H_2O . The H_2O reacts with methyl groups on the surface until this surface reaction reaches completion. The sequential exposure to TMA and H_2O constitutes one A.B. cycle [3]. These AB cycles are repeated to achieve the desired film thickness. Figure-3.2 shows the basic principle of the ALD- Al_2O_3 procedure.

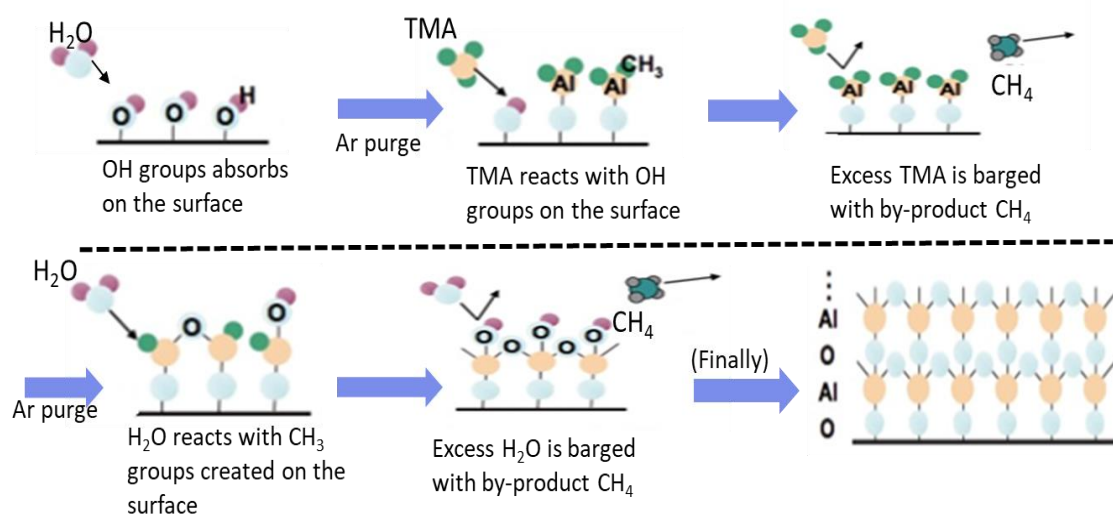


Figure-3.2: Basic principle of Al_2O_3 deposition by Atomic Layer Deposition (ALD)

3.1.2.2. Sample preparation

Here, both sides polished $2 \times 2 \text{ cm}^2$ size n-type (100) C.Z. c-Si wafers ($1\text{-}5 \Omega\text{-cm}$) with a thickness of $250 \mu\text{m}$ was used as a substrate. Before the ALD- AlO_x film deposition, the n-Si substrate was cleaned by the standard Radio Corporation of America (RCA) cleaning to remove the ionic and organic impurities. The RCA cleaning was done in two steps. First, the samples were immersed in RCA1 solution of DI-water, 37% ammonium hydroxide (NH_4OH), and 30% hydrogen peroxide (H_2O_2) in the weight ratio of 5:1:1 for 15 min, followed by rinsing in DI-water. Secondly, the cleaned samples were immersed

in RCA2 solution of DI-water, 37% hydrochloric acid (HCl), and 30% H₂O₂ in the weight ratio of 6:1:1 for 10 min, followed by rinsing in DI-water. Then, the native oxide was removed by hydrofluoric acid treatment and blow-dried with N₂. In the next stage, the amorphous aluminum oxide (AlO_x) was deposited by Atomic Layer Deposition.

3.1.2.3 AlO_x film deposition by ALD

Figure-3.3 shows the schematic diagram of an ALD system. The ALD- AlO_x films were grown using the H₂O and Al(CH₃)₃ (TMA) precursors. The carrier gas was Ar gas, which was controlled at a rate of 5 sccm by an Ar gas mass flow controller (MFC).

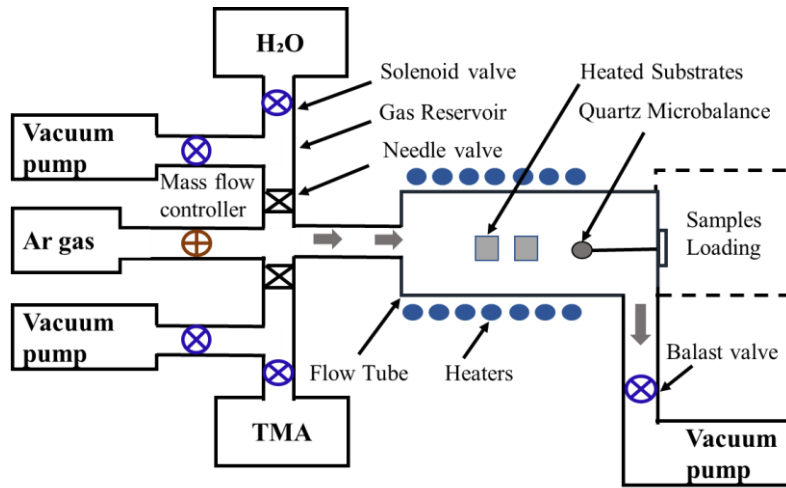


Figure-3.3: Schematic diagram of the ALD system

Alternative supply of TMA and H₂O to the cleaned n-Si substrate by adjusting the supply period of TMA and water. The residual gas and excess carriers of TMA and H₂O was removed by purging the Ar gas flow. The gas switching valves allow for a rapid turn on and shut off of the reactant gases for short ALD cycle times. This short time is facilitated by pumping the gas reservoirs with separate mechanical pumps after the

reactant exposures. Also, variable conductance needle valves are employed that control the reactant flux into the N₂ carrier gas and allow a ‘gas window’ to shut off the reactant quickly after the reactant exposure. The total time for one complete ALD- AlO_x cycle was typically 75 s where the supply time is 100ms for TMA, 40ms for H₂O, 40 ms for Ar gas. And 20s and 15s are for ballast time for TMA and H₂O, respectively. Figure-3.4 shows the gas supply period of the ALD system.

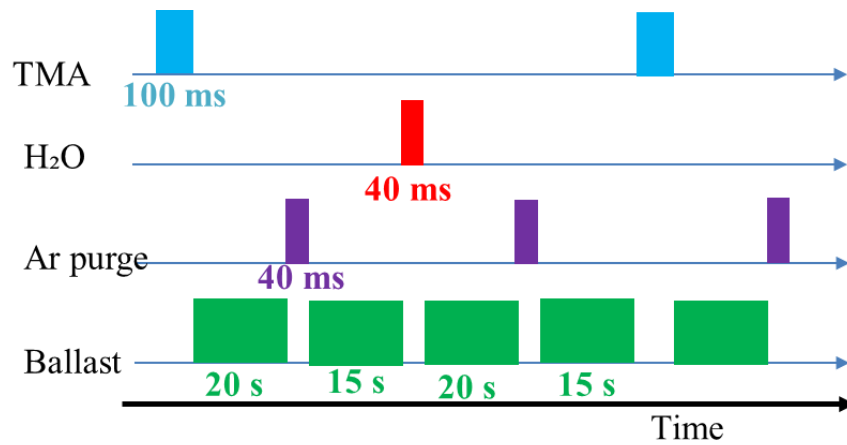


Figure-3.4: Gas supply of ALD system

Approximately 6 to 170 ALD- AlO_x cycles were grown and tested through this course of this study whose corresponding film thicknesses were about 1-30nm and the substrate temperature varying from 160 to 220°C.

3.1.3 Preparation of AlO_x island by UV photolithography process

3.1.3.1 Sample preparation

In this study, n-type (100) C.Z. c-Si wafers (1x1 cm², 1-5 Ω-cm) having both sides polished with a thickness of 250 μm was used as a substrate. First, the n-Si substrate was cleaned by RCA1 and RCA2 cleaning to remove the ionic and organic impurities. In

RCA1 cleaning, the samples were immersed into the solution of DI-water, 37% ammonium hydroxide (NH_4OH), and 30% hydrogen peroxide (H_2O_2) in the weight ratio of 5:1:1 for 15 min, followed by rinsing in DI-water. After then, the substrate was immersed in RCA2 solution of DI-water, 37% hydrochloric acid (HCl), and 30% H_2O_2 in the weight ratio of 6:1:1 for 10 min, followed by rinsing in DI-water. Then, the native oxide was removed by hydrofluoric acid treatment and blow-dried with N_2 . In the next stage, the amorphous aluminum oxide (AlO_x) was deposited by Atomic Layer Deposition 425°C for 15 min under vacuum condition.

3.1.3.2 Preparation of AlO_x island by UV photolithography process

In this study, we used the UV photolithography facility in Bio-Nano Electronics Research Centre (BNERC) at Toyo University. Before the photolithography process, a glass mask was used where different types of patterning can proceed. Figure-3.5 shows a pattern mask where $15\ \mu\text{m}$ squatted AlO_x islands were made with a different interval from $15\text{-}150\ \mu\text{m}$ distance.

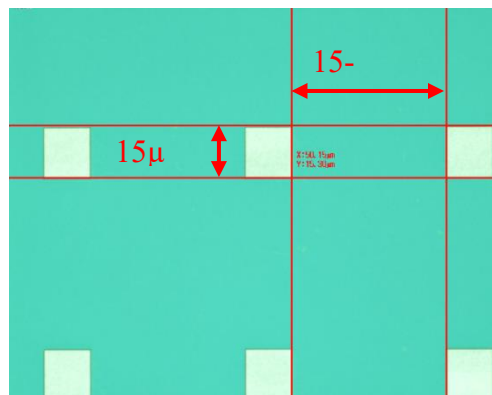


Figure-3.5: Pattern mask for $15\ \mu\text{m}$ squatted AlO_x islands with a different interval from $15\text{-}150\ \mu\text{m}$ distance

Figure-3.6 shows the fabrication process of AlO_x island on the n-type c-Si

substrate by the UV photolithography method. After AlO_x deposition on the n-type c-Si substrate with annealing, first, the photoresist material was spin-coated on the sample at a speed of 500rpm for 5 min and then 3000rpm for 30 sec. Here, we used the OFPR-10CP solution as a photoresist material. After spin coating, the sample was pre-baked at a 110°C for 90 sec. Then the sample was exposed by UV light exposer for a short time (6 sec). After that, the sample was immediately developed through the NMD-3 solution. After development, the sample was rinsed by the DI-water and then post baked at 110°C for 2 min. This way, the patterning was created on the AlO_x .

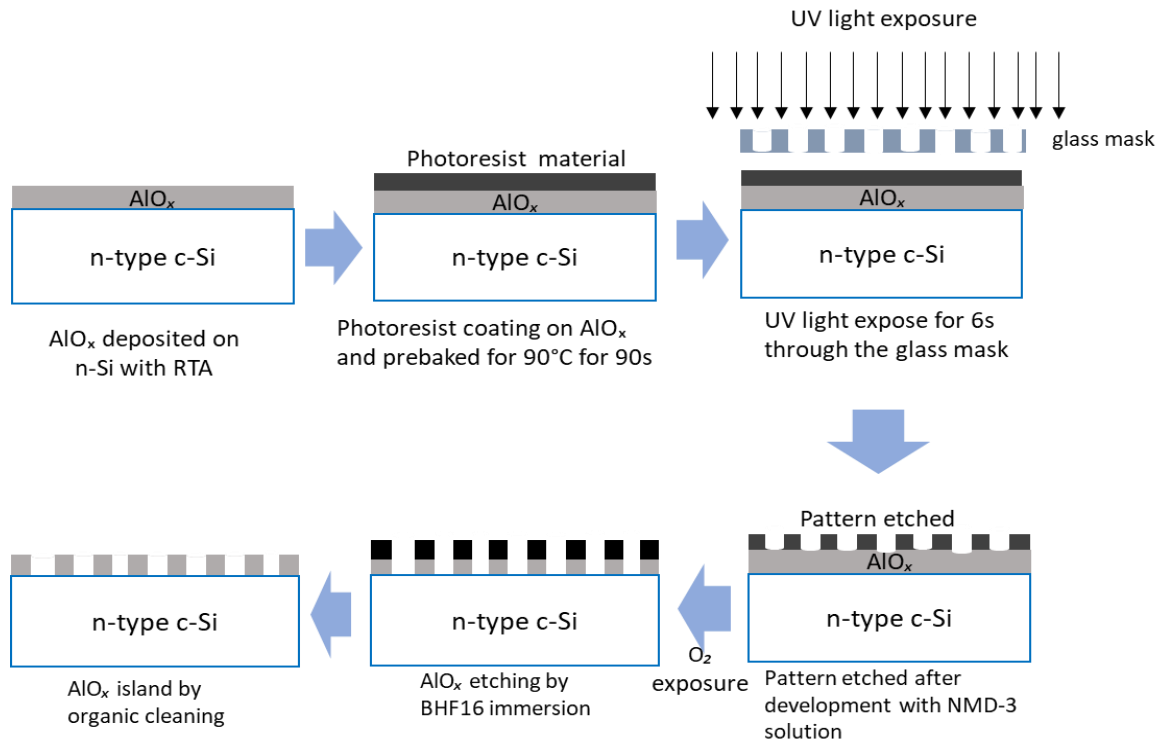


Figure-3.6: Fabrication process of AlO_x island on c-Si substrate using UV photolithography process.

After patterning, the sample was exposed through the O_2 plasma at 100W for 10 sec and then immersed the sample into the buffered hydrofluoric acid (BHF16) and then

rinsed by DI-water to make the AlO_x island. Finally, organic cleaning was used for removing the photoresist coating. In this way, we prepared the AlO_x island for different area ratios. Figure-3.7(a-b) shows the microscopic image and thickness profile of AlO_x island on n-Si substrate where 15 μm squatted AlO_x islands were designed with different space distance of 50-150 μm . Also, the thickness profile confirms the AlO_x island on n-Si substrate. Table-3.1 shows the area ratio of AlO_x island to PEDOT:PSS.

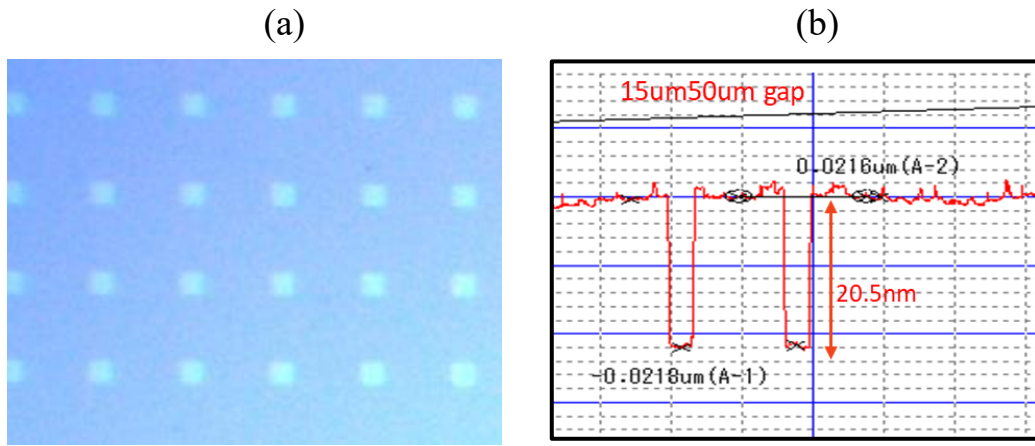


Figure-3.7: (a) Microscopic image of AlO_x island on n-Si substrate and (b) thickness profile of AlO_x island

Table-3.1: Area ratio of AlO_x island with a PEDOT:PSS overlayer

Area (μm)	Area distance (μm)	Area ratio of AlO_x island /PEDOT:PSS
15	15	1/1
	50	3.3/1
	100	6.7/1
	150	10/1

3.1.3.3 Device fabrication PEDOT:PSS/n-Si heterojunction solar cells with AlO_x island

Figure-3.8(a) shows the device fabrication of PEDOT:PSS/n-Si solar cell with AlO_x island. Here, the PEDOT:PSS was spin-coated on the AlO_x island/n-Si substrate at a 3000rpm speed for 30 sec and then annealed for 140°C for 30 min. Later, Ag was coated as an anode electrode, and InGa coated as a cathode electrode. The PEDOT:PSS coated on AlO_x island is confirmed by the cross-sectional S.E.M. image shown at the figure-3.8(b).

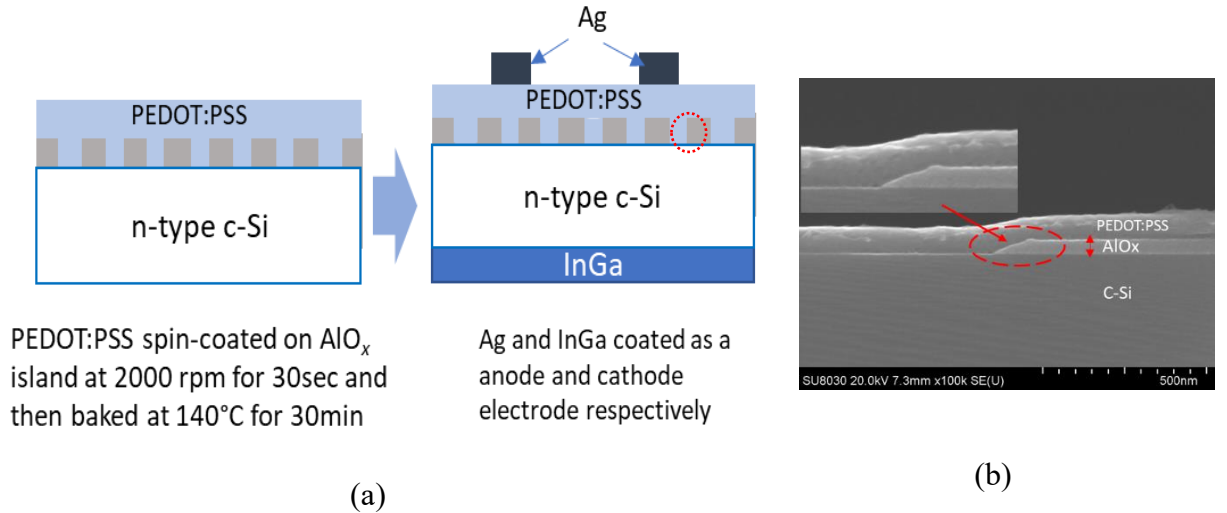


Figure-3.8: (a) Device fabrication of PEDOT:PSS/n-Si solar cell with AlO_x island, (b) Cross-sectional image of AlO_x island/PEDOT:PSS on n-Si substrate.

The interface of PEDOT:PSS/n-Si solar cells with AlO_x island at different area ratio were examined by the C-V, J-V, and EQE characteristics. The C-V measurements of the samples were carried out at 100 kHz by Hisol 2700-LCR embedded with Keithley 4200 system, J-V, and EQE by the solar simulator of model CEP-25BX designed by Bunkoukeiki, embedded with 1.5AM ($100\text{ mW}/\text{cm}^2$) light source.

3.1.4 Fabrication process PEDOT:PSS/n-Si heterojunction solar cell with ultrathin $\text{AlO}_x/\text{ch-SiO}_x$ (1~3 nm)

3.1.4.1 Fabrication process of ch-SiO_x at the $\text{AlO}_x/\text{n-Si}$ interface

After the RCA1 and RCA2 cleaning with HF treatment, the n-type Czochralski n-Si (100) wafers ($1\text{--}5\ \Omega\cdot\text{cm}$) samples were immersed in hydrofluoric acid (HF) for 15 s. After that, ultrathin ch-SiO_x tunnel layers were fabricated on the n-Si wafers in a 4 wt.% H_2O_2 solution at temperatures of 25 °C and 80 °C for 10 min, for thicknesses of 1.39 nm and approximately 3 nm, respectively. After then, 6 cycles of ultrathin AlO_x was deposited on the ch-SiO_x coated samples. Then, the samples were subjected to FGA at 560 °C for 30 min and RTA at 425°C for 15min. Figure-3.9 shows the fabrication process of ch-SiO_x at the $\text{AlO}_x/\text{n-Si}$ interface.

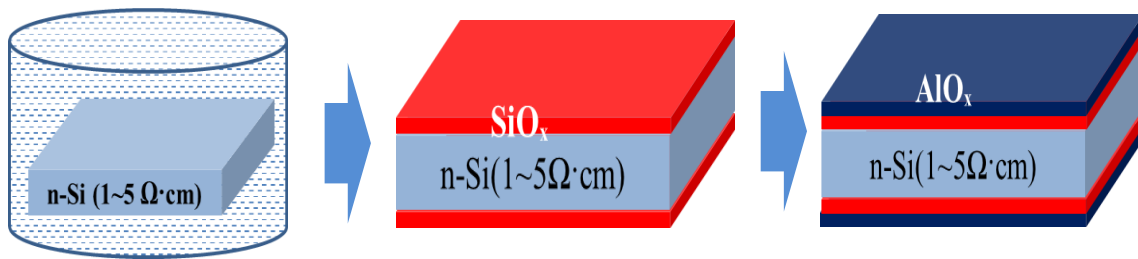


Figure-3.9: Fabrication process of ch-SiO_x at the $\text{AlO}_x/\text{n-Si}$ interface

3.1.4.2 Fabrication process PEDOT:PSS/n-Si heterojunction solar cells with $\text{AlO}_x/\text{ch-SiO}_x$ stack layer

For front-PEDOT:PSS/n-Si heterojunction solar cell devices, PEDOT:PSS with 7 wt.% ethylene glycol was spin-coated at 2000 rpm for 20s on cleaned n-Si substrates

with solely ALD- AlO_x and $\text{AlO}_x/\text{ch-SiO}_x$ stack layers with and without RTA and FGA, followed by thermal annealing at 140 °C for 30 min to remove residual solvent. Then, Ag grid electrodes were formed on the front and rear sides using a screen printer (Newlong Seimitsu Co., Ltd. DP-320) followed by thermal annealing at 170 °C for 30 min. Finally, aluminum was evaporated from the entire area of the rear side to create the cathode contact. Figure-3.10 shows the schematic device diagram of PEDOT:PSS/n-Si heterojunction solar cell with ultrathin $\text{AlO}_x/\text{ch-SiO}_x$ stack layer.

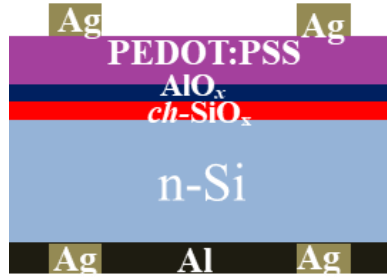


Figure-3.10: Schematic device diagram of PEDOT:PSS/n-Si heterojunction with ultrathin $\text{AlO}_x/\text{ch-SiO}_x$ stack layer

The current density-voltage (J-V) characteristics were measured in the dark and during exposure to simulated solar light of AM1.5G, 100 mW/cm² (Bunkoukeiki Co., Ltd., CEP-25BX). The light exposure area was masked using a shadow mask to prevent light leakage. The 2D maps of the solar cell parameters were obtained for devices with a 2×2 cm² area using a system to measure the distribution of the solar cell conversion efficiency (Lasertec, MP Series).

3.2 Characterization method

3.2.1 Micro-photoconductive decay (μ -PCD)

Figure-3.11 shows the principle of the μ -photoconductive decay (μ -PCD) measurement method. In this method, we monitor the decay of the excess photogenerated carrier by a pulse laser irradiation at 904 nm as the time evolution of microwave reflectance through the following equation.

$$\Delta n = \Delta n_0 \exp(-t/\tau) \quad (3.3)$$

Where n_0 is the excess carrier concentration at time $t=0$, and t is the effective lifetime of the excess carrier. The measurement has been performed using a c-Si sample, where a dielectric layer symmetrically passivated both front and rear surfaces.

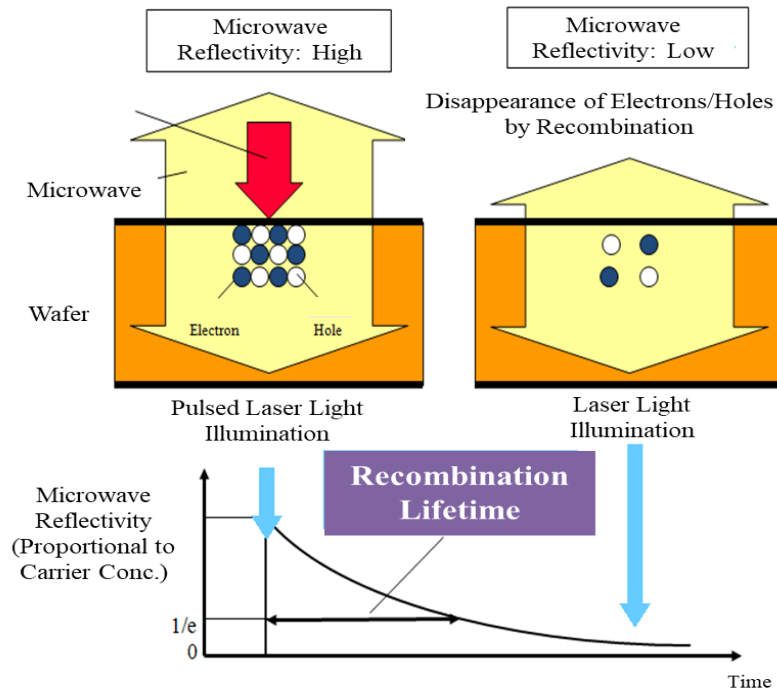


Figure-3.11: Principle of micro-photoconductive decay (μ -PCD) method

3.2.2 Forming gas annealing (FGA) and Rapid thermal annealing (RTA) method

Figure-3.12 shows the schematic diagram of forming gas annealing and rapid thermal annealing process. In the case of FGA, the samples were annealed at 560°C for 30 min under N₂/H₂ (95/5) % gas mixture condition. On the other hand, in Rapid thermal annealing, the samples were annealed at 425°C for 15min under vacuum condition.

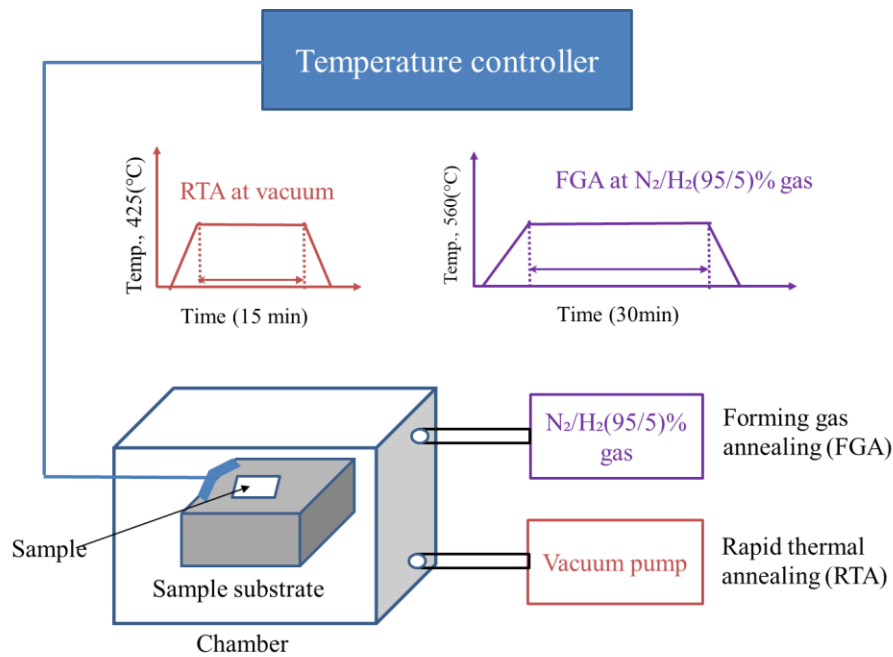


Figure-3.12: Schematic diagram of Forming gas annealing (FGA) and Rapid thermal annealing (RTA)

3.2.3 Atomic Force Microscopy (AFM)

Atomic force microscopy (AFM) is a very-high-resolution type of scanning probe microscopy (SPM), with demonstrated resolution on the order of fractions of a nanometer, more than 1000 times better than the optical diffraction limit. An AFM generates images by scanning a small cantilever over the surface of a sample. The sharp

tip on the end of the cantilever contacts the surface, bending the cantilever and changing the amount of laser light reflected into the photodiode. The height of the cantilever is then adjusted to restore the response signal resulting in the measured cantilever height tracing the surface. In this study, AFM5000II, Hitachi High-Tech Science system had been used to characterize the deposited films to understand the film's surface roughness. Figure-3.13 shows the principle of the AFM system.

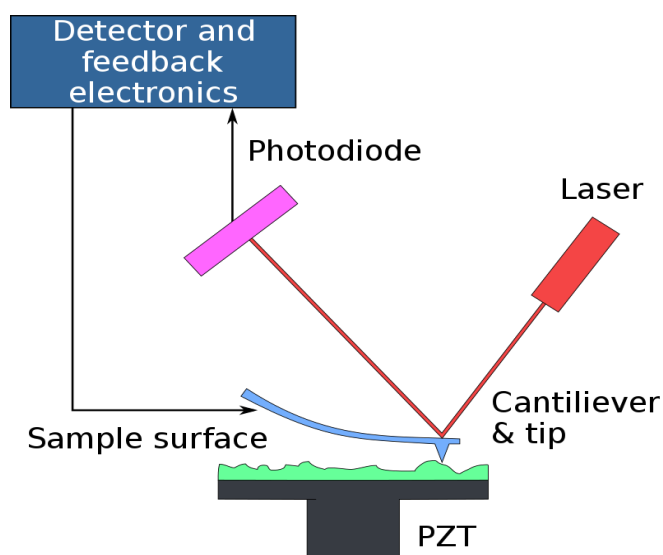


Figure-3.13: Schematic diagram of an AFM system.

3.2.4 Fourier-transform infrared spectroscopy (FTIR)

Fourier-transform infrared spectroscopy (FTIR) is a technique used to obtain an infrared spectrum of absorption or emission of a solid, liquid, or gas. An FTIR spectrometer simultaneously collects high-spectral-resolution data over a wide spectral range. This confers a significant advantage over a dispersive spectrometer, which measures intensity over a narrow range of wavelengths at a time. Figure-3.14 shows a schematic diagram of an FTIR set up with a beam splitter and compensator plate.

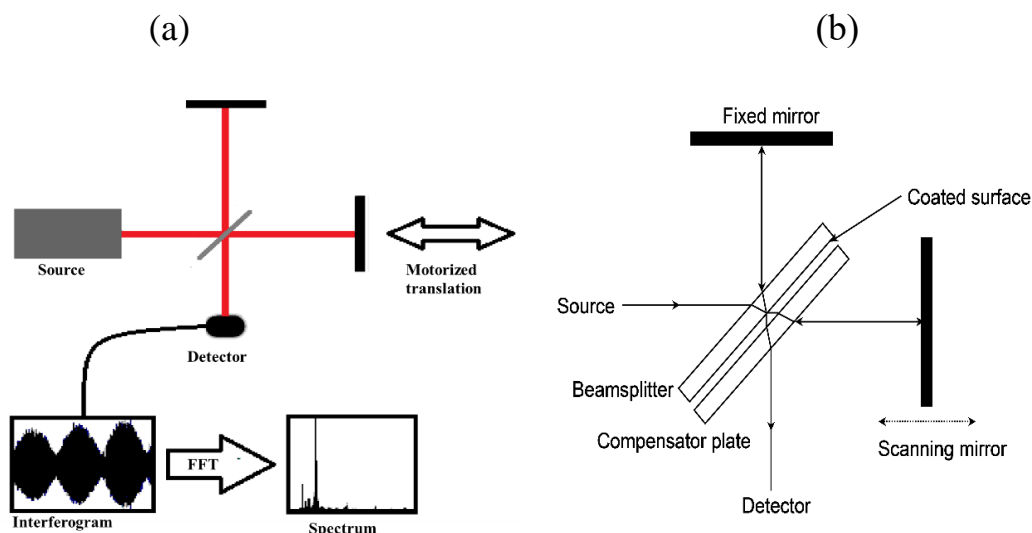


Figure- 3.14: (a) Schematic diagram of an FTIR set up, (b) Simple interferometer with a beam-splitter and compensator plate.

In this study, we have used the Shimadzu corporation (ITTracer-100 model) FTIR system. This system achieves excellent sensitivity with an SN ratio of 60,000:1, high resolution at 0.25 cm^{-1} , and high-speed scanning capable of 20 spectra/second. The performance of medium and higher-end models is supported by high reliability, including advanced dynamic alignment and an interferometer with a dehumidifier. This is compatible with applications active in a variety of circumstances, with a library of approximately 12,000 spectra and data analysis programs for contaminant analysis, and time course and rapid scan programs for reaction tracking. Figure-3.15 shows the FTIR spectroscopy (Shimadzu, ITTracer-100 system) system.



Figure- 3.15: FTIR spectroscopy (Shimadzu, ITTracer-100 system)

3.2.5 Capacitance-Voltage (C-V) Profiling

Capacitance-voltage (C-V) profiling is a technique for characterizing semiconductor materials and devices. The applied voltage is varied, and the capacitance is measured and plotted as a function of voltage. The technique uses a metal-semiconductor junction (Schottky barrier) or a p-n junction or MOSFET to create a depletion region. However, C-V measurements are widely used to characterize the semiconductor parameters like MOS device, photovoltaic cells, TFT device, and so on. In this study, the electrical properties (like built-in potential, interface trap density, negative fixed charged density, and others) are characterized by the C-V measurements of the corresponding samples were carried out at 100 kHz by Hisol 2700-LCR embedded with Keithley 4200 system. Figure-3.16 shows (a) the schematic diagram of the MIS device, and (b) modeled ideal C-V curve (no interface state, $V_{fb}=0V$) of a silicon MIS capacitor at low and high frequencies.

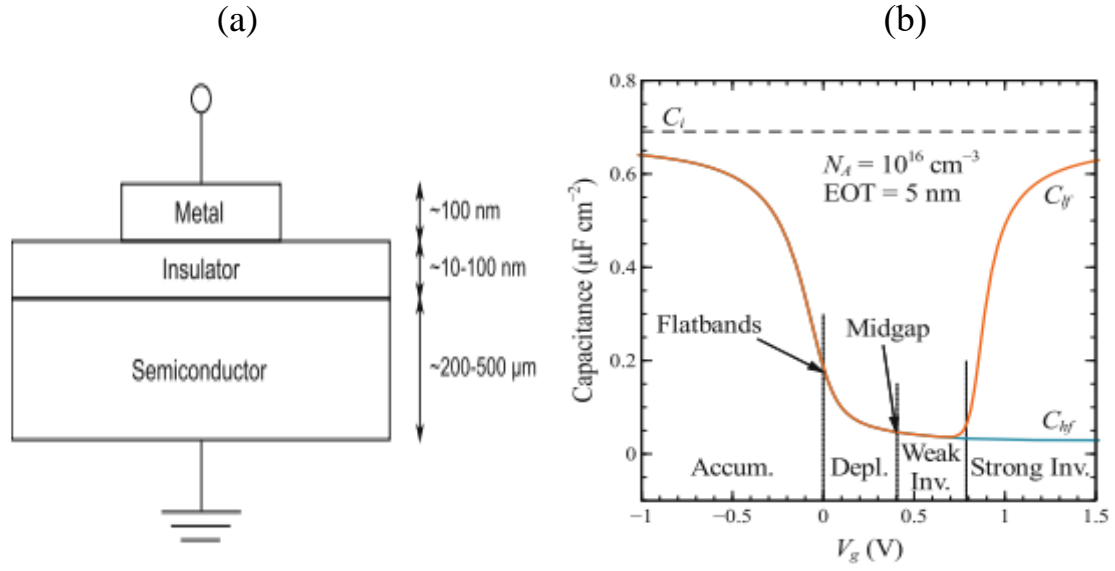


Figure-3.16: (a) Schematic of an MIS structure used in C-V measurement, (b) Modelled ideal C-V curve (no interface state, $V_{fb} = 0\text{V}$) of a silicon MIS capacitor at low and high frequencies. The voltage ranges corresponding to accumulation, depletion, weak inversion, and strong inversion are indicated.

3.2.6 X-ray electron spectroscopy (XPS) method

Figure-3.17 shows the principle of XPS for the ultrathin thick SiO_2 on Si substrate. In XPS, when an x-ray of known energy ($h\nu$) is applied to a molecule, then an electron is knocked out from the electron orbit in the molecule with a kinetic energy E_k . Then the binding energy, E_b is defined by the relations

$$E_k = h\nu - E_b - \phi \quad (3.4)$$

Where binding energy for the different chemical bond of the measured samples is shown by survey spectra, in this study, AXIS Nova (Kratos Analytical) equipped with a monochromatic X-ray source (Al Kα) was used a 1 mm square sputtering was performed

with a 5 keV argon gas cluster (Ar2000 +) using a 110- μm slit measurement. Based on this principle, an XPS scan spectrum for $\sim 5\text{\AA}$ SiO_2 on Si substrate is shown in figure-3.17 (b). The deconvolution of Si 2P core level for $\sim 5\text{\AA}$ thick SiO_2 on Si substrate and the possible Si suboxide peaks.

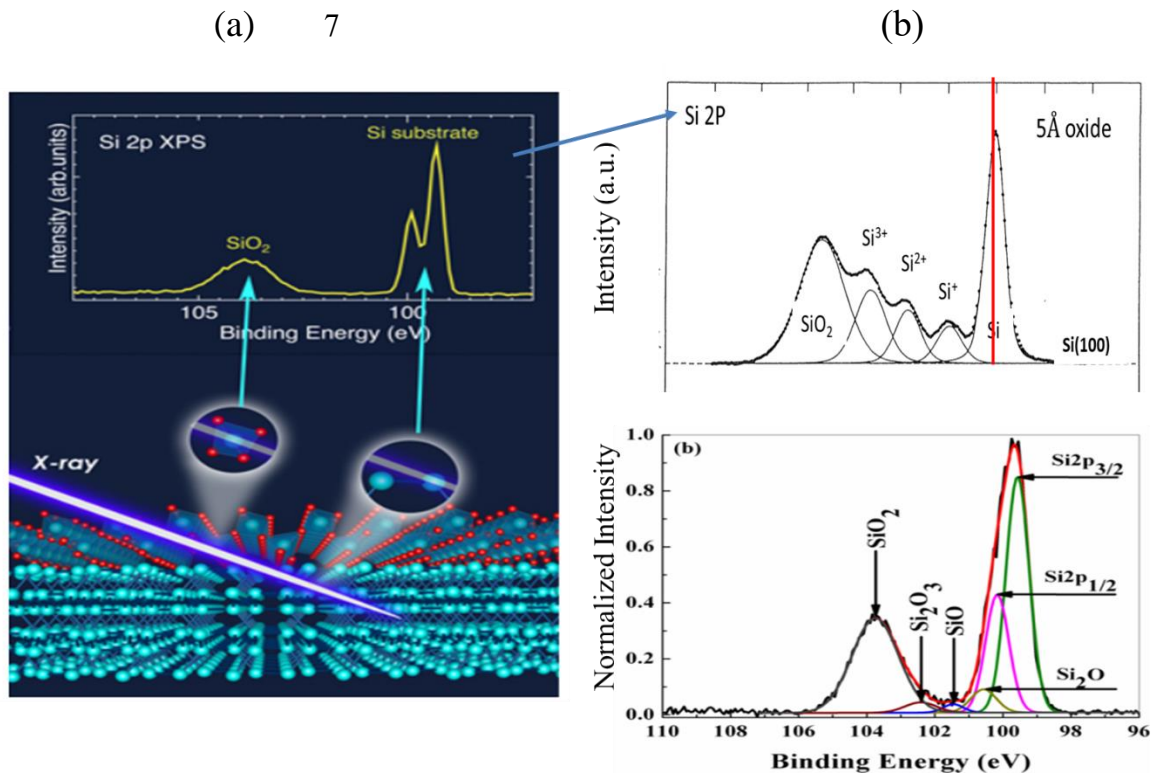


Figure-3.17: (a) principle of XPS with scan spectra for the ultrathin thick SiO_2 on Si substrate, (b) deconvolution of Si 2P core level for $\sim 5\text{\AA}$ thick SiO_2 on Si substrate and the possible Si suboxide peaks

3.2.7 Photoemission Yield Spectroscopy in Air (PYSA)

When the ultraviolet photons are emitted from an ultraviolet lamp, then the undergo wavelength selection (energy selection) in a spectrometer before being focused on the surface of a sample placed on the sample stage (in the open air). Due to the

photoelectric effect, when the photoelectrons are discharged from a material surface, then the electrons are counted by an open counter, and the count is processed and the results displayed on a PC. The wavelength λ of the ultraviolet radiation is converted into the light energy E using the following equation.

$$E = h\nu = hc/\lambda \quad (3.5)$$

Where h is the Plank constant, ν is the frequency, and c is the speed of light). The value of the threshold energy of photoemission, which corresponds to the ionization potential, is determined from the energy of an interesting point between the background line and the extrapolated line of the linear portion of square root plots of the photoemission yield. If the sample is metal, the value of the threshold energy of photoemission corresponds to the work function. Figure-3.18 shows a system configuration and measurement samples of PYSA measurement (AC-2 series).

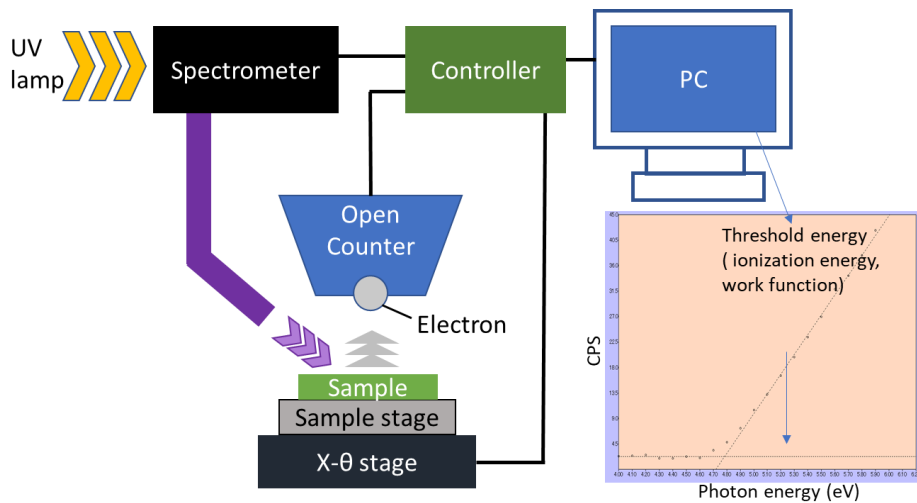


Figure-3.18: Schematic diagram of a PYSA system configuration with PC screen of a measurement sample of AC-2 by PYSA system.

The energy diagram shown in figure-3.19 explains the orbits and energy of electrons inside a material. It is a fundamental diagram for understanding how electronic devices work. The values measured by the photoelectric emission threshold energy) are work function (for metals) and ionization potential (for semiconductors and organic materials). This, therefore, reveals the valence band upper-end energy for metals and semiconductors and the HOMO energy for organic materials.

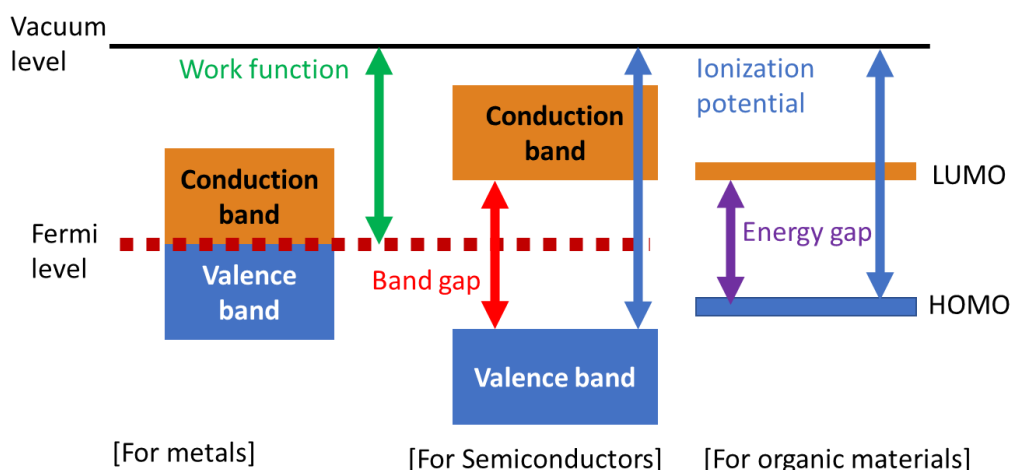


Figure-3.19: Energy band diagram for metals, semiconductors or organic materials measured by PYSA system configuration

3.2.8 Four-probe method for sheet resistance measurement

Sheet resistance is an important property of many materials, quantifying the ability for the charge to travel along with uniform thin films. Like, this property is critical in the creation of high-efficiency perovskite photovoltaic devices, where low sheet resistance materials are needed to extract charge. The most common technique used for measuring sheet resistance is the *four-probe method*. This technique involves using four equally spaced, co-linear probes (known as a four-point probe) to make electrical contact

with the material. A DC current is applied between the outer two probes, and a voltage drop is measured between the inner two probes. The sheet resistance can then be determined using the following equation:

$$R_s = \frac{\pi}{\ln(2)} \frac{\Delta V}{I} = 4.53 \frac{\Delta V}{I} \quad (3.6)$$

Where, R_s is the sheet resistance, ΔV is the change in voltage measured between the inner probes, and I is the current applied between the outer probes. The sheet resistance is expressed with the units $\Omega/\text{sq.}$, or “ohms per square” to differentiate it from bulk resistance. Figure-3.20 (a) shows a schematic diagram of a four-probe method, and (b) it's an equivalent circuit diagram that shows the wire resistance (R_W), contact resistance (R_C), and sample resistance (R_S). The green arrows represent the current flow.

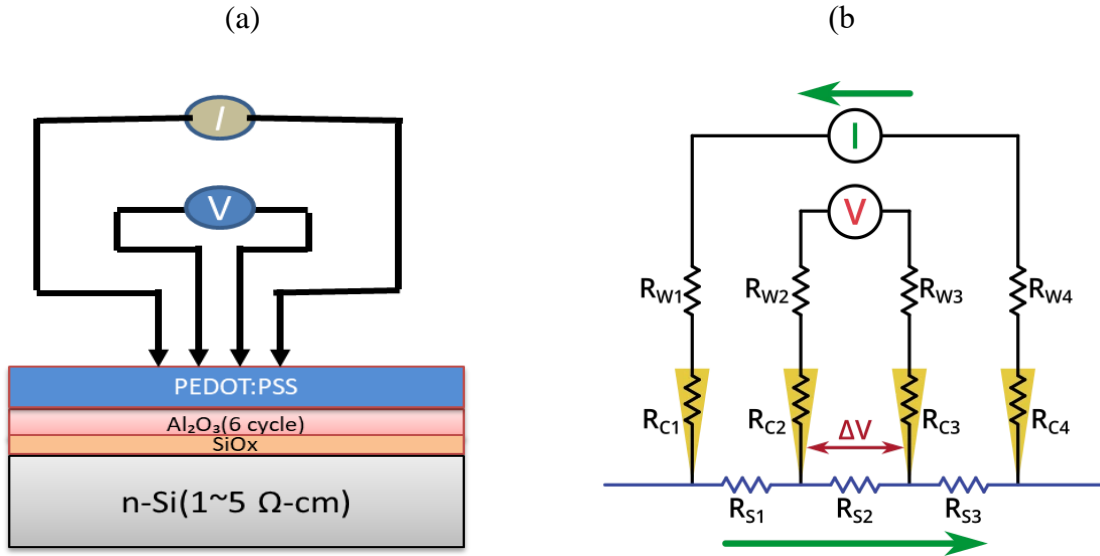


Figure-3.20 : (a) Schematic diagram of PEDOT:PSS/ AlO_x / $ch\text{-SiO}_x$ /n-Si device measuring sheet resistance by a four-probe circuit, and (b) its equivalent circuit diagram.

Bibliography

- [1] S.M. George, A.W. Ott, J.W. Klaus, "Surface Chemistry for Atomic Layer Growth", J. Phys. Chem. **100**, 13121 (1996).
- [2] G.S. Higashi, C.G. Fleming, "Sequential surface chemical reaction limited growth of high quality Al₂O₃ dielectrics", Appl. Phys. Lett. **55**, 1963 (1989).
- [3] A.C. Dillon, A.W. Ott, J.D. Way, S.M. George, "Surface chemistry of Al₂O₃ deposition using Al(CH₃)₃ and H₂O in a binary reaction sequence", Surf. Sci. **322**, 230 (1995).
- [4] A.W. Ott, K.C. McCarley, J.W. Klaus, J.D. Way, S.M. George, "Atomic layer-controlled deposition of Al₂O₃ films using binary reaction sequence chemistry", Appl. Surf. Sci. **107**, 128 (1996).
- [5] A.W. Ott, J.W. Klaus, J.M. Johnson, S.M. George, "Al₂O₃ thin film growth on Si (100) using binary reaction sequence chemistry", Thin Solid Films **292**, 135 (1997).
- [6] J. Fan, K. Sugioka, K. Toyoda, "Low-Temperature Growth of Thin Films of Al₂O₃ by Sequential Surface Chemical Reaction of trimethylaluminum and H₂O₂" Jpn. J. Appl. Phys. **30**, L1139 (1991).
- [7] H. Kattelus, M. Ylilammi, J. Saarilahti, J. Antson, S. Lindfors, "Layered tantalum-aluminum oxide films deposited by atomic layer epitaxy", Thin Solid Films **225**, 296 (1993).
- [8] K. Kukli, M. Ritala, M. Leskela, J. Jokinen, "Atomic layer epitaxy growth of aluminum oxide thin films from a novel Al(CH₃)₂Cl precursor and H₂O", J. Vac. Sci. Technol. A **15**, 2214 (1997).
- [9] M. Ritala, K. Kukli, A. Rahtu, P.I. Räsänen, M. Leskela, T. Sajavaara, J. Keinonen,

“Atomic layer deposition of oxide thin films with metal alkoxides as oxygen sources”, Science **288**, 319 (2000).

Chapter 4

ALD- AlO_x related result and discussion

4.1 Fundamental properties of AlO_x film deposited by ALD

4.1.1 ALD- AlO_x film characterization

4.1.1.1 ALD- AlO_x film thickness

AlO_x film thicknesses were measured using a spectroscopic ellipsometer (S.E.). Values of Ψ and Δ that obtained over the spectral range of 1.5-6.5 eV for an incidence angle of 70° . This incidence angle is close to the silicon Brewster angle of $\theta_B=75.5^\circ$. Measured data were fitted using a least-squares algorithm. AlO_x and SiO_x have virtually identical optical constants. Consequently, a simple ellipsometry measurement yields only the sum of the AlO_x and SiO_x film thicknesses. It is needed to determine the true AlO_x thickness and the thickness of an interfacial SiO_2 layer on the n-Si substrate, a procedure was employed that utilized simultaneous ALD- AlO_x growth on both an HF-etched Si wafer and a Si wafer with native oxide. The thickness of the native SiO_2 layer was initially measured on the Si (100) wafer. Using the bulk SiO_2 refractive index and the Ψ and Δ values from the S.E. analysis algorithm yielded a SiO_2 native oxide thickness of 31 \AA .

Because of high tunneling and leakage currents, ultrathin SiO_2 layers can exhibit a different refractive index, n , then the bulk oxide. The corrected refractive index for a SiO_2 layer with a thickness, T_{ox} , ranging from 1.4 to 8 nm can be obtained using [1]:

$$n_o = 2.139 - 8.991 \times 10^2 T_{ox} + 1.872 \times 10^{-3} (T_{ox})^2 \quad (4.1)$$

With this new refractive index, another fitting was performed to determine a new

thickness. This fitting was obtained for both the refractive index and the oxide thickness. The native oxide thickness was found to be 23 Å based on the corrected refractive index $n=1.94$.

Subsequently, the AlO_x thickness was measured for the ALD- AlO_x films grown on the n-Si substrate with the native oxide. Using a native oxide SiO_2 layer thickness of 23 Å, the AlO_x thickness was obtained by subtracting the contribution of the underlying SiO_x film from the total measured thickness. Assuming the same ALD- AlO_x growth rate on both the HF-etched n-Si and the native oxide SiO_2 layer on n-Si, the SiO_x interfacial layer was determined on the HF-etched n-Si after depositing AlO_x . This analysis yielded a 13 Å thick SiO_x interfacial oxide layer on an HF-etched Si (100) substrate after 120 AB cycles of ALD- AlO_x at 180°C. Results from numerous samples revealed that a SiO_x oxide layer thickness of 13 ± 2 Å was observed after 50-170 AB cycles of ALD- AlO_x at substrate temperatures from 160-220°C.

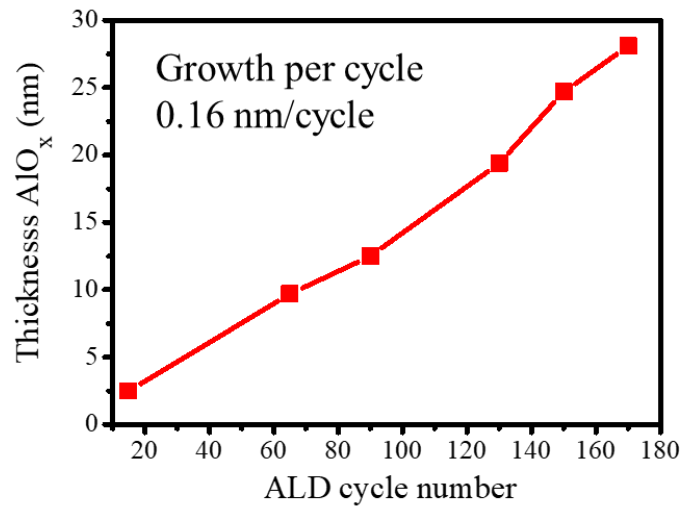


Figure-4.1: AlO_x thickness plotted as a function of ALD number of cycles,

Figure 4.1 shows the ALD- AlO_x films thickness as a function of ALD no of cycles. Here the substrate temperature or growth temperature was kept at 180°C . At fixed substrate temperature, the film thickness increases linearly with the increasing ALD no of cycles from 15 to 180 cycles. And the growth rate at fixed substrate temperature was observed of 0.16nm per cycle.

Figure 4.2 shows the ALD- AlO_x film growth rate plotted against the different substrate temperatures from 160 to 220°C . The film growth rates show a minimum of 0.10 nm/cycle at 200°C . These results indicate that higher growth temperatures may lead to higher densities and higher dielectric constants. Also, it is shown that higher temperatures lead to a decrease in incorporated hydroxyls in ALD- AlO_x films. To understand the chemical bond composition and surface morphology on substrate temperate, we also studied the surface morphology by AFM and FTIR analysis.

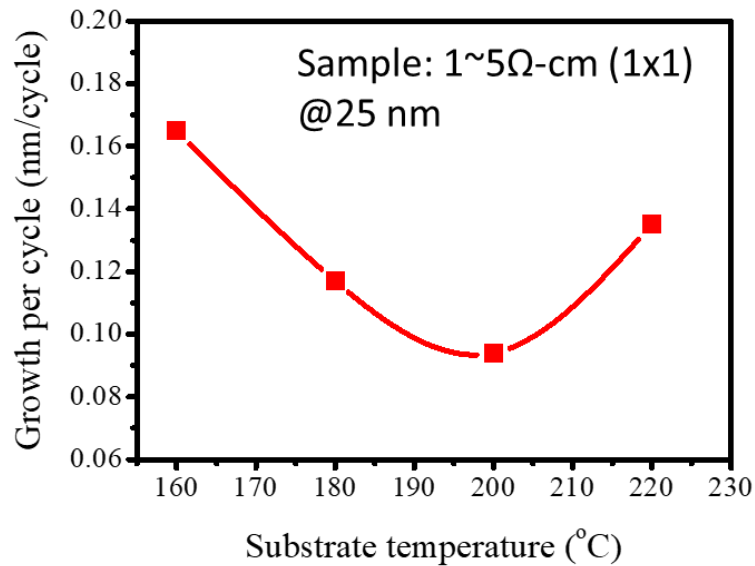


Figure-4.2: The growth rate of AlO_x film vs. substrate temperature

4.1.1.2 AFM study

Figure-4.3 shows the AFM images for 25nm thick ALD- AlO_x film at different substrate temperatures, whereas the substrate size was $1 \times 1 \mu\text{m}^2$ and the z-axis was 1nm. At the substrate temperature of 160°C , some large peaks and holes were observed on the surface, which RMS values were about 0.52nm. One of the possible reasons is that at lower substrate temperature, the sticking probability of TMA is comparatively lower than the H_2O . But when the substrate temperature was increased, then the giant peaks and holes were decreased with the decreasing of RMS value to 0.29 nm at 200°C . And after that, the RMS roughness again was increased due to increased large peaks and holes compared with 200°C . These results indicate that the optimized uniform ALD- AlO_x film is achieved on the n-Si substrate at the 200°C substrate temperature due to the increased sticking of TMA precursor than the H_2O precursor.

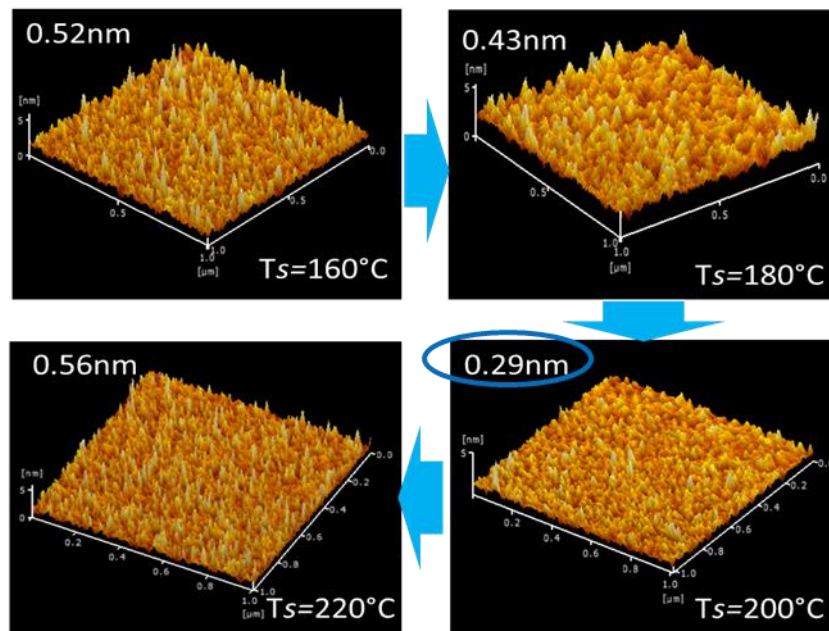


Figure-4.3: AFM images of ALD- AlO_x films at a different substrate temperature

To understand the chemical bond composition of the ALD- AlO_x on the n-type c-Si, FTIR spectra for the corresponding films were analyzed, shown in figure-4.4. Table-4.1 summarizes the local vibrational mode of ALD- AlO_x related to the absorption peaks were achieved from the films c-Si

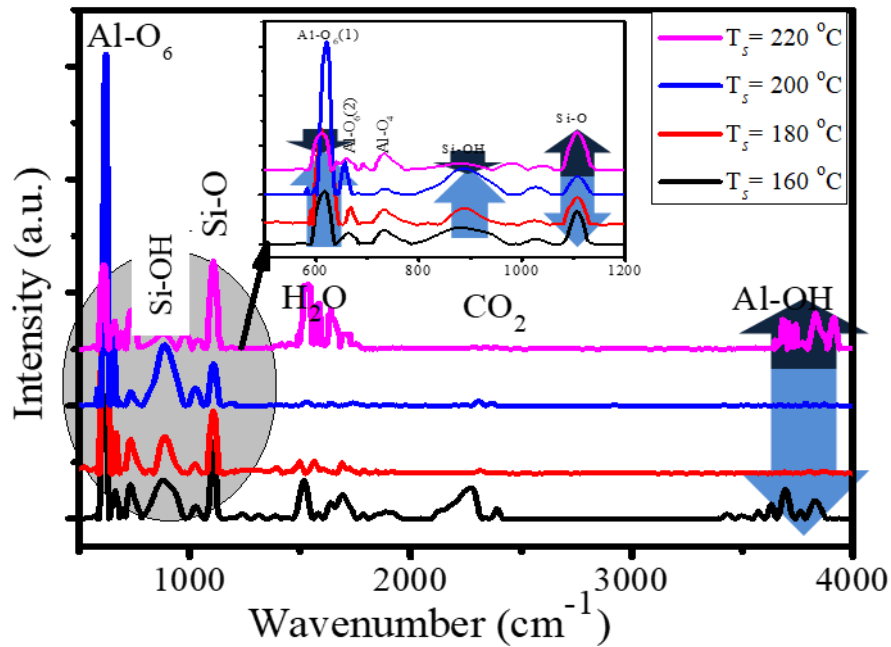


Figure-4.4: FTIR spectra of ALD- AlO_x films at a different substrate temperature

Figure-4.4: FTIR spectra of ALD- AlO_x films at a different substrate temperature from 160°C to 220°C. In the case of ALD- Al_2O_3 films at the substrate temperature of 160°C, the Al(OH) stretching peak in the range of 2600-3800 cm^{-1} is prominent. However, this peak disappears as the substrate temperature is increased up to 200°C, while peaks are related to O-Al-O (550-750 cm^{-1}), and Si-O-Al (~1100 cm^{-1}) emerge. The first peak can be assigned to the Al-O bending modes (expected to appear at approximately 603 cm^{-1}) for octahedral AlO_6 as well as the stretching vibration of tetrahedral (AlO_4) (which should appear in the range of 728-886 cm^{-1}). Several fine peaks were also observed

attributing to Si-OH, Si-O-Si, or Al-O-Si band at 300-1100 cm^{-1} , where the Si-O related peak appeared at 1103 cm^{-1} , which were intense at 200°C temperature. Also, the Al-OH related peaks at 3600 cm^{-1} wavenumber were reduced at that substrate temperature. These findings suggest that the sticking of TMA and removal of the methyl group by water supply is balanced at 200°C. Then, in the following, we deposit ALD- Al_2O_3 films at a substrate temperature of 200°C.

Table 4.1: Local vibration modes of AlO_x related FTIR peaks

Wavenumber (cm^{-1})	Molecule	Vibrational Mode	Surrounding	Reference
400-530	Al-O	Stretching	Octahedral matrix	2-6
550-750	O-Al-O	Bending	Octahedral and tetrahedral matrix	2-7
750-850	Al-O	Stretching	tetrahedral matrix	2-7
900-1200	Si-O/O-Si-O/ Si-OH	Stretching	SiO/SiO ₂	5-6
1300-1750	H-O-H	Bending	tetrahedral and octahedral γ - Aluminum ions	6
2300-2350	O-C-O	Stretching	Al_2O_3	7
3000-3600	Si-OH	Stretching		8
2600-3800	O-H	Stretching	Al-OH	6

Figure-4.5 shows the effective lifetime minority carrier lifetime of ALD deposited AlO_x on n-type c-Si before and after rapid thermal annealing (RTA) at 425°C

for 15 min under vacuum condition using the μ -PCD method as discussed earlier. The effective lifetime values were determined using the following equation:

$$\frac{1}{\tau_{eff}} = \frac{1}{\tau_{bulk}} + \left[\frac{W}{2S} + \frac{1}{D_n} \left(\frac{W}{\pi} \right)^2 \right]^{-1} \quad (4.2)$$

where τ_{bulk} is the bulk lifetime of the Si substrate, S is the surface recombination velocity, W is the substrate thickness ($250 \pm 0.060 \mu\text{m}$), and D_n is the diffusion length (37 nm for c-Si. [9,10] The effective lifetime values increased with the increase in ALD number of cycles before and after RTA, and its value reached to 280-300 μs for approximately 25nm thick ALD- AlO_x on the n-Si substrate after RTA. However, τ_{eff} was decreased for 6–15 cycles corresponding to a 1-2-nm thickness after RTA. One of the possible reasons is that at the lower thickness of AlO_x , the passivation quality of AlO_x coated on c-Si is deteriorating due to the reduction of oxidation at the c-Si surface after rapid thermal annealing under vacuum condition. Whereas the passivation quality is increased with the increased oxidation of n-Si surface for the higher thickness of AlO_x on the n-Si surface.

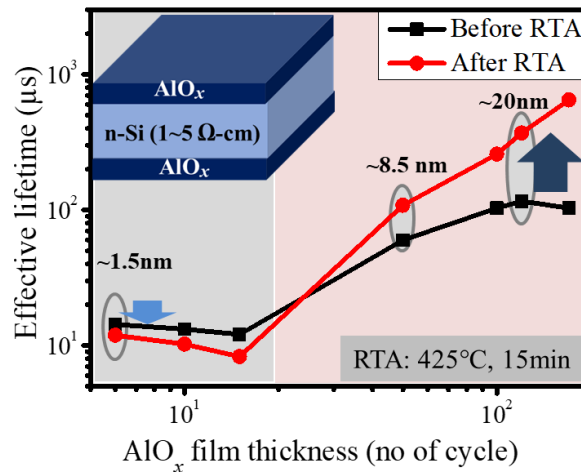


Figure-4.5: Effective minority carrier lifetime of ALD- AlO_x on the n-Si substrate at different values of layer thickness.

Thus, we classified two different thickness regimes of ALD- AlO_x . One is the thicker layer thickness regimes of about 20 nm, and another is the thinner regime of 1-2 nm. We applied both thickness regimes of AlO_x as a strong field-inversion layer for the PEDOT:PSS/n-Si anode interface, which was described in the next part.

4.2 Effect of ALD- AlO_x island at the PEDOT:PSS/n-Si interface property by the UV photolithography process

4.2.1 Effect of AlO_x island at the PEDOT:PSS/n-Si interface for different area ratio of AlO_x and PEDOT:PSS

Figure-4.6(a) shows the $1/C^2$ -V plots measured at 100 kHz for the pristine PEDOT:PSS device with and without different area ratio AlO_x island to PEDOT:PSS. The built-in field, V_{bi} , and donor density, N_d can be calculated through the following well-known equation:

$$\frac{1}{C^2} = \frac{2 \left(\frac{kt}{q} - V_{bi} - V \right)}{q A^2 \epsilon_0 \epsilon_{si} N_d} \quad (4.3)$$

where A is the diode area, and $\epsilon_0 \epsilon_{si}$ is the permittivity of silicon [11].

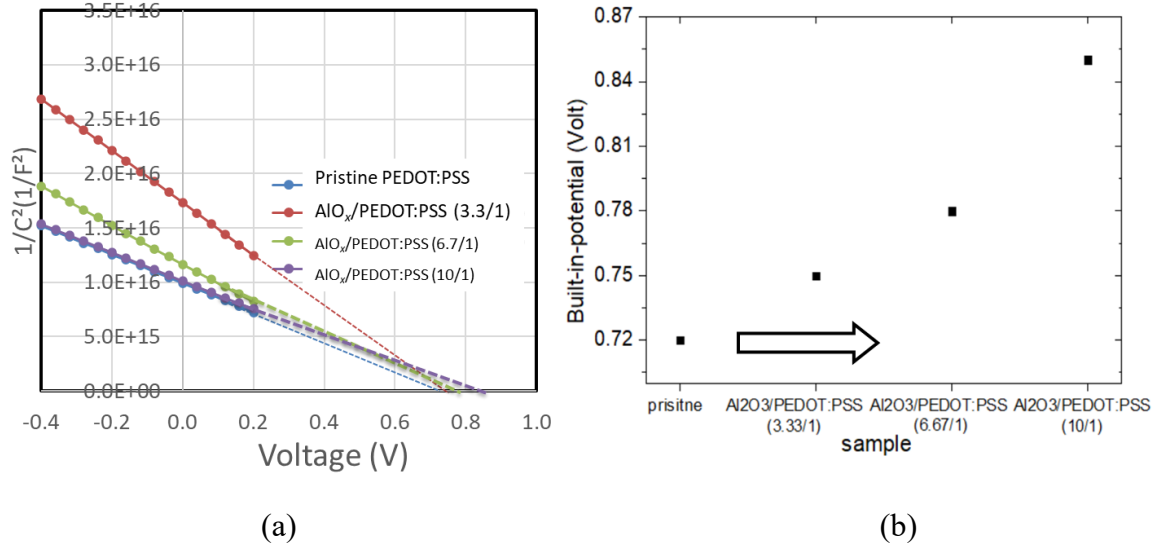


Figure-4.6: (a) $1/C^2$ vs. voltage (b) summarized built-in field of PEDOT:PSS/n-Si solar cell with AlO_x island at different area ratio of AlO_x island & PEDOT:PSS

Through the above equation (4.2), we calculated the built-in field, which is summarized in figure 4.6(b) for different area ratios of AlO_x island compared with pristine PEDOT:PSS device. In the case of pristine PEDOT:PSS device, V_{bi} is 720mV, which is increased to 750 to 850mV for the increasing AlO_x island ratio compared to PEDOT:PSS area. These results indicate that a strong inversion appeared at the PEDOT:PSS/n-Si interface once the higher thickness of AlO_x island film was inserted at the interface.

Figure-4.7 (a,b) shows the photocurrent-voltage (J-V) curve for the AlO_x island inserted PEDOT:PSS/n-Si solar cells for different area ratios of AlO_x island and PEDOT:PSS compared with pristine PEDOT:PSS device. From the dark J-V curve (figure-4.7(a)), we found that the reverse current density for all area ratios of AlO_x island/PEDOT:PSS device is suppressed to be lower compared with the pristine PEDOT:PSS device. On the other hand, the current density is higher for the AlO_x island device shown in figure-4.7(b). These suggest that the mobility in this inversion layer,

which is expected to increase with increasing inversion strength due to improved screen of donor ions, is enough to extract carriers over larger distances.

However, contrary to our expectations, the open-circuit voltage, V_{oc} , was not significantly increased. One of the possible reasons is that due to the increased sheet resistance of the higher area ratio of AlO_x island at the PEDOT:PSS/n-Si device, which is confirmed from the forward dark J-V curve. For this reason, the fill factor (F.F.) markedly deteriorated with increasing the area ratio of AlO_x island, which reduce the overall efficiency. The details of photovoltaics parameters are summarized in table-4.2.

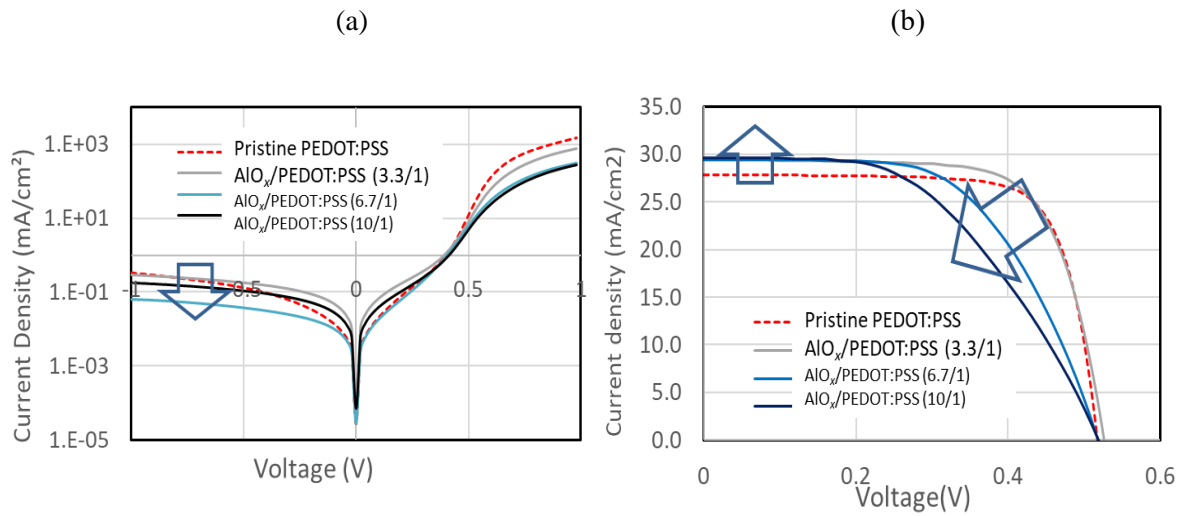


Figure-4.7: Photocurrent-Voltage (J-V) curve for the PEDOT:PSS/n-Si solar cell with AlO_x island under (a) dark condition, (b) illumination at different area ration of AlO_x island & PEDOT:PSS

Table-4.2: Photovoltaic parameters of the pristine PEDOT:PSS/n-Si device with a different area ratio of AlO_x island & PEDOT:PSS

Device type	Jsc (mA/cm ²)	Voc (V)	FF	PCE (%)
Pristine PEDOT:PSS	27.7	0.516	0.75	10.8
AlO _x /PEDOT:PSS (3.3/1)	29.4	0.525	0.72	11.0
AlO _x /PEDOT:PSS (6.7/1)	29.38	0.517	0.58	8.84
AlO _x /PEDOT:PSS (10/1)	28.07	0.518	0.50	7.68

Figure-4.8(a) shows the external quantum efficiency (EQE) for the pristine PEDOT:PSS device with all different area ratios of AlO_x island, whereas figure 4.8(b) shows the reflectance curve for the corresponding device. From the EQE curve, it is found that in the case of AlO_x island inserted device, the enhancement of which is photocurrent within the visible spectrum region was found to derive primarily due to a wider depletion width as well as the suppression of the reflection at the corresponding region. These results indicate that the AlO_x island acts as an anti-reflection layer instead of the field passivation layer. Also, we investigated the effect of AlO_x island at PEDOT:PSS/n-Si interface for different donor density substrate where the AlO_x island area was 15μm x 15 μm with fixed gap interval of 15μm. Later, we will discuss it.

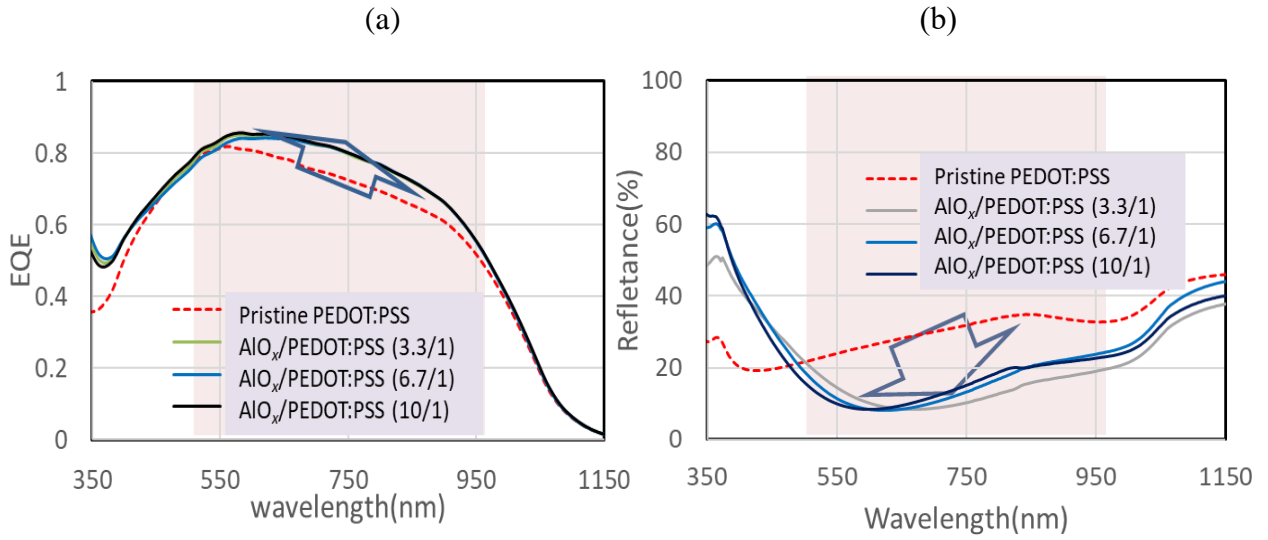


Figure-4.8: (a) External quantum efficiency (EQE) (b) Reflectance of PEDOT:PSS/n-Si solar cell with AlO_x island at different area ration of AlO_x island & PEDOT:PSS

4.2.2 Effect of AlO_x island at the PEDOT:PSS/n-Si interface for different donor density substrate

Figure-4.9 (a,b) shows the photocurrent-voltage (J-V) curve for the AlO_x island inserted PEDOT:PSS/n-Si solar cells for different donor density substrate for AlO_x island and PEDOT:PSS (15 μm x 15 μm) compared with pristine PEDOT:PSS device. The dotted line indicates the pristine device for all donor density, and the solid line indicates the AlO_x island inserted device. From the dark J-V curve (fig-4.9(a)), we found that the reverse current density for all donor density of AlO_x island/PEDOT:PSS device is suppressed to be lower compared with the pristine PEDOT:PSS device for all donor density substrate whereas the current density is higher for the AlO_x island device shown in figure-4.9(b). These suggest that the mobility in this inversion layer, which is expected to increase with increasing inversion strength due to improved screen of donor ions, is enough to extract carriers over more considerable distances. Figure-4.9(c) shows the external quantum

efficiency for the corresponding device, which indicates that the AlO_x island for different donor density devices acts as an anti-reflection layer instead of the passivation layer.

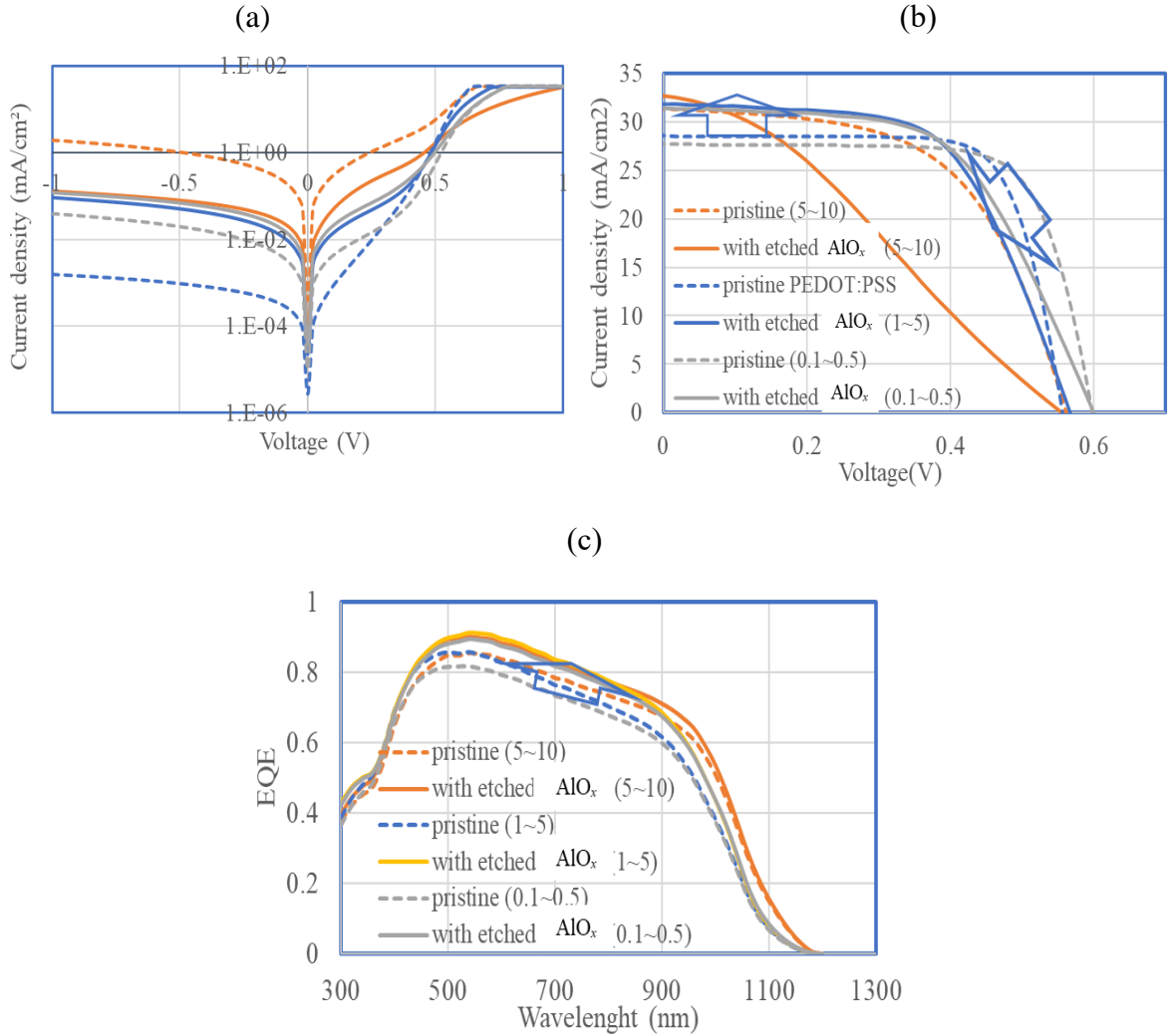


Figure-4.9: Photocurrent-Voltage (J-V) curve for the PEDOT:PSS/n-Si solar cell with AlO_x island under (a) dark condition, (b) illumination (c) EQE at different donor density substrate

Figure-4.10(a,b) shows the summarization curve of the PV performance parameters for all donor density substrate. In figures, the open black square and open red

circle indicate the current density, open-circuit voltage, fill factor (FF) and power conversion efficiency (PCE) for the different donor density of the pristine device. And filled square and circled indicate the AlO_x island device for all donor density devices. In figure-4.10(a), the current density is increased once the AlO_x island was inserted at the PEDOT:PSS/n-Si interface. In the meantime, there is no significant change of open-circuit voltage once the AlO_x island was inserted at that interface. On the other hand, the FF and PCE were deteriorated due to a higher resistive effect.

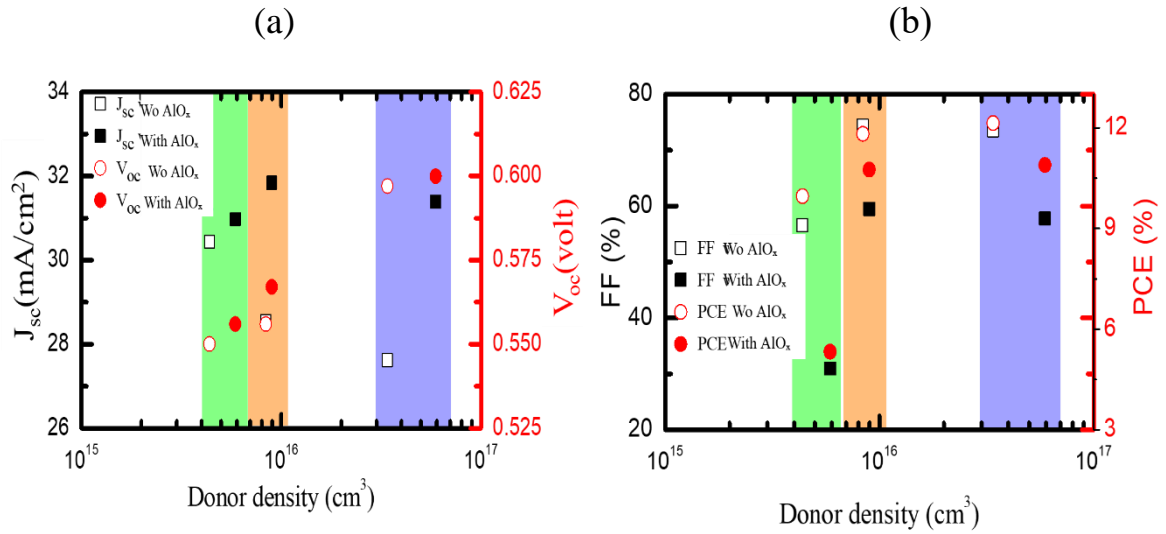


Figure-4.10: (a) Current density and open-circuit voltage curve, (b) fill-factor and power conversion efficiency for different donor density substrate compared with pristine PEDOT:PSS device.

Figure-4.11 shows the carrier concentration in the inversion layer and built-in potential as a function of different donor density. From this figure, it is indicated that at higher donor density, the higher open-circuit voltage with the lower carrier concentration in the inversion layer.

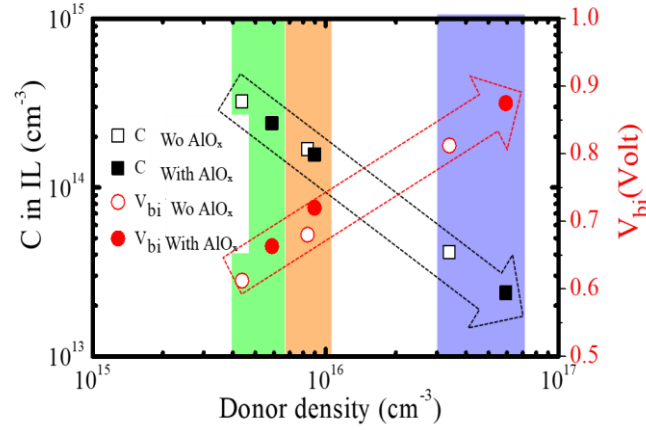


Figure-4.11: Carrier concentration and built-in potential as a function of different donor density substrate

From the above discussion regarding the effect of AlO_x island at the PEDOT:PSS/n-Si for both different area ratios and donor density, it is depicted that a higher built-in field is obtained due to the increased area ratio of AlO_x island compared with PEDOT:PSS, which revealed that a stronger inversion layer had been produced at the PEDOT:PSS/n-Si interface. Also, the higher donor density substrate shows the high built-in potential. Though the photocurrent-voltage (J-V) curve shows, the current density is increased for the AlO_x inserted devices compared with the pristine device, which is confirmed from the enhancement of photocurrent as well as the suppression of reflectance in the visible to the near-infrared spectrum region, the V_{oc} is not significantly improved due to the presence of higher sheet resistance. Thus, we found that the AlO_x island here mainly acts as an anti-reflection coating (A.R.C.) layer. Therefore, we turn our study to the effect of the insertion of an ultrathin $\text{AlO}_x/\text{ch-SiO}_x$ oxide stack layer at the PEDOT:PSS/n-Si interface as a tunnel oxide to improve the junction quality.

4.3 Effect of thermally annealed atomic-layer-deposited AlO_x /chemical tunnel oxide stack layer at the PEDOT:PSS/n-type Si interface to improve its junction quality

4.3.1 Effect of FGA and RTA at the stack layer of ALD- AlO_x /*ch*- SiO_x /c-Si

4.3.1.1 Effective lifetime of ALD- AlO_x /*ch*- SiO_x stack layer on c-Si

Figure 4.12(a) shows the correlation between τ_{eff} and the number of ALD cycles on the *n*-Si substrate before and after RTA at 425 °C for 15 min under vacuum. The τ_{eff} increased from approximately 15 to 100 μs with the increase in the number of ALD cycles for the as-deposited AlO_x layer, and it increased markedly for the AlO_x layers with thicknesses exceeding approximately 8.5 nm (50 cycles) after RTA. It reached 280–300 μs in approximately 20-nm-thick AlO_x on *n*-Si (120 cycles), whereas it decreased significantly in 1–3-nm-thick (5–15 cycles) AlO_x layers where the τ_{eff} was 5–15 μs . On the other hand, significant increases in τ_{eff} were obtained by increasing the thickness of the entire AlO_x layer from approximately 1 to 25 nm (150 cycles) by using a combination of FGA and the insertion of ultra-thin *ch*- SiO_x layers at the AlO_x /*n*-Si interfaces.

Figure 4.12(b) shows τ_{eff} of solely six-cycle ALD- AlO_x and six-cycle ALD- AlO_x /*ch*- SiO_x (1~3nm) stacks of ultra-thin layers on the *n*-Si substrate before and after FGA at 560 °C for 30 min. The τ_{eff} of six cycles of solely ALD- AlO_x increased from 48 to 70 μs after FGA, and for the ALD- AlO_x /*ch*- SiO_x (25 and 80 °C) stacked thin layers, τ_{eff} increased to 300–331.8 μs . These findings indicate that the local chemical bonding configuration of the *ch*- SiO_x suboxide at the ALD- AlO_x /*n*-Si interface dominates the passivation quality.

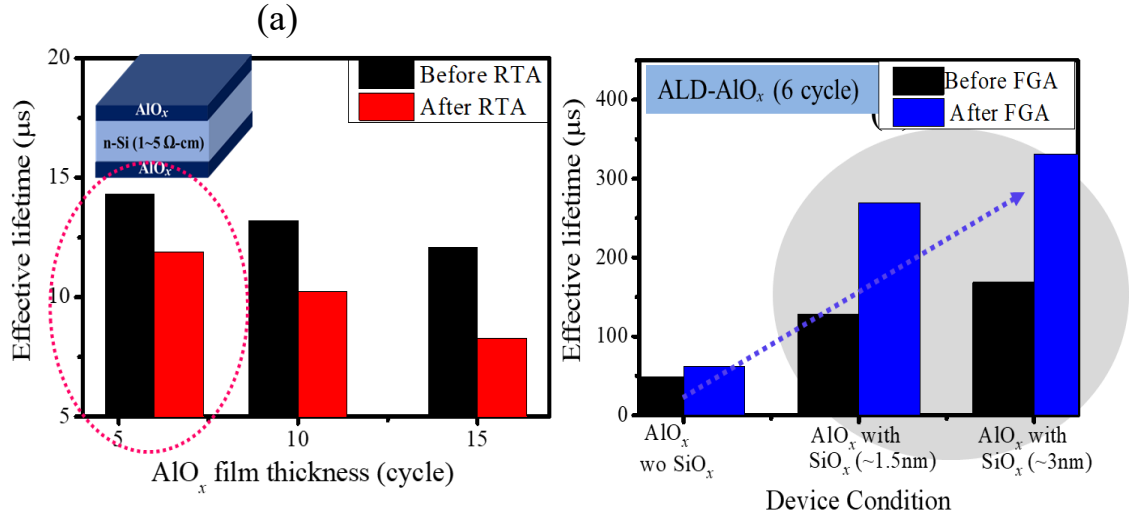


Figure-4.12 (a) Correlation between τ_{eff} and ALD number of cycles for ALD- AlO_x on n-Si before and after RTA for 5-15 cycles. (b) τ_{eff} of ALD- AlO_x (six cycles) and ALD AlO_x/ch SiO_x stack layers on n-Si (1–5 $\Omega \cdot cm$) substrate before and after FGA at 560 °C for 30 min.

4.3.1.2 Effect of RTA and FGA on the ALD- AlO_x with and without ch - SiO_x (1~3nm) by C-V study

To understand the effect of RTA and FGA at the AlO_x/n -Si interface with and without ch - SiO_x (1~3nm), we have investigated the Capacitance-Voltage study. Figure-4.13 shows a capacitance-voltage curve for AlO_x/ch - SiO_x/n -Si interface at high frequency, where both forward and reverse capacitance are indicated. Here a hysteresis curve has occurred for all the corresponding samples from which we can measure the flat-band voltage. D. Hoogeland et al., suggests that the negative fixed charge density Q_f can be calculated from the following equation

$$V_{FB} = \phi_{MS} - \frac{Q_f}{C_{ox}} \quad (4.4)$$

Where V_{fb} is the flat band voltage, Q_{MS} is the Al-Si work function, and C_{ox} is the oxide charge at the accumulation region.

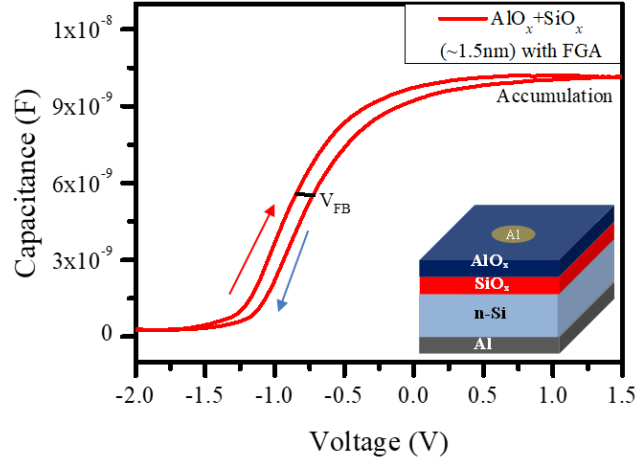


Figure-4.13: A typical C-V curve for the MIS device.

Figure-4.14(a) shows the negative fixed charge density for the AlO_x/n -Si interface with and without ch - SiO_x for as-deposited, for RTA and FGA condition. At the AlO_x/n -Si interface, the negative fixed charge density (Q_f) is maximum for the FGA condition, which means that the negative fixed charge density is more stored near the n-Si interface for the FGA condition compared with as-deposited and RTA. That indicates the evaluation of the dangling bond near the surface is increased due to the FGA effect. The same phenomena have appeared for AlO_x/ch - SiO_x/n -Si interface also.

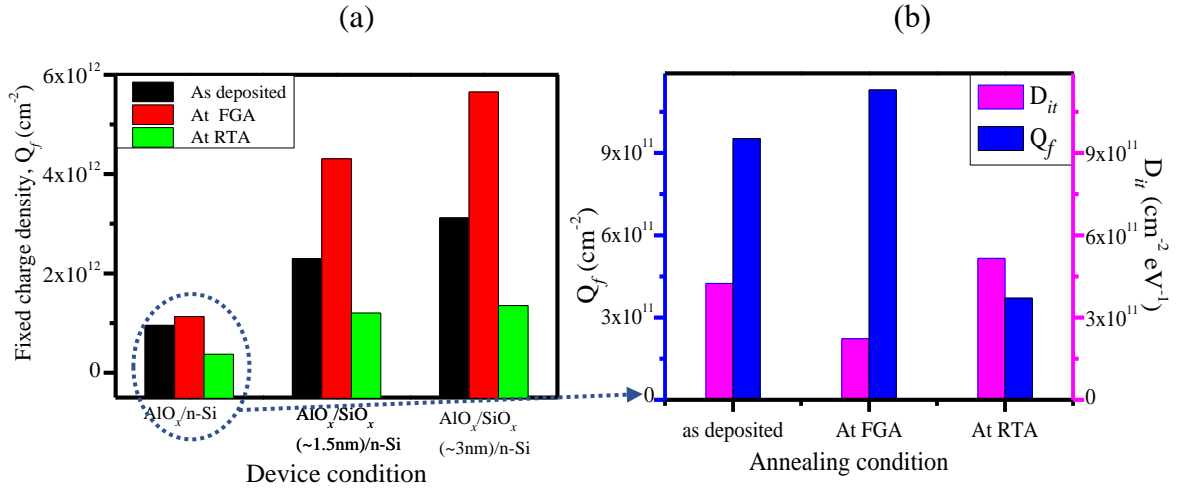


Figure-4.14: (a) negative fixed charge density (Q_f) as a function with $\text{AlO}_x/\text{n-Si}$ with and without ch-SiO_x (1~3nm) for as-deposited, FGA and RTA condition, (b) Q_f and D_{it} as a function with different annealing condition.

Figure-4.14(b) shows the negative fixed charge density and the interface trap density for $\text{AlO}_x/\text{n-Si}$ interface for different annealing conditions. The interface trap density can be derived from figure-4.13 and the following equation:

$$D_{it}(\phi_s) = \left(\frac{C_{ox}}{q} \right) \left(\frac{C_{hf}}{(C_{ox} - C_{hf})} - \frac{C_{lf}}{(C_{ox} - C_{hf})} \right) \quad (\text{cm}^{-2} \text{eV}^{-1}), \quad (4.5)$$

where, C_{lf} and C_{hf} are the low and high measurement frequencies of 10 kHz and 1 MHz, respectively. From the figure, it is found that the interface trap density is minimum, with the maximum negative fixed charge density was found due to the FGA effect compared with as deposited or RTA treated samples. These findings indicate that due to the increasing dangling band at the interface, the interface trap density at the interface is reduced with the increase of fixed charge density. For more understanding, the effect of the FGA and RTA on the local chemical bond, we also investigated the X-ray

photoelectron spectroscopy (XPS) for the $\text{AlO}_x/\text{n-Si}$ interface with and without $ch\text{-SiO}_x$.

4.3.1.3 Study of XPS for the ALD- $\text{AlO}_x/\text{SiO}_x$ stack layer on c-Si with and without FGA.

Figure 5.15(a)-(c) show the XPS Si(2p) core energy region spectra for six-cycle ALD $\text{AlO}_x/\text{n-Si}$ interface regions with and without tunnel oxide $ch\text{-SiO}_x$ (1~3nm) layers before and after RTA (425 °C for 15 min) and FGA (560 °C for 30 min), as well as those of the suboxide SiO_x at 100– 105 eV. A detailed analysis of the chemical shifts for the Si(2p) peaks reveals the presence of the SiO_x suboxide components Si^{2+} , Si^{3+} , Si^* , and Si^{4+} in addition to the Si metal peaks at 99.3 eV and 99.9 eV for $2p_{3/2}$ and $2p_{1/2}$, respectively. Among these components, the Si^* peak exhibited an unknown valence state that does not correspond to the Si^+ , Si^{2+} , Si^{3+} , and Si^{4+} components. For as-deposited six-cycle ALD- AlO_x on n-Si with and without $ch\text{-SiO}_x$ (1~3nm) layers, the Si^+ peak at 100.3 eV and the broadband peaks forming a shoulder in the higher energy region. In addition, the suboxide Si^* peak at 101.9 eV in the as-deposited $\text{AlO}_x/\text{n-Si}$ interface shifted to the higher energy of 102.9 eV, and the intensities of Si^{2+} , Si^{3+} , Si^* , and Si^{4+} were increased by inserting tunnel oxide $ch\text{-SiO}_x$ layers. However, all the samples exhibited similar spectra comprising of Si^* and Si^{4+} components with smaller broadband peaks attributed to the formation of shoulders by Si^{2+} and Si^{3+} after FGA (Fig. 5.15(b)). On the other hand, the suboxide Si^* and Si^{4+} peaks at the $\text{AlO}_x/\text{n-Si}$ interface after RTA shifted to lower regions compared with as-deposited and FGA-treated samples with and without $ch\text{-SiO}_x$ insertion.

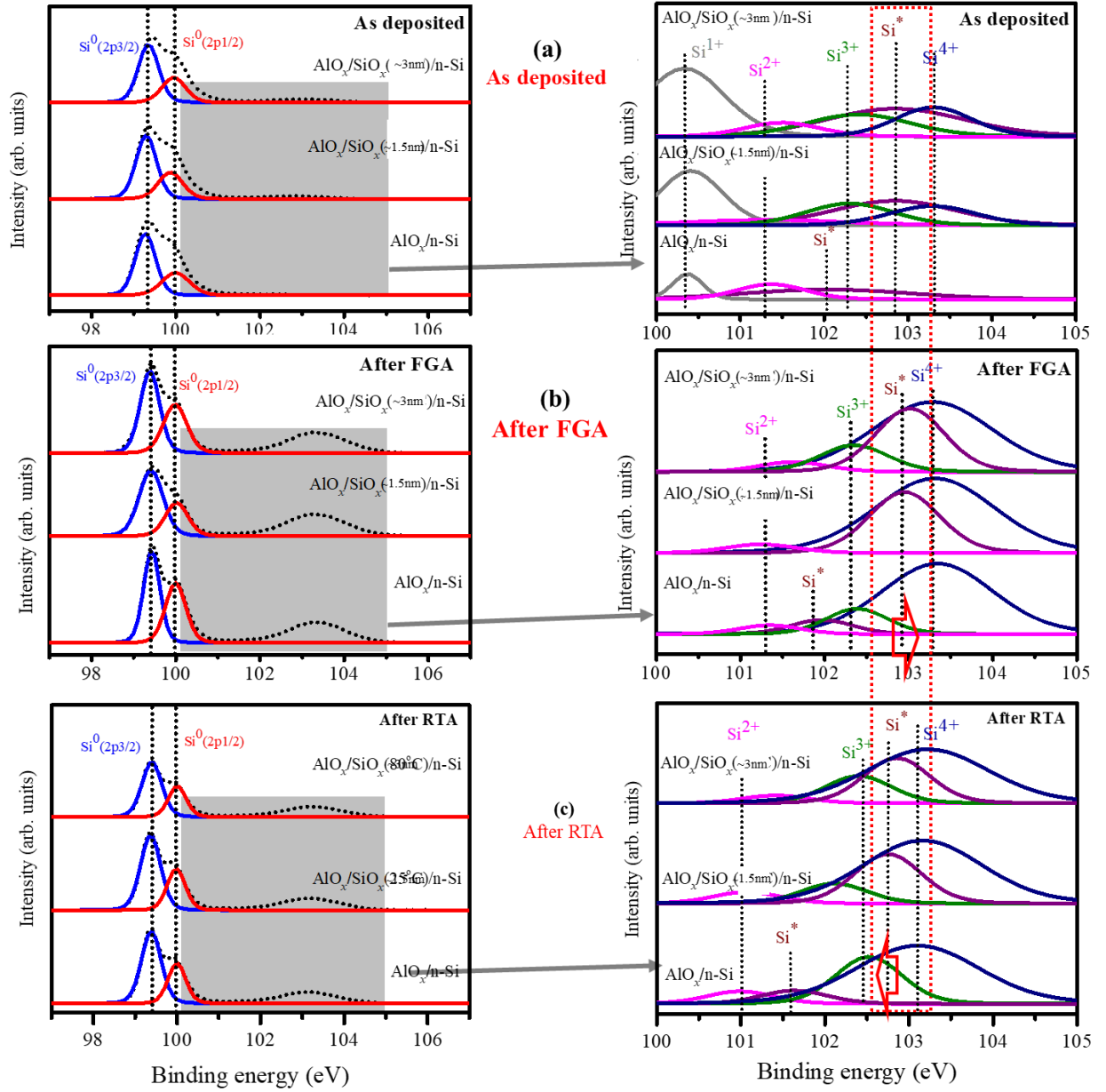


Figure-4.15: XPS Si(2p) core energy region spectra of ALD-AlO_x (six cycles) with and without tunnel oxide *ch*-SiO_x (1~3nm) layers (a) as-deposited, (b) after FGA at 560 °C for 30 min, and (c) RTA at 425 °C for 15 min. The subfigures on the left show the spectra between 100-105 eV. The subfigures on the right show the enlarged view of the same energy region.

Table 4.3 summarizes the chemical shifts of the SiO_x suboxide components, Si^{2+} , Si^{3+} , Si^* , and Si^{4+} on the basis of the $\text{Si}(2p)$ core levels for as-deposited, RTA, and FGA treated ALD- AlO_x (six cycles)/n-Si junctions with and without tunnel oxide $ch\text{-SiO}_x$ (1~3nm) layers. The binding energy of Si^* , $\text{B.E.}(\text{Si}^*)$, shifted to a higher energy value of 2.55 eV measured from the $\text{Si}^0(2p_{3/2})$ energy of 99.3 eV used as a reference value for the as-deposited $\text{AlO}_x/\text{n-Si}$ junction. Moreover, $\text{B.E.}(\text{Si}^*)$ shifted to 3.51 eV and 3.54 eV in the 1~3nm thick $ch\text{-SiO}_x$ tunnel oxide layers, respectively. Furthermore, $\text{B.E.}(\text{Si}^*)$ shifted to 3.57 eV (25 °C) and 3.64 eV (80 °C) after FGA. No significant shift of $\text{B.E.}(\text{Si}^*)$ was observed in the ALD- $\text{AlO}_x/\text{n-Si}$ interface without tunnel oxide $ch\text{-SiO}_x$ layers. However, the $\text{B.E.}(\text{Si}^*)$ shifted to the lower energy values of 2.35 eV, 3.36 eV, and 3.45 eV in ALD- $\text{AlO}_x/\text{n-Si}$ interfaces without $ch\text{-SiO}_x$ layers, the RTA-treated samples with $ch\text{-SiO}_x$ layers sample, and the RTA-treated samples with ~3nm thick $ch\text{-SiO}_x$ layers samples, respectively. The values of $\text{B.E.}(\text{Si}^*)$ were lower than those of as deposited and FGA. This resulted in the lower passivation quality in RTA-treated samples compared to the samples before and after FGA treatment.

Table 4.3: Chemical shifts of SiO_x suboxide components, Si²⁺, Si³⁺, Si^{*}, and Si⁴⁺, from the Si(2p_{3/2}) core energy level used as a reference value for ALD-AlO_x (six cycles) with and without tunnel oxide *ch*-SiO_x (1~3nm) layers before and after FGA and RTA

	Tunnel oxide layer	AlO _x /n-Si			AlO _x /SiO _x (~1.5nm)/n-Si			AlO _x /SiO _x (~3nm)/n-Si		
		As-deposited	W FGA	W RTA	As-deposited	W FGA	W RTA	As-deposited	W FGA	W RTA
Binding energy difference ΔB.E from (Si2p _{3/2}) core energy	ΔB.E. (Si ¹⁺) (eV)	1.2	-		1.12	-		1.01	-	
	ΔB.E. (Si ²⁺) (eV)	2.05	1.84	1.7	2.07	1.87	1.65	2.17	2.14	2.01
	ΔB.E. (Si ³⁺) (eV)	2.89	2.89	3.01	2.86	-	2.82	3.03	2.90	3.01
	ΔB.E. (Si [*]) (eV)	2.47	2.55	2.35	3.51	3.57	3.36	3.54	3.64	3.45
	ΔB.E. (Si ⁴⁺) (eV)	-	3.93	3.72	4.13	3.95	3.79	4.06	3.91	3.82
height ratio (%)	I (Si ⁴⁺)/Si(2p _{3/2})	0.7	22.5	14.6	4.7	27.7	16.1	5.7	31.4	18.7
	I (Si ⁴⁺)/Si(2p _{1/2})	0.9	34.4	26.9	4.8	46.2	28.6	6.7	55.9	33.3

In addition, the ratio of the Si⁴⁺ peak height to the Si(2p_{3/2}) peak height of the ALD-AlO_x (six cycles)/n-Si junctions was approximately 0.7%, which increased to 5.7% and 31.4% with tunnel oxide *ch*-SiO_x layer insertion before and after FGA, respectively. The ratio of the peak height between Si⁴⁺ and Si2p_{1/2} increased from 0.9 to 55.9%. But for RTA treated samples, the intensity ratio is lower than the FGA treated samples. These results indicate that the Si^{*} complex and the suboxide composition ratio in the tunnel oxide *ch*-SiO_x layer contribute to the improvement of the passivation quality at the ALD-AlO_x/n-Si interface. But still, the role of FGA and RTA at the AlO_x/n-Si interface with and without *ch*-SiO_x layers is not clear. To understand the role of FGA and RTA on the chemical bond composition, we have also investigated the Fourier transform infrared ray (FTIR) spectra study, which will be described in the next part.

4.3.1.3 Effect of RTA and FGA on the ALD- AlO_x with and without $ch\text{-SiO}_x$ (1~3nm) by FTIR spectra

Figure-4.16 shows the aluminum octahedra (Al-O_6) and aluminum tetrahedra (Al-O_4). According to several researcher's investigations, if the evaluation of aluminum octahedra (Al-O_6) and aluminum tetrahedra (Al-O_4) intensity is more dominant at the $\text{AlO}_x/\text{n-Si}$ interface, then the passivation quality can be enhanced. To this aim, we also investigate the FTIR study to understand the chemical bond composition of Al-O at the $\text{AlO}_x/\text{n-Si}$ interface.

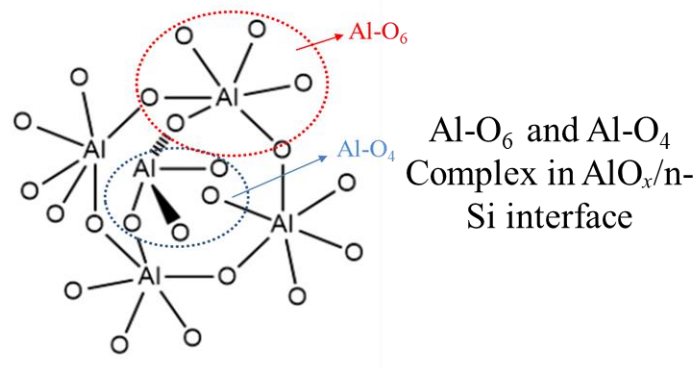


Figure-4.16: Aluminum octahedra (Al-O_6) and aluminum tetrahedra (Al-O_4) complex

Figure- 4.17 (a) shows the FTIR spectra to understand the effect of FGA and RTA at the $\text{AlO}_x/\text{n-Si}$ interface with and without $ch\text{-SiO}_x$ from 500-4000 cm^{-1} wavenumber. Also, from 500-1200, the wavenumber is expanded to figure-4.17 (b). For the $\text{AlO}_x/\text{n-Si}$ interface, the Al-OH bond is observed at the 3700 wavenumbers for all annealing conditions. In the case of FGA treated samples, the Al-OH bond at 3700 cm^{-1} was reduced with the enhancement of Al-O_6 intensity at the 613 cm^{-1} wavenumbers compared with the RTA treated samples. The same observation is observed for the $ch\text{-SiO}_x$ inserted samples.

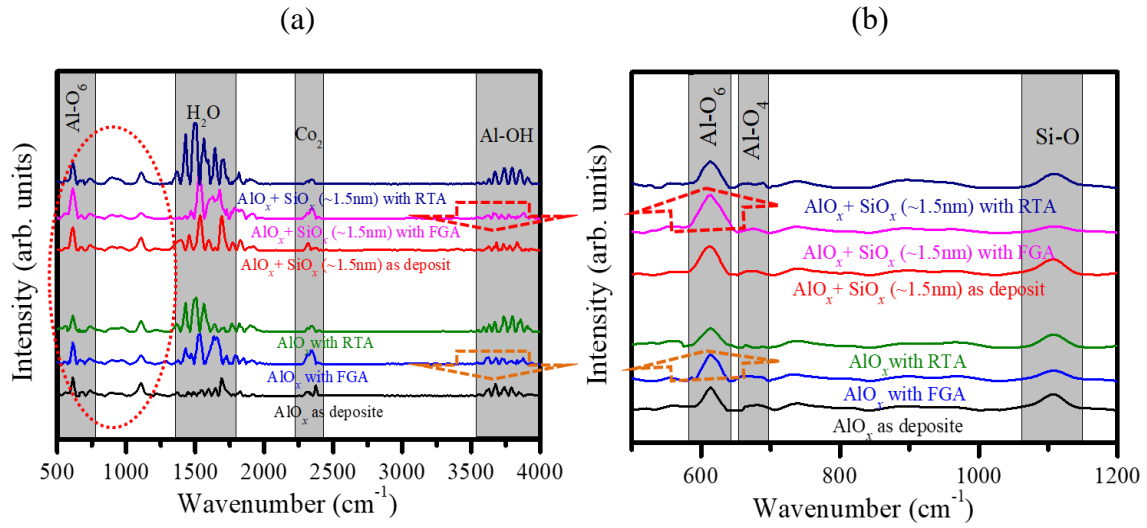


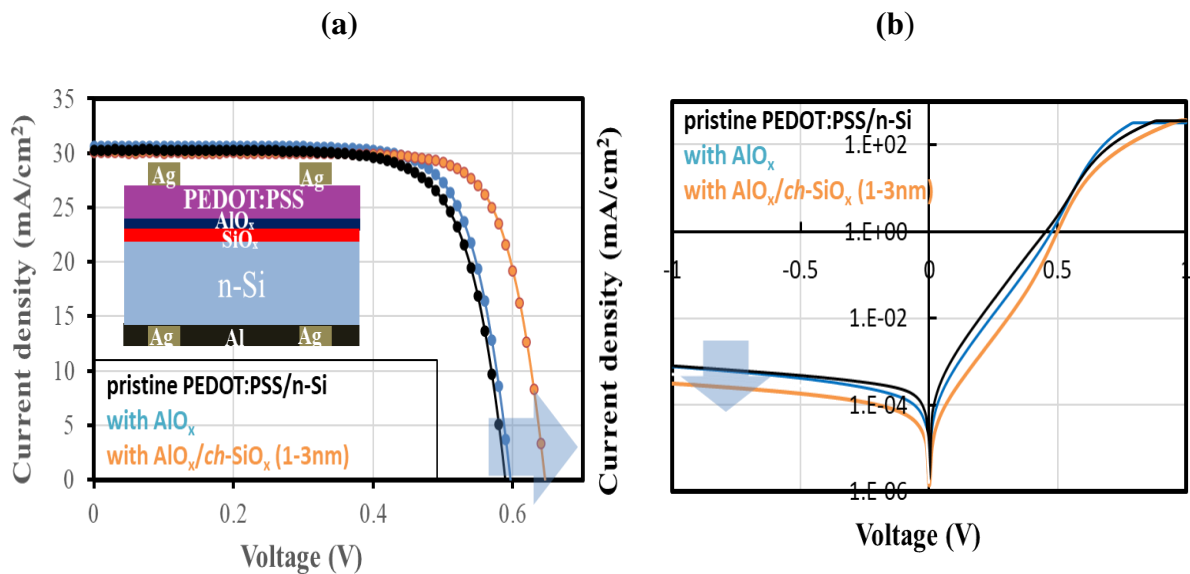
Figure-4.17: FTIR spectra for the $\text{AlO}_x/\text{ch-SiO}_x$ for as-deposited, FGA and RTA from (a) 500-400 and (b) 500-1200 cm^{-1} wavenumber.

From this investigation, it can be concluded that for FGA treated samples, due to the reduction of Al-OH bond at the $\text{AlO}_x/\text{n-Si}$ interface, the enhancement of Al-O_6 bond intensity is evaluated, which enhanced the passivation quality compared with the as-deposited and RTA treated samples. And due to the better passivation quality of the FGA treated ultrathin stack layer of the $\text{AlO}_x/\text{ch-SiO}_x$ interface, we introduced them at the PEDOT:PSS/n-Si junction to improve its passivation quality.

4.3.1 PV performance of FGA treated ALD- $\text{AlO}_x/\text{ch-SiO}_x$ stack layer with the PEDOT:PSS/n-Si heterojunction solar cell

Figure 4.18(a,b) shows the dark and photocurrent density-voltage (J-V) curves of $2 \times 2\text{-cm}^2$ PEDOT:PSS/n-Si($1-5 \Omega \cdot \text{cm}$) heterojunction solar cells with solely AlO_x and $\text{AlO}_x/\text{ch-SiO}_x$ stack ultra-thin layers. The device consisting of an Ag/PEDOT:PSS/n-Si($1-5 \Omega \cdot \text{cm}$)/Ag(Al) structure was used with and without ALD- $\text{AlO}_x/\text{ch-SiO}_x$ stack interlayers.

The solar cell parameters are summarized in Table 4.4. The dark current was suppressed to be lower across the entire bias region from -1 V to 1 V for the device containing FGA-treated $\text{AlO}_x/\text{ch-SiO}_x$ stack interlayer compared with those for the PEDOT:PSS/n-Si devices with and without six cycles $\text{AlO}_x/\text{ch-SiO}_x$ stack layer. V_{oc} increased slightly from 598 to 645 mV without decreasing J_{sc} and FF. No marked increases in the photovoltaic performance were obtained for the device into which solely ALD- AlO_x was inserted. However, the PCE increased from 13.08 % to 14.91 % with an increased V_{oc} of 645 mV and FF of 0.77 by the FGA-treated $\text{AlO}_x/\text{ch-SiO}_x$ stack layer. Figure 4.12(c) shows V_{oc} and V_{bi} for solely AlO_x , the $\text{AlO}_x/\text{ch-SiO}_x$ stack interlayer, and the pristine PEDOT:PSS/n-Si device. For the device that contains the ALD- AlO_x interlayer solely at the PEDOT:PSS/n-Si interface, V_{oc} (V_{bi}) increased from 589 mV (685 mV) to 598 mV (710 mV). However, a further increase in V_{oc} (V_{bi}) up to 645 mV (750 mV) was observed for FGA-treated $\text{AlO}_x/\text{ch-SiO}_x$ (1~3nm) stack layers.



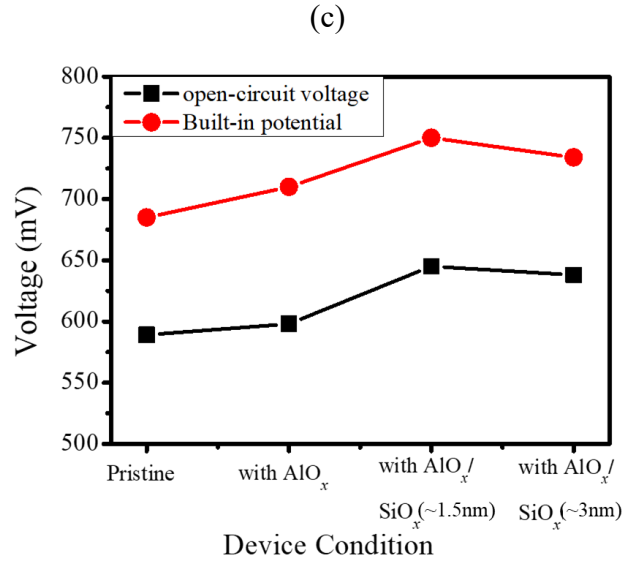


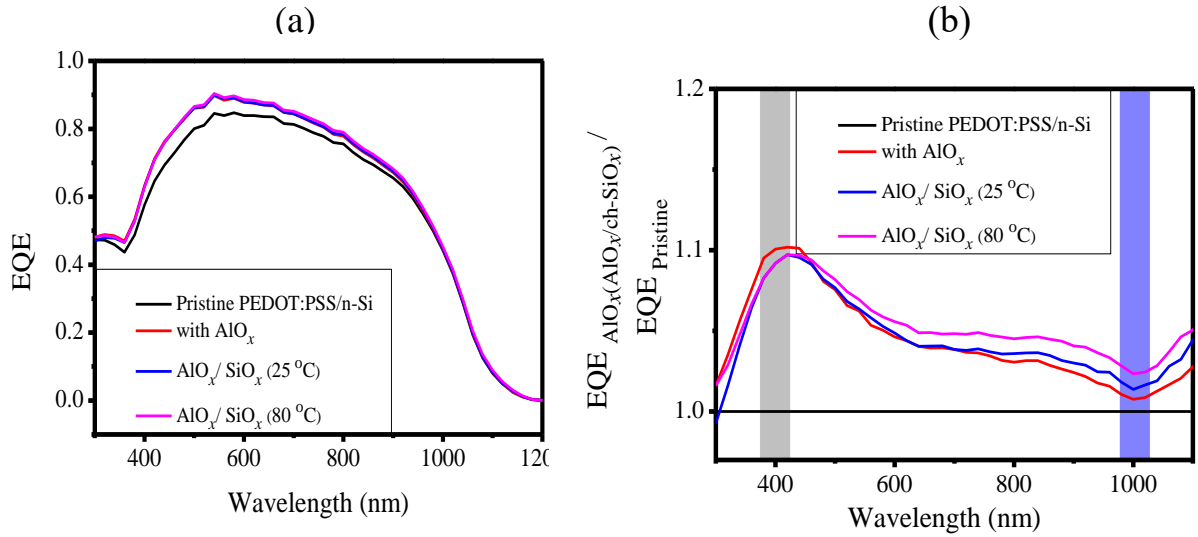
Figure-4.18: (a) Dark and (b) photocurrent density-voltage curves of pristine PEDOT:PSS/n-Si heterojunction solar cell and PEDOT:PSS/n-Si devices together with six cycles ALD- AlO_x solely and ALD- $\text{AlO}_x/\text{ch-SiO}_x$ (1~3nm) stack interlayers. (c) V_{oc} and V_{bi} for the corresponding PEDOT:PSS/n-Si devices.

Table 4.4: Solar cell parameters for the pristine PEDOT:PSS/n-Si device and the devices with solely ALD- AlO_x and the $\text{AlO}_x/\text{ch-SiO}_x$ (1~3nm) stack ultrathin layers.

Device parameters	$J_{sc}(\text{mA}/\text{cm}^2)$	$V_{oc} \text{ (V)}$	FF	PCE (%)
Pristine	30.3	0.589	0.733	13.08
Pristine with AlO_x	31.2	0.598	0.752	14.03
Pristine with $\text{AlO}_x/\text{ch-SiO}_x$ (1~3nm)	30	0.645	0.771	14.91

Figure 4.19(a), (b), and (c), respectively, show the EQE, normalized EQE, and 2D map of EQE at 400 and 1000 nm for the corresponding PEDOT:PSS/n-Si solar cells

with and without ultrathin ALD- $\text{AlO}_x/\text{ch-SiO}_x$ (1~3nm) stack layers. The FGA $\text{AlO}_x/\text{ch-SiO}_x$ stacked interlayer increased the EQE across the entire wavelength region from 400 to 1000 nm compared with that of the device containing solely AlO_x despite the use of the cathode metal contact alone. Notably, the 2D maps of EQE at both the wavelengths, 400 and 1000 nm, (Fig. 4.13(c)) for $2 \times 2 \text{ cm}^2$ PEDOT:PSS/n-Si heterojunction devices with solely AlO_x and the $\text{AlO}_x/\text{ch-SiO}_x$ stack layers are more intense than that of the pristine device. This indicates that the FGA $\text{AlO}_x/\text{ch-SiO}_x$ stack interlayer provides more effective passivation and a stronger built-in-field at the PEDOT:PSS/n-Si anode interface.



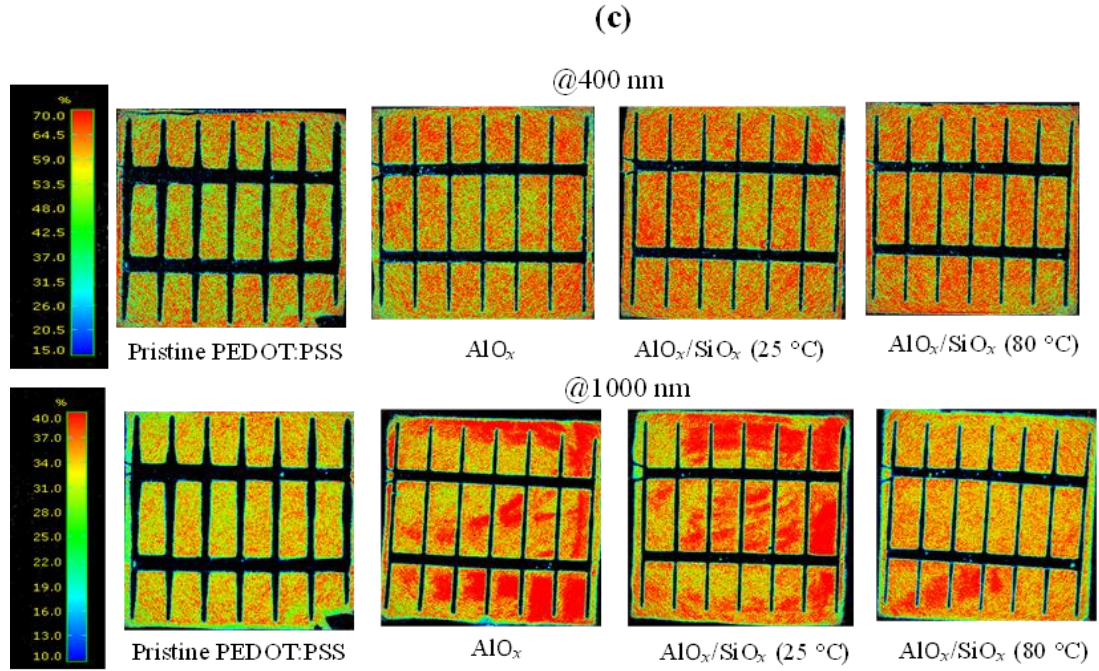


Figure-4.19: (a) EQE, (b) $\text{EQE}_{\text{AlO}_x(\text{AlO}_x/\text{ch-SiO}_x)}/\text{EQE}_{\text{pristine}}$, and (c) 2D mapping of EQE at 400- and 1000-nm wavelengths for pristine PEDOT:PSS/n-Si heterojunction solar cells together with six-cycles ALD- AlO_x solely and ALD- $\text{AlO}_x/\text{ch-SiO}_x$ (1~3nm) stack interlayers.

From the above discussion, it is observed that the higher thickness regimes of AlO_x island act as an anti-reflection layer, not the passivation layer. On the other hand, the ultrathin stack layer of ALD- $\text{AlO}_x/\text{ch-SiO}_x$ (1~3nm) shows us a good passivation layer, which improved the open-circuit voltage and overall performance also. But the interface properties and band alignment of the ALD- $\text{AlO}_x/\text{ch-SiO}_x$ interface is still unclear. Even the effect of the forming gas annealing (FGA) and rapid thermal annealing (RTA) is still unclear. To this aim, in the next chapter, we also investigated the band alignment of the ALD- $\text{AlO}_x/\text{ch-SiO}_x$ interface with and without PEDOT:PSS/n-Si junction.

Bibliography

- [1] Y. Wang, E.A. Irene, “Consistent refractive index parameters for ultrathin SiO₂ films”, J. Vac. Sci. Technol. B **18**, 279 (2000).
- [2] R. Katamreddy, R. Inman, G. Jursich, A. Soulet, and C. Takoudis, “ALD and Characterization of Aluminum Oxide Deposited on Si (100) using Tris(diethylamino) Aluminum and Water Vapor”, J. Electrochem. Soc. **53**, C701 (2006).
- [3] A. Roy Chowdhuri, C. G. Takoudis, R. F. Klie, and N. D. Browning, “Metalorganic chemical vapor deposition of aluminum oxide on Si: Evidence of interface SiO₂ formation”, Appl. Phys. Lett. **80**, 4241 (2002).
- [4] P. Tarte, “Infra-red spectra of inorganic aluminates and characteristic vibrational frequencies of AlO₄ tetrahedra and AlO₆ octahedra”, Spectrochim. Acta A **23**, 2127 (1967).
- [5] A. C. Dillon, A. W. Ott, J. D. Way, and S. M. George, “Surface chemistry of Al₂O₃ deposition using Al(CH₃)₃ and H₂O in a binary reaction sequence”, Surf. Sci. **322**, 230 (1995).
- [6] T. T. A. Li, S. Ruffell, M. Tucci, Y. Mansoulié, C. Samundsett, S. De Iuliis, “Influence of oxygen on the sputtering of aluminum oxide for the surface passivation of crystalline silicon”, Solar Energy Materials and Solar Cells **95**(1), 69–72 (2011).
- [7] P. V. Bulkin, P. L. Swart, and B. M. Lacquet, “Electron cyclotron resonance plasma enhanced chemical vapor deposition and optical properties of SiO_x thin films”, J. Non-Cryst. Solids **226**, 58 (1998).
- [8] L. X. Yi, J. Heitmann, R. Scholz, and M. Zacharias, “Phase separation of thin SiO

- layers in amorphous SiO/SiO₂ superlattices during annealing”, *J. Phys. Condens. Matter* **15**, S2887 (2003).
- [9] Z. Y. Wang, R. J. Zhang, H. L. Lu, X. Chen, Y. Sun, Y. Zhang, T. F. Wei, J. P. Xu, S. Y. Wang, Y. X. Zheng, and L. Y. Chen, “The impact of thickness and thermal annealing on refractive index for aluminum oxide thin films deposited by atomic layer deposition”, *Nanoscale Res. Lett.* **10**, 46 (2015).
- [10] P. Kumar, M. K. Wiedmann, C. H. Winter, and I. Avrutsky, “Optical properties of Al₂O₃ thin films grown by atomic layer deposition”, *Appl. Opt.* **48**, 5407 (2015).
- [11] S. M. Sze, C. R. Crowell, and D. Kahng, "Photoelectric Determination of the Image Force Dielectric Constant for Hot Electrons in Schottky Barriers", *Journal of Applied Physics* **35**, 2534–2536 (1964).

Chapter 5

Band alignment at the PEDOT:PSS/a-AlO_x/ch-SiO_x/c-Si interface

5.1 Determination of band offset and band alignment of ALD-AlO_x/SiO_x stack layer on n-Si substrate

The effect of FGA on the valence-band offset at the AlO_x/n-Si junction with and without *ch*-SiO_x interlayer was determined through Kraut's method reported in 1980 [1]. Figure-4.20 shows the schematic of the heterojunction of semiconductor X and Y with two different bandgap energies.

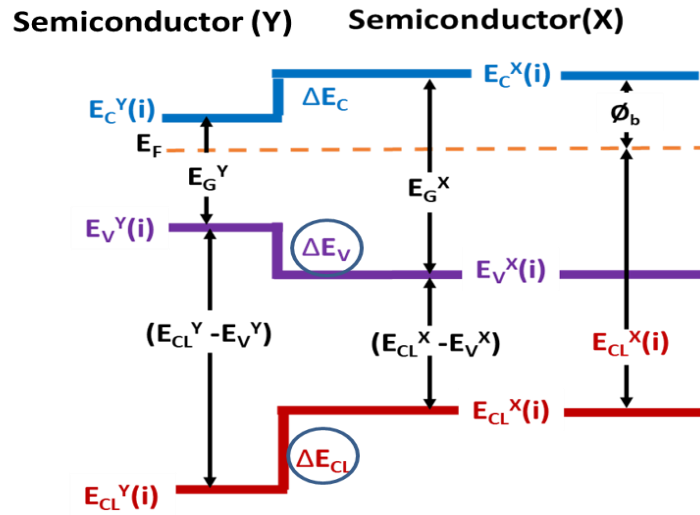


Figure-5.1: Schematic band diagram of an MS junction

As shown in figure 5.1, the valence band offset, ΔE_V is the energy difference between energy levels of the valence band maximum of X and Y. ΔE_C is the conduction band offset between X and Y, and ΔE_{CL} is the core energy difference between X&Y semiconductors. These values can be determined from the following equation

$$\Delta E_V = (E_{CL}^Y - E_V^Y) - (E_{CL}^X - E_V^X) - \Delta E_{CL} \quad (5.1)$$

Where E_V & E_C are the valence band maximum and conduction band minimum at the interface of X&Y semiconductor, to determine the valance band energy difference between X and Y, the information of the core energy level of X and Y, and the threshold energy of the photogenerated electron XY interface is needed. Those values can be obtained from XPS, UPS, or photoemission yield spectroscopy in air.

Figure 5.2(a)–(c) display the XPS Si(2p) and Al(2p) core energy level spectra for the ALD- AlO_x (six cycles)/ n -Si interface with and without tunnel oxide ch - SiO_x (1~3nm) layers. The Al(2p_{3/2}, 2p_{1/2}) core energy was shifted to slightly lower energy by 0.1–0.3 eV for the FGA AlO_x/ch - SiO_x (1~3nm) stack structures compared to that of as-deposited AlO_x on n -Si. The proportion of Si(2p_{1/2}) core energy level was increased compared with the Si(2p_{3/2}), together with the appearance of SiO_x complex related peaks at the higher energy region for ch - SiO_x -inserted AlO_x/n -Si junctions. This finding indicates that the insertion of ch - SiO_x tunnel oxide inserted at the AlO_x/n -Si interface promotes the oxidation through the reduction of AlO_x .

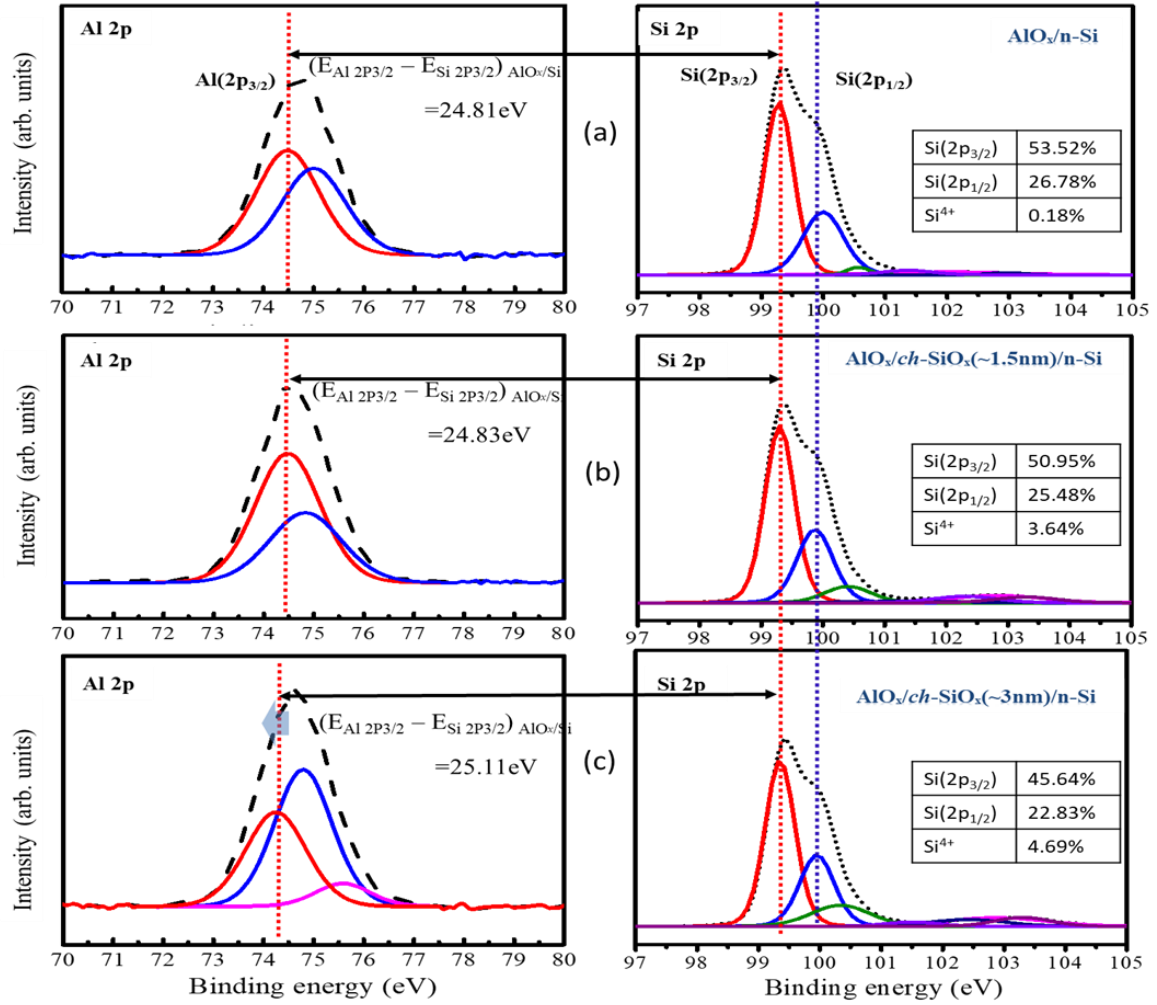


Figure-5.2: XPS spectra of Al(2p) and Si(2p) core energy level regions of (a) ALD-AlO_x/n-Si, (b) AlO_x/ch-SiO_x (~1.5nm)/n-Si, and (c) AlO_x/ch-SiO_x (~3nm)/n-Si samples, respectively. The inset shows the compositional ratio for corresponding samples.

Figure 5.3 (a-c) show the band alignments of ALD-AlO_x/n-Si junctions corresponding to the spectra. These results were obtained by calculating the valence band offset (VBO) values using the following equation derived by Kraut [1]:

$$\Delta E_{\text{VBM}} = (E_{\text{Al } 2P_{3/2}} - E_{\text{Si } 2P_{3/2}})_{\text{Al}_2\text{O}_3/\text{Si}} - [(E_{\text{Al } 2P_{3/2}} - E_{\text{VBM}})_{\text{Al}_2\text{O}_3} - (E_{\text{Si } 2P_{3/2}} - E_{\text{VBM}})_{\text{Si}}] \quad (5.2)$$

Where ΔE_{VBM} is the VBO, i.e., the energy difference between the valence band maxima E_{VBM} of AlO_x and n-Si. E_{Al} and E_{Si} are the binding energies of the $\text{Al}(2\text{P}_{3/2})$ and $\text{Si}(2\text{P}_{3/2})$ core levels, respectively, at the $\text{AlO}_x/\text{n-Si}$ interface [1,2]. The energy differences between these core levels and the corresponding E_{VBM} were determined using experimental results from XPS, PYSA, and KP analyses for the AlO_x layer and bulk n-Si substrates. Thereafter, these values were used to evaluate the ΔE_{VBM} of the corresponding samples with and without tunnel oxide *ch-SiO_x* layers.

The fine scan spectra of the fabricated samples, shown in Fig. 5.2(a)–4(c), show that the energy differences between the $\text{Al}(2\text{p}_{3/2})$ and $\text{Si}(2\text{p}_{3/2})$ core levels, $(E_{\text{Al}2\text{p}_{3/2}} - E_{\text{Si}2\text{p}_{3/2}})_{\text{AlO}_x/\text{n-Si}}$, were approximately 24.81, 24.83, and 25.11 eV for the ALD- $\text{AlO}_x/\text{n-Si}$, $\text{AlO}_x/\text{ch-SiO}_x$ (~1.5nm)/n-Si, and $\text{AlO}_x/\text{ch-SiO}_x$ (~3nm)/n-Si samples, respectively. In addition, the energy differences between the $\text{Al}(2\text{p}_{3/2})$ core level and its VBM, $(E_{\text{Al}2\text{p}_{3/2}} - E_{\text{VBM}})_{\text{AlO}_x}$, were determined to be approximately 69.69, 69.63, and 69.24 eV for the ALD- $\text{AlO}_x/\text{n-Si}$, $\text{AlO}_x/\text{ch-SiO}_x$ (~1.5nm)/n-Si, and $\text{AlO}_x/\text{ch-SiO}_x$ (~3nm)/n-Si samples, respectively, and the energy differences between the $\text{Si}(2\text{p}_{3/2})$ core level and its VBM, $(E_{\text{Si}2\text{p}_{3/2}} - E_{\text{VBM}})_{\text{Si}}$, were determined as 98.6, 98.63, and 98.67 eV for these structures. Substituting these values into Eq. (1), ΔE_{VBM} was calculated as approximately 4.10, 4.17, and 4.32 eV for the ALD- $\text{AlO}_x/\text{n-Si}$, $\text{AlO}_x/\text{ch-SiO}_x$ (~1.5nm)/n-Si, and $\text{AlO}_x/\text{ch-SiO}_x$ (~3nm)/n-Si interfaces, respectively. The conduction band offset (CBO) value, ΔE_{CBM} , for the $\text{AlO}_x/\text{n-Si}$ junction can be determined using the following equation:

$$\Delta E_{\text{CBM}} = (E_g)_{\text{AlO}_x} - (E_g)_{\text{Si}} - \Delta E_{\text{VBM}}, \quad (5.3)$$

Where $(E_g)_{\text{AlO}_x}$ and $(E_g)_{\text{Si}}$ are the band gaps of the ALD- AlO_x layer and n-Si substrate, respectively. The CBO values were obtained from Eqs. (1) and (2) were 1.78, 1.71, and

1.56eV for the corresponding samples. These findings indicate that the chemical tunnel oxide ch -SiO_x modifies the VBO and CBO with an increase in VBO at higher concentrations of the Si^{*} related complex. The results are summarized in detail in Table 5.1.

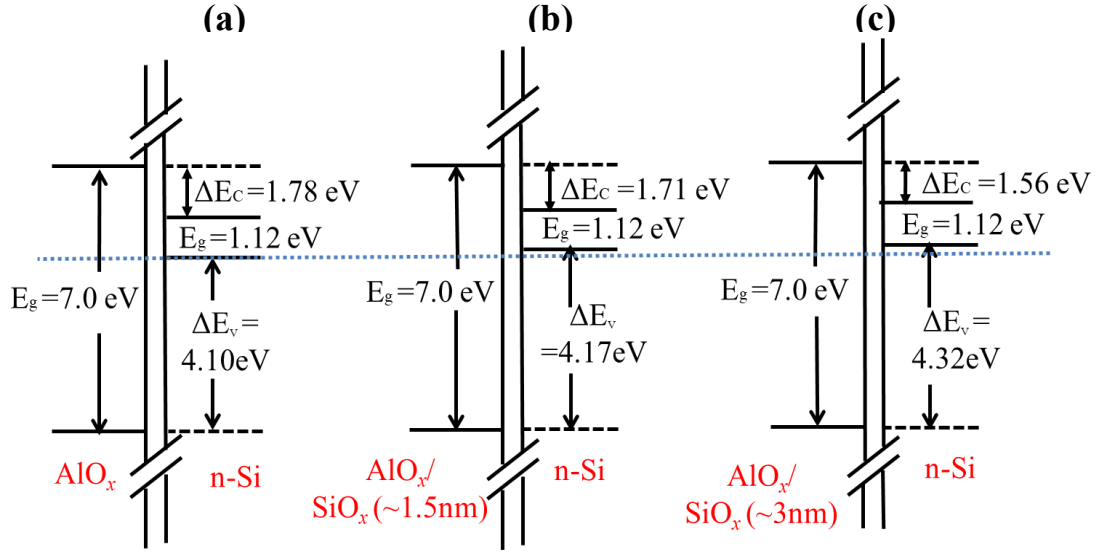


Figure-5.3: Derived band alignment and band offset of the ALD-AlO_x/n-Si interface with and without tunnel oxide ch -SiO_x (1~3nm) layers.

Table 5.1: Determination of valance band offset for ALD-AlO_x/n-Si interface with and without tunnel oxide ch -SiO_x layers

Interface layer	($E_{Al2P3/2}$) AlO _x (eV)	(E_{VBM}) AlO _x (eV)	($E_{Si2P3/2}$) Si (eV)	(E_{VBM}) Si (eV)	($E_{Al2P3/2}$) AlO _x - (E_{VBM}) AlO _x (eV)	($E_{Si2P3/2}$) Si - (E_{VBM}) Si (eV)	($E_{Al2P3/2}$ - $E_{Si2P3/2}$) AlO _x /Si (eV)	ΔE_{VBM} (eV)	ΔE_{CBM} (eV)
AlO _x /n-Si	74.47	4.78	99.4	0.68	69.69	98.72	24.93	4.10	1.78
AlO _x /SiO _x (25°C)/n-Si	74.48	4.85	99.43	0.68	69.63	98.75	24.95	4.17	1.71
AlO _x /SiO _x (80°C)/n-Si	74.24	5.00	99.40	0.68	69.24	98.72	25.16	4.32	1.56

5.3.4 Effect of FGA treated ALD- $\text{AlO}_x/\text{ch-SiO}_x$ stack layer at the PEDOT:PSS/n-Si interface

Table-5.2 shows the sheet resistance of the PEDOT:PSS/n-Si device with and without $\text{AlO}_x/\text{ch-SiO}_x$ stack layers. Initially, the sheet resistance for the PEDOT:PSS/n-Si interface was about 162 ohm.sqr. But once the stack layer of $\text{AlO}_x/\text{ch-SiO}_x$ was used, the sheet resistance becomes lower compared with previous. Moreover, the FGA-treated $\text{AlO}_x/\text{ch-SiO}_x/\text{PEDOT:PSS}$ shows the lower sheet resistance compared with others. These results indicate that FGA treated samples show the lower sheet resistance compared with others treated samples that refer to better passivation quality.

Table-5.2: Sheet resistance for PEDOT:PSS/n-Si devices with and w/o AlO_x and $\text{AlO}_x/\text{ch-SiO}_x(1\sim 3\text{nm})$ interlayers

Device parameters	Sheet resistance, (Ω/\square)	
PEDOT:PSS/n-Si	162	
	Without FGA	With FGA
PEDOT:PSS/ AlO_x /n-Si	145	117
PEDOT:PSS/ $\text{AlO}_x/\text{ch-SiO}_x(\sim 1.5\text{nm})$ /n-Si	132	110
PEDOT:PSS/ $\text{AlO}_x/\text{ch-SiO}_x(\sim 3\text{nm})$ /n-Si	123	105

Figure-5.4 presents the derived energy band diagrams of (a) PEDOT:PSS/n-Si, (b) PEDOT:PSS/ AlO_x /n-Si, and (c) PEDOT:PSS/ $[\text{AlO}_x/\text{ch-SiO}_x(1\sim 3\text{nm})]$ /n-Si junctions determined from a combination of XPS, C-V, and KP measurements. The illustration at the top is a schematic representation of the energy band diagram of the PEDOT:PSS/n-Si junction with the definitions of each energy level. E_c , E_v , and E_f are the conduction band

minimum, valence band maximum, and Fermi level, respectively. E_i is the intrinsic energy level of c-Si. $\Psi_{bi}(p)$ and $\Psi_{bi}(p, inv)$ are the built-in fields at the PEDOT:PSS/n-Si heterojunction with and without ALD- $AlO_x/ch-SiO_x$ (1~3nm) stack interlayers, respectively. The procedure to determine each value is described in detail elsewhere [3-4]. The Fermi energy and CBO, $|E_c-E_f|$, increased because of the insertion of ALD- AlO_x at the PEDOT:PSS/n-Si interface with higher VBM of (4.10 eV) compared with that of the PEDOT:PSS/n-Si interface alone. As a result, V_{bi} also increased from 680 mV to 710 mV because of the increased $|E_i-E_f|$. Furthermore, V_{bi} increased to 750 mV because of the higher VBM (4.32 eV) for the ALD- $AlO_x/ch-SiO_x$ stack interlayer. These results suggest that a strong inversion layer is formed at the PEDOT:PSS/n-Si interface with the ALD- $AlO_x/ch-SiO_x$ stack interlayer.

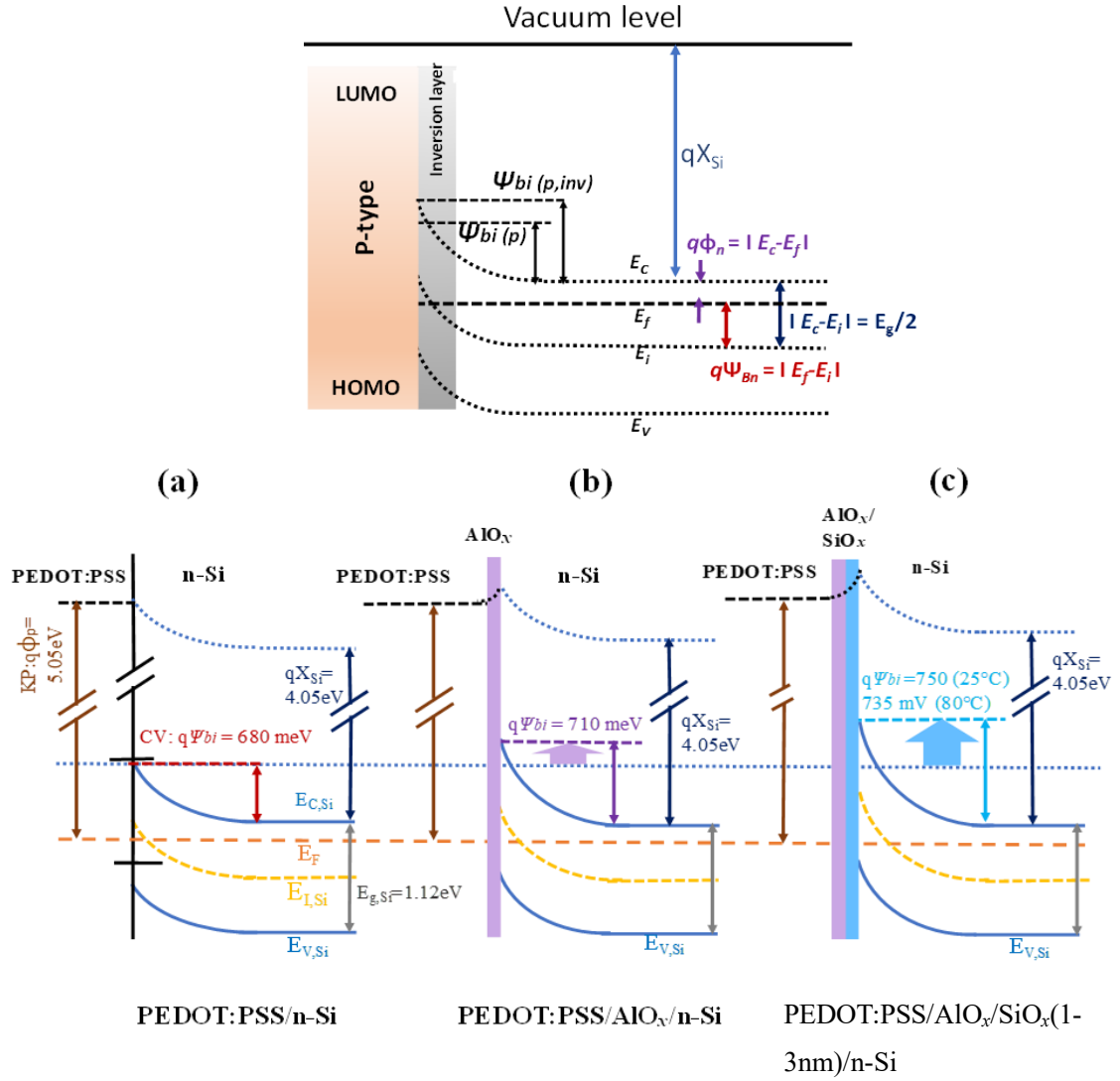


Figure-5.4: (top) Schematic energy band diagram of PEDOT:PSS/n-Si junction, including definitions of the energy differences. (bottom) Derived energy band diagrams of (a) PEDOT:PSS/n-Si, (b) PEDOT:PSS/AlO_x/n-Si, and (c) PEDOT:PSS/AlO_x/ch-SiO_x (1~3nm)/n-Si.

Based on the results described above, the effect of the FGA AlO_x/ch-SiO_x stack interlayer at the PEDOT:PSS/n-Si interface is considered as follows. The μ -PCD, XPS, and SE revealed that the FGA promotes the formation of Si^{*} suboxide and Si⁴⁺ within

several monolayers near the top surface, which enhances the passivation ability of n-Si. XPS also revealed that the Al(2p) core energy level was decreased, and the VBO at the *ch*-SiO_x/n-Si junction increased as the thickness of the tunnel oxide *ch*-SiO_x layer increased at higher immersion temperature at ~3nm thick AlO than that at ~1.5nm. These findings suggest that the reduction of the AlO_x layer results in the promotion of oxidation of the tunnel oxide SiO_x layer [6-8]. In addition, sheet resistance decreased from 162 Ω/□ for solely PEDOT:PSS to 117 Ω/□ for the solely AlO_x and further reduced to 105–110 Ω/□ for the AlO_x/*ch*-SiO_x (1~3nm) stack layer after FGA. These results suggest that the negative charge stored in the ALD-AlO_x layer increased because of the removal of oxygen after FGA by reduction. This indicates that both the increased passivation ability and increased negative charge storage in the ALD-AlO_x layer contribute to the increase in V_{bi} at the PEDOT:PSS/n-Si anode interface and increase in V_{oc} in PEDOT:PSS/n-Si heterojunction solar cells.

Bibliography

- [1] E. A. Kraut, R. W. Grant, J. R. Waldrop, and S. P. Kowalezyk, Phys. Rev. Lett. “Precise Determination of the Valence-Band Edge in X-Ray Photoemission Spectra: Application to Measurement of Semiconductor Interface Potentials **44**, 1620 (1980).
- [2] Z. P. Ling, Z. Xin, G. Kaur, C. Ke, and R. Stangl, “Ultra-thin ALD- AlO_x /PEDOT:PSS hole selective passivated contacts: An attractive low cost approach to increase solar cell performance” Sol. Energy Mater. Sol. Cells, **185**, 477 (2018).
- [3] T. Sakata, N. Ikeda, T. Koganeazawa, D. Kajiya, and L Saitow, “Performance of Si/PEDOT:PSS Solar Cell Controlled by Dipole Moment of Additives” J. Phys. Chem. C **33**, 20130 (2019).
- [4] K. Kasahara, J. Hossain, D. Harada, K. Ichikawa, R. Ishikawa, and H. Shirai, “Crystalline-Si heterojunction with organic thin-layer (HOT) solar cell module using poly(3,4-ethylenedioxythiophene):poly(styrene sulfonate)(PEDOT:PSS)” Sol. Energy Mater. Sol. Cells **181**, 60 (2017).
- [5] D. Zielke, A. Pazidis, F. Werener, J. Schmidt, “Organic-silicon heterojunction solar cells on n-type silicon wafers: The BackPEDOT concept.” Sol. Energy Mater. Sol. Cells **131**: p. 110 (2014).
- [6] M. Schmidt, L. Korte, A. Laades, R. Stangl, Ch. Schubert, H. Angermann, E. Conrad, and K. v. Maydell, “Physical aspects of a-Si:H/c-Si hetero-junction solar cells” Thin Solid Films **515**, 7475 (2007).
- [7] H. Wang, M. R. Page, E. Iwaniczko, D. H. Levi, Y. Yan, H. M. Branz, and Q. Wang, Proc. of the 14th Workshop on Crystalline Silicon Solar Cells and Modules,

NREL/BK-**520**-36622, 74, (2004).

- [8] V. A. Dao, Y. Lee, S. Kim, J Cho, S. Ahn, Y. Kim, N. Lakshminarayam and J. Yi, “Effect of Valence Band Offset and Surface Passivation Quality in the Silicon Heterojunction Solar Cells” J. Electro chem. Soc. V. **158**(11), H1129-H1132 (2011).

Chapter 6

Summary and future work

5.1 Summary and conclusion

In this work, we have studied the junction property of the solution-processed PEDOT:PSS/n-Si junction using the selective carrier contacts such as TiO_2 and AlO_x at the cathode and anode interface. The key observations of this work are given below:

a) Effect of TiO_2 as a Hole Blocking Layer in the PEDOT:PSS/n-Si Heterojunction Solar Cells

Usually, the hole blocking layer has been used to improve the passivation ability at the n-Si/cathode interface. But here, the low-temperature solution process TiO_2 is used as an HBL layer to enhance the passivation of the n-Si/cathode interface. Transient reverse recovery analysis depicted that using TiO_2 at the n-Si/cathode interface, the recombination velocity, S has been decreased compared with the metal contact. In the case of direct metal contact (cathode) to n-Si, S is found around 750cm/s, which is reduced to 15.5% by single-layered TiO_2 as a hole blocking layer. For further reduction of S , a double layer TiO_2 is used to avoid the direct metal contact to Si. These results suggested that the recombination at the cathode interface can be reduced by using a double layer of TiO_2 for avoiding direct metal contact to the c-Si.

Additionally, using the TiO_2 as an HBL at the cathode/n-Si interface, the PCE of PEDOT:PSS/n-Si solar cell is increased from 11.2% to 13.08%. Also, the carrier collection efficiency is increased at the cathode/n-Si interface for the TiO_2 inserted device, which is confirmed from the EQE.

b) Effect of ALD- AlO_x island at the PEDOT:PSS/n-Si interface by the UV photolithography process

Using the higher passivation layer, the junction property of PEDOT:PSS/n-Si interface can be improved due to the reduction of sheet resistance produced at the PEDOT:PSS/plane n-Si interface. For this aim, a high k-material of the AlO_x layer has been introduced between the PEDOT:PSS/n-Si junction. But, AlO_x itself as a high insulation layer, so for the flow of photo-generated carrier to the anode interface, AlO_x island has been demonstrated for tunneling through the 20nm thick AlO_x layer by UV photolithography process. A higher built-in field has been achieved at the PEDOT:PSS/n-Si junction for the AlO_x island, which was determined from the C-V analysis. Also, the current density is enhanced for the AlO_x island inserted device, which is confirmed from the JV, EQE study. Thus, we found that AlO_x island acts as an anti-reflection coating layer.

c) Effect of thermally annealed atomic-layer-deposited AlO_x / chemical tunnel oxide stack layer at the PEDOT:PSS/n-type Si interface to improve its junction quality

As we studied that the high thickness of AlO_x acts as an ARC layer, we turn our investigation to the ultrathin AlO_x /*ch*- SiO_x stack layer to improve the junction quality of PEDOT:PSS/n-Si interface as a passivation layer. As the passivation quality of the ultrathin AlO_x layer is not so attractive, for the purpose of its improvement, ultrathin *ch*- SiO_x has been inserted between the AlO_x /n-Si interface as well as annealed the device using FGA at ambient condition. XPS study revealed that FGA promotes the reduction of the AlO_x layer as well as the oxidation of Si suboxide related complex, which mainly enhances the passivation quality at the surface. From the CV and JV studies, it is found that the built-in field and open-circuit voltage is increased compared with the pristine device. The EQE for the corresponding PEDOT:PSS/n-Si heterojunction solar cells with

the ALD- $\text{AlO}_x/\text{ch-SiO}_x$ stack layer was enhanced across the entire wavelength range of 350 to 1100 nm, which was provided by a stronger inversion layer at the PEDOT:PSS/n-Si anode interface and increased the minority carrier collection efficiency.

5.2 Future Work

The PV performance of the solar cell depends on several more interface properties. For further improvement of the cell performance and to understand the interface properties, some more approaches are as follows:

1. The light stability test for the ALD- $\text{AlO}_x/\text{ch-SiO}_x$ stack layer can be investigated under light exposure at different illumination times.
2. Also, the stability for the corresponding device with and without the emitter layer of PEDOT:PSS can be another work.
3. For the more clearer effect of $\text{AlO}_x/\text{ch-SiO}_x$ layer at the PEDOT:PSS/n-Si heterojunction solar cell, contact resistivity or sheet resistance measurement is needed.
4. FGA can be reduced the recombination loss at the n-Si/cathode interface.
5. The transient reverse recovery study can be extended to understand the effect of ALD- $\text{AlO}_x/\text{ch-SiO}_x$ stack layer at the PEDOT:PSS/n-Si junction.